technische universität dortmund

MERCUR Mercator Research Center Ruhr

From High Energy Physics to Hospital

—

Investigation of the ATLAS IBL Pixel Detector for Applications in Proton Therapy

Dissertation

submitted in partial fulfillment of the requirements
for the degree of

doctor rerum naturalium
(Dr. rer. nat.)

of the Department of Physics
TU Dortmund University, Germany

by

Isabelle Schilling
born in Giessen

- 2023 -

A dissertation submitted to the department of physics of TU Dortmund University in partial fulfillment of the requirements for the degree of doctor of science.

First corrector:	Prof. Dr. Kevin Kröninger
Second corrector:	PD Dr. Christian Bäumer
Head of commission:	Prof. Dr. Christoph Lange
Representative of scientific staff:	PD Dr. Jörg Bünemann

Date of submission:	12.04.2023
Date of disputation:	07.06.2023

Abstract

The effort to obtain continual progress in treatment quality in proton therapy facilities implies new technical requirements, mainly for the irradiation machines and the detector systems. For example, the collimation of proton spots generates stepper dose gradients and, thereby, the need for detectors with a high spatial resolution. Besides this, beam currents around 2 nA ($\approx 1.2 \cdot 10^{10}\ \frac{\text{protons}}{\text{s}}$) during patient treatment set challenging requirements on the detectors' readout electronics for single particle tracking or counting.
The knowledge gained in detector development in High Energy Physics (HEP) during the past decades is transferred to proton therapy applications in this work to address the upcoming detector requirements. It provides studies investigating the usage of a pixel detector designed for individual particle tracking in the high-radiation environment of the ATLAS experiment at LHC, namely the ATLAS IBL Pixel Detector, for proton beam measurements at proton therapy facilities. Due to the small pixel size of the detector under study, the shape of single pencil beam proton spots is determined with precision in the smaller pixel direction of 28 µm. The timing information of the particle hits on the detector allows the distinction between the single spots of scanned proton fields. Dose linearity checks reveal that the detector meets the requirement of an output dose consistency of $\pm 3\,\%$ for the daily quality assurance (QA) in the chosen dose range. Additionally, further studies lead to the conservative assumption that hit rates up to $(73.85 \pm 0.95)\ \frac{\text{clusters}}{25\,\text{ns}}$ sampled with a frequency of 1 kHz feature a linear dependency on the beam current. Furthermore, the provided information on the deposited energy in the detector is utilized for range verification. Range differences of 1 mm required for the daily QA can be detected for proton energies impinging the sensor in the range of $(30 - 44)$ MeV. Finally, an example of using the detector under study in the field of proton therapy is given by supporting a study investigating the energy deposition of platinum nanoparticles on a macroscopic scale. This work offers a characterization of the ATLAS IBL Pixel detector for proton therapy application and points out improvement opportunities for further detector development.

Kurzfassung

Der Anspruch der kontinuierlichen Verbesserung der Behandlungsqualität in Protonentherapie Einrichtungen sorgt gleichzeitig für neue technische Anforderungen, vor allem an Detektorsysteme. Ein Beispiel dafür ist die Kollimation einzelner Protonennadelstrahlen. Um die erzeugten, steilen Dosisgradienten zu vermessen, werden Detektoren mit hoher räumlicher Auflösung benötigt. Des Weiteren sorgen die in der Protonentherapie üblichen Strahlströme um 2 nA für hohe Anforderungen an die Ausleseelektronik der Detektoren, wenn das Ziel der Messung die Einzelteilchenverfolgung ist. Um den wachsenden Detektoranforderungen gerecht zu werden, wird in dieser Arbeit das Wissen aus jahrzehntelanger Entwicklung für die Hochenergiephysik (HEP) auf Anwendungen in der Protonentherapie übertragen. Dafür wird der ATLAS IBL Pixeldetektors, der für die Einzelteilchenverfolgung in der Hochstrahlungsumgebung des ATLAS Experiments am LHC entwickelt wurde, für Protonenstrahlmessungen an Therapieanlagen charakterisiert. Aufgrund der Pixelierung des Detektors kann die Form einzelner Nadelstrahlen mit einer Genauigkeit in der kleineren Pixelrichtung von 28 µm bestimmt werden. Die zeitliche Information der Treffer auf dem Detektor ermöglicht die Betrachtung einzelner Nadelstrahlen gescannter Protonenfelder. Überprüfungen der Dosislinearität zeigen, dass der Detektor die Anforderung einer Ausgangsdosis-Konsistenz von $\pm 3\,\%$ für die tägliche Qualitätssicherung (QS) in dem gewählten Dosisbereich erfüllt. Zusätzliche Studien führen außerdem zu der konservativen Annahme, dass Trefferquoten bis zu $(73,85 \pm 0,95)\,\frac{\text{clusters}}{25\,\text{ns}}$, abgetastet mit einer Frequenz von 1 kHz, eine lineare Abhängigkeit zum Strahlstrom aufweisen. Die Information über die im Detektor deponierte Energie wird in dieser Arbeit zur Reichweitenverifizierung genutzt. Nach der Kalibrierung der mittleren deponierten Energien auf Referenzwerte aus der NIST PSTAR Datenbank können für Protonen, die mit einer Energie im Bereich von $(30 - 44)$ MeV auf den Sensor treffen, die für die tägliche QS erforderlichen Reichweitendifferenzen von 1 mm unterschieden werden. Abschließend wird der Detektor zur Untersuchung der Energiedeposition von Platin-Nanopartikeln auf makroskopischer Ebene eingesetzt, um ein Beispiel für eine mögliche Anwendung zu geben. Zusammenfassend liefert diese Arbeit eine Charakterisierung des ATLAS IBL Pixel Detektors für die Anwendung in der Protonentherapie und zeigt Ansätze für die weitere Detektorentwicklung auf.

Chapter

Contents

Contents **vi**

1 Introduction **1**

2 Proton therapy **5**

2.1 Interaction of protons with matter 5
2.2 Proton beam therapy system 9
2.3 Beam delivery technique 10
2.4 Quality Assurance 12
2.5 Commonly used detectors 12

3 Silicon particle detectors **15**

3.1 Detectors in High Energy Physics 15
3.2 Conduction in silicon 16
3.3 Doping and p-n junction 18
3.4 Particle detection with silicon sensors 19

4 ATLAS IBL Pixel Detector **23**

4.1 Hybrid Pixel Modules 23
4.2 Sensor technology - planar n-in-p 24
4.3 Readout chip FE-I4B 26
4.4 Readout system 29
4.5 Tuning of the readout chip 30
4.6 ToT Calibration 33
4.7 Experimental Setup 35
4.8 Processing and clustering of data 36

5 PBS spot shape and position measurements **37**
5.1 Measurement settings 38
5.2 Spot shape characterization 39
5.3 Spot position characterization 44

6 Dose consistency measurements **47**
6.1 Dose linearity in PBS mode 47
6.2 Dose linearity measured for varying beam currents 51
6.2.1 Experimental Setup 51
6.2.2 Impact of sensitive time per trigger 52
6.2.3 Investigation of memory consumption 54
6.2.4 Dose linearity 56

7 Energy deposition measurements **59**
7.1 Measurement settings 60
7.2 Beam characteristics 61
7.3 LET approximation thin detectors 63
7.4 Characterization deposited energy spectra 65
7.5 Impact of tuning setting 70
7.6 LET spectra measurements 72
7.7 Track LET measurements 79

8 Energy deposition in platinum nanoparticles at macroscopic scale **85**
8.1 Introduction to study structure 86
8.2 Energy deposition comparison 87
8.3 Spot profile comparison 91

9 Conclusion and Outlook **95**

Bibliography **99**

Publications **115**

Acknowledgments **119**

Chapter

List of Acronyms

ATLAS	A Toroidal LHC Apparatus	16, 23, 24, 59
BCU	bunch crossing unit	xiii, 27, 36, 53, 55–58, 66
CERN	European Organization for Nuclear Research	15, 23
CMOS	complementary-metal-oxide-semiconductor	26
CSDA range	continuous slowing down approximation range	xii, 8, 80–84
HEP	High Energy Physics	2, 15, 16, 25, 29, 47, 61
IBL	Insertable B-Layer	2, 16, 23
LET	Linear-Energy-Transfer	xii, 2, 59, 63, 81
LHC	Large Hadron Collider	15, 16
MBRT	Minibeam radiation therapy	37, 97

MCS	multiple Coulomb scattering	5, 9
MU	monitor units	48–50, 56
NPs	noble metal nanoparticles	85, 86
PBS	pencil beam scanning	vi, xi, 10–13, 37, 38, 41, 44, 47–50, 52, 55, 60, 91
PCB	printed circuit board	xi, 24
PtNPs	platinum NPs	86, 87, 91, 97
QA	quality assurance	1, 3, 12, 13, 38, 44, 47, 48, 50, 59, 77, 78, 84, 96
ROI	region of interest	73, 74, 88
SEM	standard error of the mean	xiii, 33, 52, 53, 56
SM	Standard Model	15
SOBP	spread-out Bragg peak	8, 10

ToT	Time over Threshold	xiii, 26, 27, 29, 31, 36, 39, 54, 65, 67, 69–72, 75, 88
UPTD	University Proton Therapy Dresden	9, 51, 66, 97
WER	water-equivalent ratio	72, 91
WET	water-equivalent thickness	9, 51, 63, 64
WPE	West German Proton Therapy Centre Essen	9, 11, 38, 39, 43, 44, 48, 51, 60, 61, 64, 80, 86, 87, 92

Chapter

List of Figures

2.1 Mass stopping power of protons traversing silicon or liquid water. . . 7
2.2 Depth dose profile of a monoenergetic proton beam. 8
2.3 Schematic sketch of pencil beam scanning (PBS) delivery technique. . 11

3.1 Bond situation n-type and p-type silicon. 18
3.2 Depletion zone width of a p-n junction. 19

4.1 PCB loaded with bare module. 24
4.2 Schematic cross section n^+-in-p sensor. 25
4.3 Schematic diagram analog pixel. 26
4.4 Conversion from analog signal to digital ToT signal. 27
4.5 USBpix setup. 30
4.6 STcontrol scan results for exemplary tuning. 31
4.7 Mean injected charge as a function of the ToT values. 34
4.8 Setup to operate the detector. 35

5.1 Picture setup beam spot characterization. 39
5.2 Hitmap showing pencil beam spots. 41
5.3 Hitmaps showing pencil beam spots of various energies. 42
5.4 Pencil beam spot σ as a function of proton energy. 43
5.5 Asymmetry of pencil beam spot as a function of proton energy. . . . 44
5.6 Mean pencil beam spot σ as a function of proton energy. 44
5.7 Position determination of individual pencil beam spots. 45

6.1 Temporal distribution of clusters over irradiation duration. 49
6.2 Averaged total number of clusters as a function of dose. 50

6.3 Temporal distribution of clusters taken with a different TrigCnt parameter. 53
6.4 Correlation between stored Trigger ID and temporal distribution of clusters. 55
6.5 $\bar{R}_{\mathrm{TrigCnt}}$ corresponding to the dose for various beam currents. 56

7.1 Proton energy stages during measurement. 62
7.2 Calculation of $dE_{\mathrm{expected,Si}}$ 62
7.3 Sketch introducing incident angle of protons. 64
7.4 Energy dependent cluster size distribution. 65
7.5 Deposited energy spectra measured with sensors of different thicknesses. 68
7.6 Simulated deposited energy spectra of 55 MeV protons in a 200 µm silicon sensor. 71
7.7 Picture setup beam energy measurements. 73
7.8 Exemplary energy deposition map downstream of PMMA absorber. . 74
7.9 Correlation measured mean deposited energy in silicon and expectation. 75
7.10 Calibration of measured mean deposited energy to NIST PSTAR database. 76
7.11 Histogrammed pull for energy deposition calibration procedure. . . . 77
7.12 Range determination uncertainties corresponding to the proton energy. 78
7.13 Sketch parallel alignment of detector. 79
7.14 Experimental setup track LET measurement. 79
7.15 Track length distributions for parallel proton incident. 80
7.16 Energy deposition along proton tracks in sensor. 82
7.17 Measured CSDA ranges compared with NIST reference. 83

8.1 Setup PtNP characterization. 88
8.2 Deposited energy distributions for PtNP and nonPtNP cubes. 89
8.3 Spatial information of the clusters corresponding to trigger count. . . 92
8.4 Spot widths and positions for individual PBS spots. 93

Chapter

List of Tables

4.1 Correlation between the 4-bit stored ToT values (hex) and the true ToT for the HitDiscCnfg register settings 0, 1, and 2. [1] 28

6.1 The investigated TrigCnt settings and the corresponding average number of clusters per BCU. The uncertainty on the results is given by the SEM. 53

6.2 Settings of I_{beam} and corresponding dose values measured with the integrated ionization chamber at the nozzle's exit for a fixed irradiation time of 1 s. The TrigCnt parameters and measured clusters per BCU $\bar{R}_{\text{TrigCnt}}$ are listed. 57

7.1 Tuning settings of the detector used for the energy deposition measurements. The thickness of the sensor. the charge threshold and the ToT at target charge are listed. 67

8.1 Measured mean deposited energies $dE_{\text{SI,200}}$ and mean deposited energy ratios $dE_{\text{SI,ratio}}$ for the different setups downstream the PtNP and nonPtNP samples. The 1σ interval takes into account the height ratio of the different samples. updated [2] 89

8.2 Measured mean spot width σ_{spot} and mean spot width ratios $\sigma_{\text{spot,ratio}}$ for PtNP and nonPtNP samples of different thickness and for different proton energies. 94

Chapter 1
Introduction

Since its development in the 1950s, proton and ion beam therapy was steadily improved, so the number of treated patients has risen up to this decade [3, 4]. Compared to conventional radiotherapy with high-energy photons or gamma rays, the depth dose distribution of protons with the maximum energy deposition towards the end of their range is the decisive advantage of proton therapy. Many patients benefit from the improved sparing of healthy tissue [5]. The effort to obtain continuous progress in treatment quality in proton therapy facilities at the same time also causes new technical requirements for the equipment needed for therapy.
Apart from the beam delivery systems, this mainly concerns detector systems. Those indispensable devices are used to characterize and monitor the proton fields, which directly impact the patients' safety in terms of improved procedures in quality assurance (QA). In addition, detector systems are utilized for various experiments concerning proton therapy: from investigating the radiobiological effectiveness of protons to developing proton radiography systems for patient positioning. Further literature gives an overview of existing detectors for medical applications [6].

The requirements for the detector systems have to be considered individually for each application, as will be discussed afterward.
Several approaches in the proton therapy community strive to improve the shaping of the high-dose regions of the proton fields to the surface of the tumor volume. Small proton fields with sharp dose gradients are single examples to be managed [7, 8]. Consequently, one has to notice that the detector system must have a higher spatial resolution to characterize those fields compared to the measurement of commonly used proton fields [9, 10].
Besides this, a detector used in proton therapy applications has to deal with the

high beam currents around 2 nA ($\approx 1.2 \cdot 10^{10}\ \frac{\text{protons}}{\text{s}}$) during patient treatment [11]. Suppose the aim of the detector application is single proton counting as in a real-time beam monitor, for example. In that case, the readout electronics have to be adapted to the expected beam currents [12, 13]. Moreover, imaging techniques like proton radiography mostly require the tracking of individual particles to precisely determine the hit position on the detector plane and the Linear-Energy-Transfer (LET) [14]. An ideal detector for this purpose would be able to measure the individual energy deposition per proton in a thin layer to allow conclusions on the stopping power of the tissue. However, most detector system tested for this, like the TimePix detector [15], suffer from high beam currents [16].
In addition, detectors used in proton therapy have to be resistant to radiation damage for a long lifetime in clinical usage.
Most of the addressed requirements on detector systems in medical physics application can be compared to those established for detectors in HEP experiments. For example, the ATLAS Insertable B-Layer (IBL) Pixel Detector can be chosen that is commonly used in the ATLAS experiment at the particle accelerator facility CERN. The experiment is operated to advance the fundamental research on particle decays and the associated physics phenomena. The ATLAS IBL Pixel Detector comprises a silicon sensor and an FE-I4B readout chip bump bonded to it [17, 18]. The detector system is located as the innermost component of the ATLAS detector around the interaction point of the particle collision. Therefore, it is designed to be radiation tolerant with an expected ionizing dose over the lifetime of the ATLAS experiment of 2.5 MGy. Being developed to track charged particles, the ATLAS IBL Pixel Detector has a high spatial resolution with pixel sizes of 50 µm × 250 µm.
At this point, this thesis wants to answer whether the ATLAS Pixel Detector can be used in proton therapy applications to deal with the technological progress and the rising requirements on detector systems. Therefore, the aim is to transfer the knowledge on research and development of pixelated semiconductor detectors for HEP to medical physics. Based on the imposed detector requirements, the ATLAS IBL Pixel Detector's features will be investigated, and possible improvements in the scope of proton therapy will be identified.
In order to achieve this goal, this work presents experimental studies performed at two proton therapy facilities (West German Proton Therapy Centre Essen and University Proton Therapy Dresden) dealing with the main features of the detector:

high spatial resolution due to small pixel size, sampling of the beam by providing timing information for individual hits, and the additional information on the deposited energy in the sensor for individual particles.
A study on the shape characterization of single proton beam spots is performed to highlight the advantages of the high spatial resolution of the detector. N. Bauer supported the analysis process of this study in the scope of his Bachelor thesis. In addition, the measurement of dose linearity is tested by sampling the beam. The proof-of-principle studies on the characterization of the detector for daily QA measurements are published in I. Schilling *et al.* [19].
The usage of the additional information on the energy deposition per particle in the detector for proton beam energy determination is tested with various approaches: measuring the energy deposition spectrum of all protons or tracking the energy deposition of individual protons on their way through the detector. The results are published in I. Schilling *et al.* [20]. J. Hohmann and J. Wüller performed Monte Carlo simulations to verify the measurement analysis as part of their Bachelor's and Master's degree theses.
Moreover, an example of the applicability of the detector in the field of proton therapy is given by supporting a study of C. Behrends *et al.* [2] on the radiosensitizing effect of platinum nanoparticles with measurements performed by the ATLAS IBL Pixel detector.

The thesis is organized into 9 chapters. Following the introduction, chapter 2 provides an overview of the theoretical background of proton therapy. Particle detection with semiconductor detectors is introduced in chapter 3. The detector under study and the corresponding readout chip are presented in chapter 4. Chapter 5 introduces the survey on spot shape characterization. A presentation on sampled beam measurements to investigate the applicability of the detector for time-resolved beam characterization is given in chapter 6. Chapter 7 provides evaluated studies on using the measured energy deposition in the detector for proton beam energy estimation. As an example of the applicability of the detector in the field of proton therapy, the investigation of the impact of platinum nanoparticles on the energy deposition of protons at a macroscopic scale is presented in chapter 8. Finally, the main results of the thesis are highlighted, and an outlook is given in chapter 9. All supervised theses are listed at the end.

Chapter 2

Proton therapy

In this section, the theoretical background of proton therapy is discussed, starting with the interaction of protons with matter. In addition, two therapy facilities are presented with the corresponding beam delivery system. An overview of detectors commonly used in proton therapy later allows comparison with the ATLAS IBL Pixel Detector.

2.1 Interaction of protons with matter

Talking about the interaction of protons with matter, one commonly distinguishes between electromagnetic interactions with the atomic electrons or atomic nuclei and nuclear interactions. As an approximation, inelastic Coulombic interactions with atomic electrons result in a continuous kinetic energy loss of the protons without accountable deflection. The total energy deposition is mainly dominated by the excitation processes. In comparison, repulsive elastic Coulombic scattering of the protons with the heavier nucleus leads to a deflection from the original trajectory. [21]

Since the deflection from a single scattering process is almost always negligible, the observed deflection results from many tiny deflections referred to as multiple Coulomb scattering (MCS). The scattering angles of the protons after traversing an absorber are very nearly normally distributed due to the statistically independent scattering processes. The width of the angular distribution depends on the proton energy as well as the scattering material and thickness. Considering Highland's formula, the

associated standard deviation of the angular distribution θ_0 can be approximated [22]:

$$\theta_0 = \frac{14.1\,\mathrm{MeV}}{pv}\sqrt{\frac{L}{L_\mathrm{R}}}\left[1+\frac{1}{9}\log_{10}\left(\frac{L}{L_\mathrm{R}}\right)\right]\mathrm{rad}. \tag{2.1}$$

The formula is based on the kinematic factor pv, the target thickness L, and the corresponding irradiation length L_R. As a condition for the approximation, L has to be thin to preserve a nearly constant pv. In the scope of proton therapy applications the multiple Coulomb scattering leads to a lateral broadened beam width with increasing target depth.

Turning now to the mass stopping power $\frac{S}{\rho}$, which is defined to be the mean energy loss $\mathrm{d}E$ of ions per path length $\mathrm{d}l$ in an absorber with density ρ:

$$\frac{S}{\rho} = -\frac{1}{\rho}\frac{\mathrm{d}E}{\mathrm{d}l}. \tag{2.2}$$

It comprises the electronic stopping power $\left(\frac{\mathrm{d}E}{\mathrm{d}l}\right)_\mathrm{el}$ arising from inelastic collisions, the radiative stopping power $\left(\frac{\mathrm{d}E}{\mathrm{d}l}\right)_\mathrm{rad}$ due to the emission of bremsstrahlung, and the nuclear stopping power $\left(\frac{\mathrm{d}E}{\mathrm{d}l}\right)_\mathrm{nucl}$ caused by elastic Coulombic interactions.

Since the energy loss of protons in the clinically relevant energy range (up to about 250 MeV) is based on excitation processes, the electronic stopping power is dominating, analytically described by the Bethe-Bloch formula [23–26]:

$$\begin{aligned}\frac{S}{\rho} &\approx -\frac{1}{\rho}\left(\frac{\mathrm{d}E}{dl}\right)_\mathrm{el}\\ &= \frac{N_\mathrm{A}e^4}{4\pi\epsilon_0^2 m_\mathrm{e}c_0^2}\frac{Z}{A}\frac{1}{\beta^2}\left[\ln\left(\frac{2m_\mathrm{e}\gamma^2\beta^2}{c_0^2 I}\right)-\beta^2-\frac{\delta(\beta\gamma)}{2}-\frac{C(\beta\gamma,I)}{Z}\right].\end{aligned} \tag{2.3}$$

The latter equation includes the electron mass m_e, the velocity of light c_0, the elementary charge e, the vacuum permittivity ϵ_0, and the Avogadro constant N_A. The following parameters describe the material properties: the absorber material's mean excitation energy I, and the atomic number Z, just like the mass number A. Relativistic parameters are defined as $\beta = \frac{v}{c_0}$ and $\gamma = \frac{1}{\sqrt{1-\beta^2}}$. Corresponding to the particle energy and the absorber material, density correction $\frac{\delta(\beta\gamma)}{2}$, and shell corrections $\frac{C(\beta\gamma,I)}{Z}$ are applied. The Bethe-Bloch formula generally describes the

energy loss of heavy charged particles.

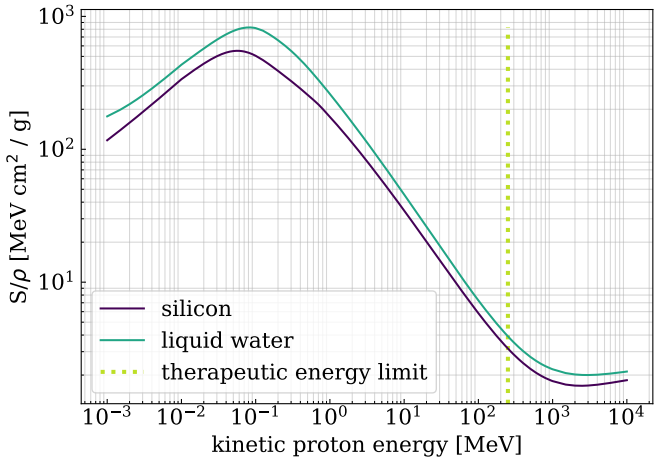

Figure 2.1: Mass stopping power of protons traversing silicon (purple) or liquid water (blue). The therapeutic energy limit of about 250 MeV is highlighted as dotted green line. The figure was reproduced with data from [27].

Depending on this, the mass stopping power of protons traversing silicon (purple) and liquid water (blue) is presented in Figure 2.1. The plot was reproduced with data from the NIST PSTAR database [27]. The therapeutic energy limit of about 250 MeV is highlighted as a dotted green line to illustrate the $\frac{1}{\beta^2}$ proportionality of the mass stopping power in this energy range.
To describe the mean energy delivered by ionizing particles $\mathrm{d}E$ absorbed per unit mass $\mathrm{d}m$, the dosimetric quantity absorbed dose D is used [28]:

$$D = \frac{\mathrm{d}E}{\mathrm{d}m}. \tag{2.4}$$

The absorbed dose along the depth in matter is referred to as the depth dose profile. Figure 2.2 illustrates the depth dose profile of a broad, monoenergetic proton beam in water, reproduced according to T. Bortfeld [29] with software provided by F. Mentzel [30]. The characteristic regions of the profile, also known as Bragg peak curve, will be discussed now.
The sub-peak region results from the $\frac{1}{\beta^2}$ proportionality of the stopping power in this energy range and nuclear interactions leading to the removal of protons and an increasing number of secondary particles. This region passes into the region with

the maximum dose deposition, namely the Bragg peak. The increased energy loss of the protons with decreasing energy while traversing matter leads to the peak of the absorbed dose near the end of the range of the protons, which ends with a sharp distal fall-off.
Bragg peak curves for different proton energies are superposed for the treatment of tumors in the clinics, resulting in a high dose plateau. The superposed depth dose profile is called spread-out Bragg peak (SOBP).

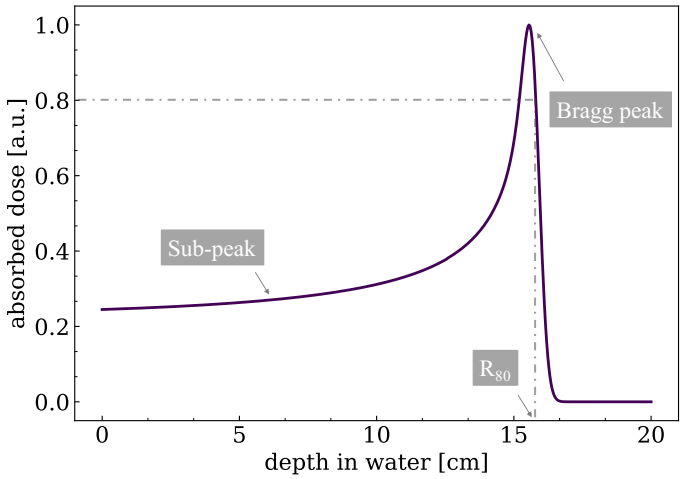

Figure 2.2: Depth dose profile of a broad, monoenergetic proton beam in water (reproduced according to [29], software [30]). The characteristic regions of the profile are labeled.

Statistical fluctuations of the energy loss result in the proton beam range being an average quantity. It can be defined as the depth at which 50 % of the initial protons have stopped and the absorbed dose drops to around 80 % of the maximum dose, respectively [31]. Based on this, the defined range is named R_{80}.
The projected range approximates the proton range in clinical applications when assuming a continuous energy loss and neglecting lateral scattering. In the case of a monoenergetic beam, the projected range can be approximated with the continuous slowing down approximation range (CSDA range), which characterizes the average path length of the protons till they stop [32]. The energies used for treating patients are based on the relationship between proton energy and range.

Water is a recommended material to mimic the interactions of protons with human tissue in clinics due to its properties in terms of energy loss, MCS, and nuclear interactions. Proton beam ranges are commonly determined in water phantoms, for example. Based on this, one can intuitively add or subtract objects of water in the beam path from the range. Therefore the range-absorbing power of various objects with thickness t_m is frequently described by their equivalent thickness t_w in water, referred to as water-equivalent thickness (WET). Assuming thin targets, the WET is given by

$$t_\mathrm{w} = t_\mathrm{m} \frac{\rho_\mathrm{m} \bar{S}_\mathrm{m}}{\rho_\mathrm{w} \bar{S}_\mathrm{w}} \text{ [33].} \tag{2.5}$$

Thereby, ρ_w and ρ_m describe the mass density of water and material, respectively, and $\bar{S}_\mathrm{m}$ and $\bar{S}_\mathrm{m}$ are the corresponding mean proton mass stopping power values.

Further details on the physical principles of proton therapy can be found in the literature [21, 34, 35].

2.2 Proton beam therapy system

The experiments presented in this thesis were performed at the West German Proton Therapy Centre Essen (WPE) and the University Proton Therapy Dresden (UPTD). Both facilities are equipped with an IBA Proteus Plus proton therapy system (IBA, Louvain-La-Neuve, Belgium). [13]
Therefore the generation of a therapeutic beam within the IBA Proteus Plus proton therapy system is described briefly; see [34]. The system is based on an isochronous cyclotron. In the center of the cyclotron, protons are injected by a hot filament Penning Ion Gauge (PIG) source. Enforced by a magnetic field, the protons traverse the cylindrical cyclotron on spiral-like trajectories in the round beam plane. Unlike a classical cyclotron, the magnetic field of the isochronous cyclotron increases with increasing radius and particle energies, respectively. The acceleration of the particles is realized by an alternating electric field with a fixed frequency induced between the two electrodes of the isochronous cyclotron. The number of cycles the protons must go through is adapted to the maximum energy required for proton therapy applications of about 228 MeV.

After the ejection of the protons out of the cyclotron, an energy selection system is used to reduce the energies in a range down to around 60 MeV. As a result, beam energies between 60 MeV and 228 MeV approximately are available to treat patients. The focused proton beam is transported to the treatment rooms within vacuum tubes consisting of dipole and quadrupole magnets. The beam delivery system at the exit of the beam, namely the nozzle, shapes the field and monitors the beam.
An overview of essential beam parameters: At a rate of 106 MHz, microbunches consisting of a round 100 protons are accelerated in regular therapy conditions (9.43 ns microbunch separation), leading to an approximate beam current of 2 nA or $1.24 \cdot 10^{10}$ protons/s at the nozzle exit. [11, 13].
There are fixed beam treatment rooms equipped with a horizontally mounted nozzle and others utilizing 360 ° beam rotation isocentric gantries. Depending on the utilized nozzle, different beam delivery techniques are available. [34]

2.3 Beam delivery technique

In order to adapt the narrow proton beam entering the nozzle to the three-dimensional target volume, the beam must be spread out accordingly in the lateral and longitudinal directions. Superposing beams with different ranges achieve the coverage of the target volume in the longitudinal direction. As an example, the concept of the SOBP was introduced previously.
The lateral field shaping differs for active and passive beam delivery systems. In passive systems like double scattering systems, for example, the beam is spread laterally using scattering devices mounted in the nozzle [36]. In the scope of this thesis, we will mainly refer to an active delivery technique, namely pencil beam scanning (PBS), where a narrow beam is scanned across the target in the three dimensions. Therefore the PBS technique will be presented in more detail now.

Compared to passive beam delivery systems equipped with scattering devices, active beam delivery systems do not spread the beam but focus it using quadrupole magnets. The single beams are called pencil beams with a shape that can be approximated by adopting a Gaussian intensity profile. Using the parameter

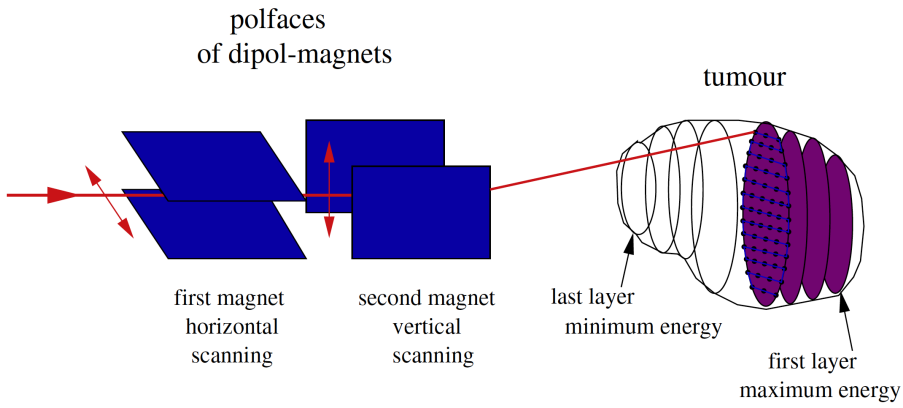

Figure 2.3: Schematic sketch of pencil beam scanning (PBS) delivery technique. [37]

σ = full-width half maximum/2.35, the width of the pencil beam spots can be described [38]. The pencil beams are scanned across the target volume using dipole magnets, see Figure 2.3. Due to the beam optics, the width sigma σ of the beam depends on the proton energy and varies from 3.1 mm for high energies to 5.5 mm for the lowest energy [39]. In contrast to passive beam delivery systems, the beam energy manipulation in the active beam delivery system cannot be performed in the nozzle but only in the upstream energy selection system. [40]
At WPE, the scanning is realized in discrete steps, referred to as the 'step and shoot' technique [41]. During the scanning, beam parameters like position, size, range, and intensity can be adjusted to achieve the prescripted dose distribution. Different energy layers are irradiated successively, commonly starting with the one having the most distal range.
With widths in the order of millimeters to centimeters, the pencil beams can cover complex target structures. Furthermore, the usage of apertures leads to sharper gradients at the field edges, further improving the dose conformality. [42]
Ionization chambers placed at the beam exit measure the dose and verify the position, size, and shape of the pencil beam spots during irradiation.
At the WPE, two treatment rooms are equipped with a PBS dedicated Nozzle (ProteusPlus system, IBA PT, Louvainla-Neuve, Belgium). Two other treatment rooms have installed a Universal Nozzle (ProteusPlus system, IBA PT, Louvainla-Neuve, Belgium).

2.4 Quality Assurance

The quality assurance (QA) procedures performed in proton therapy facilities depend on the beam delivery technique selected and vary from facility to facility. Recommendations and guidelines concerning the machine-specific QA are defined by the American Association of Physicists in Medicine's (AAPM) task group 224, summarized in Arjomandy *et al.* [38]. They identified the beam parameters that need to be checked and the recommended frequencies for performing the checks (daily, weekly, monthly, or annually).
This thesis focuses on the dosimetric QA for a PBS beam delivery system. Since the total dose distribution of PBS fields arises from the superposition of single pencil beams, the spacing and width of the beams have to be known to avoid deviations from the planned dose distribution [43]. An example of spot displacement's influence on the dose distribution is given by Arjomandy *et al.* [38]. They stated that during the production of a broad flat field, a displacement of $\approx 1.5\,\mathrm{mm}$ for one line of spots ($\sigma = 3\,\mathrm{mm}$) might result in dose errors of up to $20\,\%$. The same deviation occurs looking at errors in the spacing of the energy layers.
Since the spot size depends on the proton energy, the influence of deviation from the correct spot spacing on the dose distribution is a function of the energy and the beam size, respectively. B. Arjomandy *et al.* provide that a dose uniformity of $\pm 3\,\%$ can be achieved if the local shift of the individual spots falls below $13\,\%$ of the beam σ.
To account for the influence of the spot spacing and spot width on the dose distribution, the AAPM task group 224 recommends spot position tolerances of $\pm 2/\pm 1\,\mathrm{mm}$ for absolute/relative measurements during daily QA. In addition, the dose output constancy has to be within $\pm 3\,\%$, measured for different ranges on different days with one consistent field. Moreover, the range must be verified within $\pm 1\,\mathrm{mm}$.

2.5 Commonly used detectors

Specific properties of the proton beam can be measured with specially adapted detectors. In the following, an overview of commonly used detectors is given. The daily output constancy can be checked using parallel plate ionization chambers,

like the Advanced Markus Chamber (PTW, Freiburg, Germany) [38]. Furthermore, two-dimensional ionization chambers, such as the MatriXX detector (IBA Dosimetry, Schwarzenbruck, Germany), can perform beam output consistency checks and lateral profile investigations [44].
An overview of dose detectors appropriate for proton therapy applications is given by S. Giordanengo *et al.* [45]. The proton beam range can be estimated with an accuracy of up to 0.4 mm by measuring the depth dose distribution of the protons with multi-layer ionization chambers, like the Giraffe detector (IBA Dosimetry, Schwarzenbruck, Germany) [46, 47].
Radiochromic films or scintillation screens viewed through a CCD camera, like the Lynx PT (IBA Dosimetry, Schwarzenbruck, Germany), enable the characterization of the spot profile and position, respectively [48].
In order to reduce the time-consuming procedure of measuring all parameters with different devices during the daily QA, various combined systems are currently in operation. A set of wedge-shaped phantoms like the Sphinx (IBA Dosimetry, Schwarzenbruck, Germany) coupled with a detector like the Lynx PT is suggested to improve the efficiency of daily QA for PBS proton therapy, in particular, to verify energy and range consistency, respectively [49, 50]. The advancement of this detector system is called Sphinx Compact (IBA Dosimetry, Schwarzenbruck, Germany) and consists of wedge-shaped phantoms combined with a photo-diode flat-panel detector. Additionally, equipped with a PPC05 parallel plate chamber (IBA Dosimetry, Schwarzenbruck, Germany) for machine output measurements, all parameters for the PBS daily QA recommended by AAPM TG224 protocol can be determined [51].
Another device used for QA measurements is the Sun Nuclear QA3 device (Melbourne, Florida, USA), initially designed for routine QA in photon and electron radiotherapy beams. The detector system consists of multiple Precision SunPoint diodes and parallel plate ionization chambers and enables a daily QA of the proton therapy gantry in less than 30 minutes. [52, 53]

Chapter 3

Silicon particle detectors

Characterizing and measuring particles in HEP experiments, like in the ATLAS detector at CERN, requires advanced and continual detector development. Silicon pixel detectors provide an excellent spatial resolution best fitting for tracking charged particles. This chapter summarizes the physical principles on which particle detection with semiconductor detectors is based.

3.1 Detectors in High Energy Physics

HEP experiments are designed to answer essential questions about the constitution of matter and radiation. The description of the fundamental particles and their interactions is predicted by the Standard Model (SM). Still, some questions remain unanswered, like the explanation for dark energy or the existence of particles that have not yet been discovered. In order to investigate the origin of matter and to expedite fundamental research related to the universe, the two-ring superconducting hadron accelerator and collider Large Hadron Collider (LHC) was built at the European Organization for Nuclear Research (CERN) close to Geneva [54].
Before their injection into the 26.7 km long LHC, two proton beams are accelerated by an accelerator chain to an energy of 450 GeV. Subsequently, accelerating structures in the ring increase the final protons' energy up to center-of-mass energies of 13 TeV. When the two opposite high-energy hadron beams collide, particles like τ-leptons, B-hadrons, and many others are produced, replicating similar conditions as in the Big Bang. A peak luminosity of approximately $2 \times 10^{34}\,\mathrm{cm}^{-2}\mathrm{s}^{-1}$ was achieved in 2017. Luminosity describes the number of collisions. [55, 56]
The produced particles are then characterized in different experiments at the LHC,

that provide information of which particle and track was passing through them. One ground-breaking discovery in the LHC was in 2012 when two of the experiments confirmed the evidence of the Higgs-Boson [57, 58].
The A Toroidal LHC Apparatus (ATLAS) detector was one of those experiments involved in the Higgs-Boson discovery. It was constructed at one of the four interaction points at the LHC, where the proton beams collide [59]. The general-purpose particle detector experiment ATLAS consists of multiple detector layers that cover the maximum volume for particle identification. The detector system is arranged cylindrically around the interaction point with discs called end-caps for maximal coverage. Nearby the interaction point, the first detector component is aligned, consisting of a tracking system. The tracking system can extract the vertex and momentum information using an applied magnetic field that bends charged particles giving information about the charge. At a larger radius of the beamline, electromagnetic and hadronic calorimeters are installed for energy measurements. The outer component of the detector, the so-called muon detector, identifies muons.

The detector system used in this study is designed as a part of the vertex detector for the innermost detector layer close to the beam pipe, named Insertable B-Layer (IBL), installed in the ATLAS detector at 2014 [17, 60]. The IBL consists of pixelated silicon detectors with pixel sizes of $250\,\mu\text{m} \times 50\,\mu\text{m}$ bump bonded to a read-out chip, that give good tracking performance with excellent spatial resolution. The detectors are called ATLAS IBL Pixel Detectors.
Due to their arrangement close to the interaction point, the detectors have to be radiation robust. They, therefore, are designed to withstand a radiation dose of 2.5 MGy and a non-ionizing fluence of $5 \times 10^{15} \text{n}_{\text{eq}}/\text{cm}^2$ [61]. In order to introduce the operating principle of the pixelated ATLAS silicon detectors, the theoretical background of particle detection with semiconductor detectors and the detailed layout of the detector are summarized in the following sections of this chapter.

3.2 Conduction in silicon

Nowadays, silicon is established as one standard material for tracking detectors in HEP due to impressive features like the ability to work in extreme environmental

conditions and the good resolution for spectroscopy measurements. Detailed descriptions exceeding the explanation of semiconductor sensors in this thesis can be checked in the literature; see [26, 62–64].
Silicon crystallizes with a diamond lattice structure. By forming covalent bonds, four valence electrons of each atom are shared with the neighboring atoms. Influenced by the neighboring atom, the energy levels of the electrons split into energy states, grouped as energy bands with gaps between them.
In an attempt to expound the band structure of a semiconductor, the energy bands filled with electrons at a temperature of absolute zero must first be considered. The highest occupied band at this temperature is referred to as the valence band. Due to thermal excitation or the usage of an external electric field, the electrons can be shifted into the higher energy band, called the conduction band. The electrons are free to move in this band and therefore participate in electric conduction.
The excitation of an electron, which implies the break of the covalent bonds, requires an energy amount of at least the difference between the highest energy level of the valence band and the lowest energy band of the conduction band, namely band gap energy. At room temperature (300 K) and normal pressure (1 bar), silicon has a band gap energy of 1.12 eV [63], whereas the average energy sufficient to create an electron-hole pair is 3.6 eV [26, 65]. The energy deviation occurs because silicon is an indirect semiconductor, meaning there is a difference between the crystal momentum of the valence band's maximum and the conduction band's minimum. Therefore an additional momentum transfer to the lattice is mandatory.
The band structure model can explain the impact of temperature and pressure changes on silicon conduction. With increasing temperature or pressure decreases the band gap width [64]. The band gap width determines the applicability of the material for usage in particle detectors.
For example, the band gap in silicon is larger than in germanium, resulting in potentially higher operation temperatures. On the other hand, the energy sensitivity and resolution are better for germanium due to the lower energy required for electron-hole pair creation. Additional advantages of silicon are the lower price and a faster signal formation caused by the higher mobility of the electrons compared to germanium. [66]

3.3 Doping and p-n junction

One can intentionally alter the conduction properties of the semiconducting material by inserting impurities into the crystal lattice, referred to as doping. The type of the inserted material determines whether an n-type or p-type semiconductor is obtained. Materials from the fifth element group as so-called donor atoms with five valence electrons, like arsenic or phosphorus, result in n-type doped silicon, illustrated in Figure 3.1(a). The additional valence electron of the donor atom only weakly bonds to the atom via electrostatic forces and not in the covalent bond. Therefore it can be easily ionized and participates in conduction afterward.
In comparison, extra holes can be inserted by replacing a silicon atom with so-called acceptor atoms from the third element group, like boron, holding only three valence electrons. The bond representation of the resulting p-type doped silicon is shown in Figure 3.1(b). Compared to the number of valence electrons per silicon atom, the missing electron causes a hole in one covalent bond. Due to doping, additional energy levels are introduced in the silicon, but the total charge remains unaffected.
Bringing a p-type and an n-type semiconductor together forms a p-n junction,

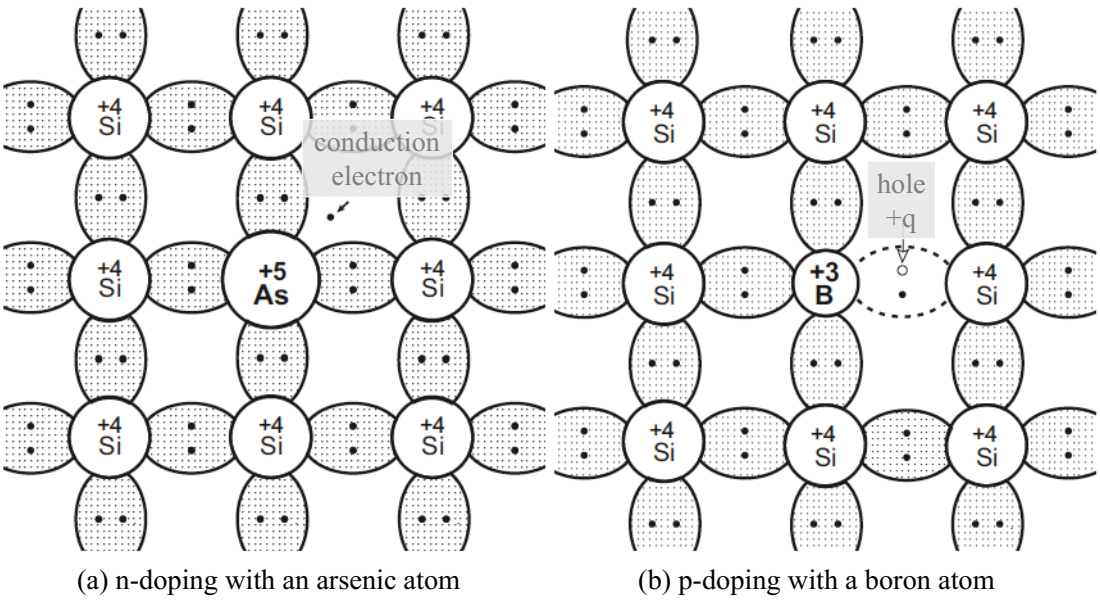

Figure 3.1: Schematic bond pictures for (a) n-type silicon doped with an arsenic atom and (b) p-type silicon doped with a boron atom. (modified from [64])

creating a concentration difference of electrons and holes for both sides. Consequently, diffusion of the electrons into the p-type region and the holes into the n-type region occurs, generating the diffusion current I_{diff}. The recombination of the electrons and holes forms an area lacking mobile charge carriers, the so-called depletion zone. Furthermore, the remaining immobile charged ions build up space charges, creating a potential difference resulting in an electrical field that counteracts the movement of the charge carriers, forming the drift current I_{drift}. The drift and diffusion current are in thermal equilibrium if no external bias voltage is applied. They define the built-in voltage V_0 and the width of the depletion zone, respectively. The discussed considerations are also valid for normal and highly doped regions of the same type, like n^+-n or p^+-p junctions.

3.4 Particle detection with silicon sensors

On closer consideration of the thermal equilibrium of a p-n junction shown in Figure 3.2(a), the depletion zone's width depends on the semiconductors' initial doping concentration. Furthermore, the width of the depletion zone w is adjustable by applying an external bias voltage U_{ext} with well-chosen polarity and voltage.

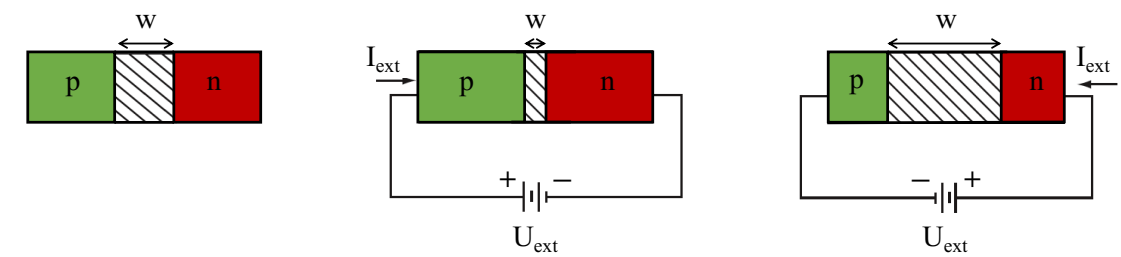

(a) Thermal-equilibrium condition.

(b) Forward-bias condition.

(c) Reverse-bias condition.

Figure 3.2: Adjustment of the depletion zone of a p-n junction under various biasing conditions. (modified from [26])

Applying a higher potential to the p-side in contrast to the n-side leads to a forward biasing of the semiconductor junction resulting in an increasing I_{diff} exceeding I_{drift}. As a consequence, the width of the depletion zone decreases, as outlined in

Figure 3.2(b). To enlarge the depletion zone, a negative U_{ext} has to be applied to the p-side, referred to as reverse biasing and shown in Figure 3.2(c).
The measurement of ionizing particles with a semiconductor detector is based on creating electron-hole pairs in the material. If the electron-hole pair is created in the depletion zone, they do not recombine, and due to the electrical field, they drift and induce a signal after the acceleration to the electrodes. On that account, a semiconductor particle detector is operated in reverse bias to generate the largest depleted volume possible through the total thickness of the sensor.
The bias voltage to fully deplete a sensor of thickness d is referred to as depletion voltage V_{depl}. Depending on the acceptor concentration N_A and the donor concentration N_D, as well as on the built-in voltage V_0, V_{depl} can be described using the equation

$$-V_{\mathrm{depl}} = \frac{e}{2\epsilon\epsilon_0}\left(\frac{N_A N_D}{N_A + N_D}\right) d^2 - V_0, \tag{3.1}$$

where $\epsilon\epsilon_0$ is the permittivity of silicon [64].

As particle detection with silicon sensors is based on their interaction with matter, a summary of the main interaction processes for various particles is given. Photons primarily interact with silicon through the photoelectric effect, Compton scattering, or pair production. The electrons released in these interactions can be detected subsequently. In contrast, other non-charged particles like neutrons can only be detected with silicon sensors when passing through additional converter material. The latter is required to generate photons, or charged particles, that can be detected in the silicon.
The energy loss of charged particles with lower energies is mainly due to collision effects, meaning the excitation and ionization of atoms. A detailed discussion on the interaction of protons with matter is provided in section 2.1. In contrast, charged particles with higher energies lose energy primarily by radiation effects like Bremsstrahlung.

A leakage current I is generated as a function of the applied external voltage, consisting of a surface and a bulk-generated current. The impact of the surface-caused current is usually small and results from depositions or damages on the surface.

If the surface of the sensor is scratched or contaminated, the surface-generated current increases.
Compared to that, the bulk current is mainly generated by thermal excitation and electron-hole pair generation in the depletion zone and can be described as

$$I(T) \propto T^2 \exp^{-\frac{E_g(T)}{2k_B T}}, \tag{3.2}$$

using the band gap energy E_g, the Boltzmann constant k_B and the temperature T. Since the volume of the depletion zone depends strongly on the bias voltage, the bulk current does as well.
Moreover, the leakage current increases with radiation damage [67]. More detailed information on radiation damage in silicon sensors is given in the literature [26, 63, 68]. High fluences of high energy particles can generate defects in the sensor crystal lattice that lead to irreversible radiation damage. The defects created by radiation damage increase the leakage current, which implies an increased generation of charge carriers and noise. Therefore the signal-to-noise ratio gets worse, which has to be avoided during the experiment.
In addition, an increased leakage current and, thus, an increasing power consumption heat the sensor, leading to a further rise in the sensor's temperature and leakage current in the order given. Since the readout electronics have a limited leakage current tolerance and the breakdown voltage of the sensor should not be exceeded, the detector has to be cooled during the operation of the experiment [1]. Furthermore, crystal defects induced by radiation damage lead to the trapping of charge carriers and thereby reduce the charge collection efficiency [69].
Considering the impact of radiation damage, developing a particle detector has to be adapted to the expected particle fluence in the measurement environment. The quantity of neutron equivalent per square centimeter (n_{eq}/cm^2) is used to scale up the damaging effects of various particles to the impact of neutrons with an energy of 1 MeV. Since the detector under study is designed for usage in a radiation-hard environment close to the interaction point of the ATLAS experiment, it is tested for excepted particle fluences up to $5 \times 10^{15}\, n_{eq}/cm^2$.

Chapter 4

ATLAS IBL Pixel Detector

As introduced in section 3.1, ATLAS IBL Pixel Detectors are designed to track particles in the ATLAS experiment at CERN. In order to do so, the detector requirements are high spatial resolution, radiation robustness, and an excellent hit efficiency in the active area of $> 97\,\%$ [17]. For this reason, the ATLAS IBL Pixel Detector is designed to withstand a radiation dose of 2.5 MGy and a non-ionizing fluence of $5 \times 10^{15} \mathrm{n_{eq}}/\mathrm{cm}^2$ [61]. The high spatial resolution is realized by choosing a pixelated detector with small pixels.
Pixelated semiconductor detectors are currently built either as monolithic detectors or hybrid detectors. An overview and evaluation of the different sensor technologies is given by N. Wermes [70].
The device under study is a hybrid pixel silicon detector consisting of a readout chip and a pixelated silicon sensor connected via so-called bump bonds. The separated processing enables tests and optimization of the detector components independently. The following sections present the sensor technology and the readout chip to meet the listed detector requirements. Additionally, the experimental setup and data processing procedure is outlined.

4.1 Hybrid Pixel Modules

The first step to constructing a hybrid pixel module is to connect each sensor pixel to a pixel of the readout chip via bump bonds. The hybridization process of the pixel modules investigated in this thesis corresponds to the hybridization process of the IBL modules described by the ATLAS IBL Collaboration [71]. After running

through the hybridization process, the device is called a bare module.

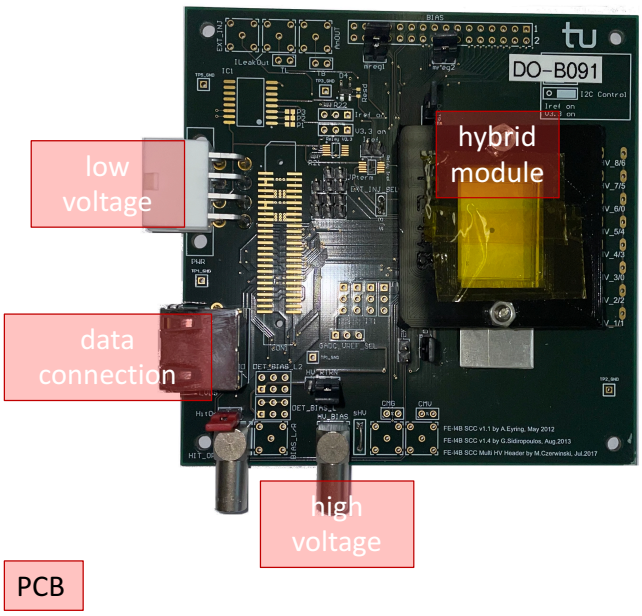

Figure 4.1: PCB loaded with bare module. Signal and power connectors are highlighted.

The second construction step is the gluing and wire bonding of the bare module onto a printed circuit board (PCB), which provides the signal and power lines for the operation. In contrast to the flexible PCBs used in the ATLAS experiment, rigid PCBs are utilized because they provide mechanical robustness in the measurements. After finishing the two construction steps, the device is referred to as a hybrid pixel module, shown in Figure 4.1. In addition, the PCB holds an 8-pin Molex connector for the low voltage supply, the data transmission connector, and the connector for the bias (high) voltage power supply.
A detailed introduction of the main components of the hybrid pixel module, namely the sensor and the readout chip, follows this chapter.

4.2 Sensor technology - planar n-in-p

The sensors used to set up hybrid silicon pixel detectors consist of an n- or p-type doped silicon bulk with n^+- or p^+- silicon layers on top and beneath it to implement

the pixelated readout electrodes. Out of these four compositions, only the sensor technologies n-type silicon bulk with n^+-doped pixel implantations, called n^+-in-n, and p-type silicon bulk with n^+-doped pixel implantations, called n^+-in-p, uses the electron signal instead of the signal induced by the holes. One can take advantage of the higher mobility and the lower trapping probability of electrons compared to holes in silicon. For clarification, the production of electron-hole pairs in an n^+-in-p sensor released by the incidence of an ionizing particle is outlined in Figure 4.2(b). In the scope of this thesis, pixelated n^+-in-p sensors are used. An additional advantage of this sensor technology is that only one side of the sensor has to be segmented, which leads to fewer production costs than processing a double-sided wafer [72, 73]. See the thesis of J-C. Beyer [74] for a detailed introduction to sensor manufacturing. As established in section 3.4, the depletion zone in n^+-in-p sensors grows from the n^+-pixel implantation to the p^+-implant on the backside if a negative bias voltage is applied to the backside during measurement, shown in Figure 4.2(a).

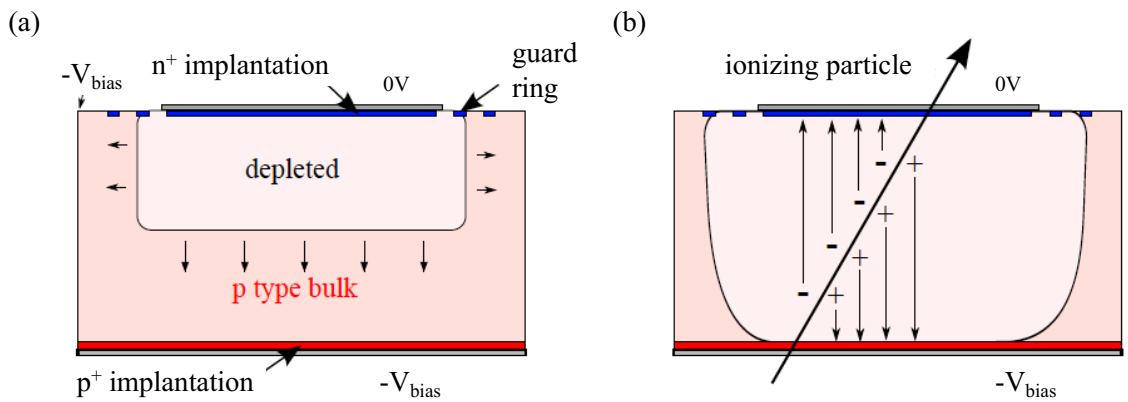

Figure 4.2: Schematic cross-section of an n^+-in-p silicon sensor to illustrate the growth of the depletion zone with an increasing bias voltage (a) and the detection of an ionizing particle (b). [75]

The measurements presented in this thesis were performed using various pixelated silicon sensors with a thickness of 100 µm or 200 µm. Pixels with a pitch of 250 µm × 50 µm are arranged in a matrix of 80 × 336 pixels, 26880 pixels in total, with an area of 2.00 cm × 1.68 cm.
In order to exploit the existing work on optimizing the pixel design for HEP experiments, the utilized sensors are based on the IBL sensor pixel design [76]. A detailed

explanation of the fundamental design of ATLAS pixel sensors using the example of an n^+-in-n sensor is given in the thesis of T. Wittig [75].

4.3 Readout chip FE-I4B

The readout chip amplifies and digitizes the signal induced in the pixel electrodes. In this study, all detectors are equipped with the FE-I4B readout chip, initially designed for the ATLAS IBL detector [1, 18]. The chip is produced with a commercial 130 nm feature size complementary-metal-oxide-semiconductor (CMOS) process and is segmented with the same pixel matrix as the sensor introduced in the previous section.

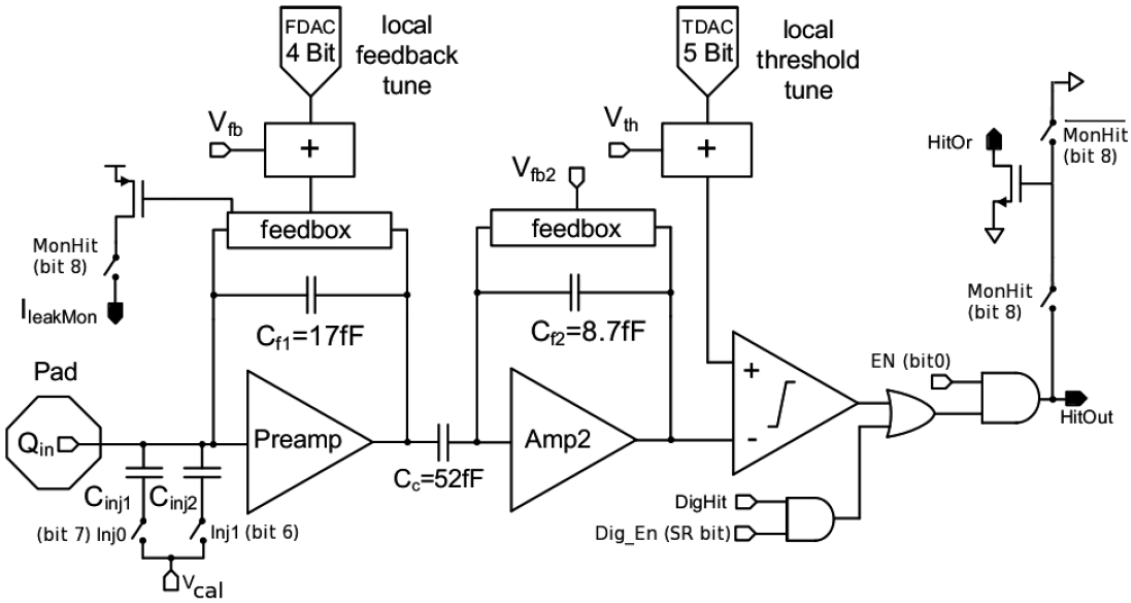

Figure 4.3: The analoge circuit for one pixel cell depicted as a schematic diagram [1].

Figure 4.3 illustrates a schematic diagram of the analog circuit for one pixel cell. The bump pond pad (Pad) is the connection to the pixel electrode to receive the signal generated in the sensor. Then, a two-stage amplifier amplifies the signal for processing with the discriminator. If the signal exceeds the discriminator threshold generated by a voltage generator, the Time over Threshold (ToT) is measured in

units clock cycles of 25 ns, called bunch crossing units (BCUs). Figure 4.4(a) shows the stages of conversion from the analog to the digital signal for two charge pulses of different heights. The charge pulses for a particle that deposits more energy in the sensor (blue) and a particle generating a smaller energy deposition (purple) are processed by the preamplifier resulting in two voltage signals with different amplitudes and duration, shown in the second plot. The discriminator output is shown in the third plot.

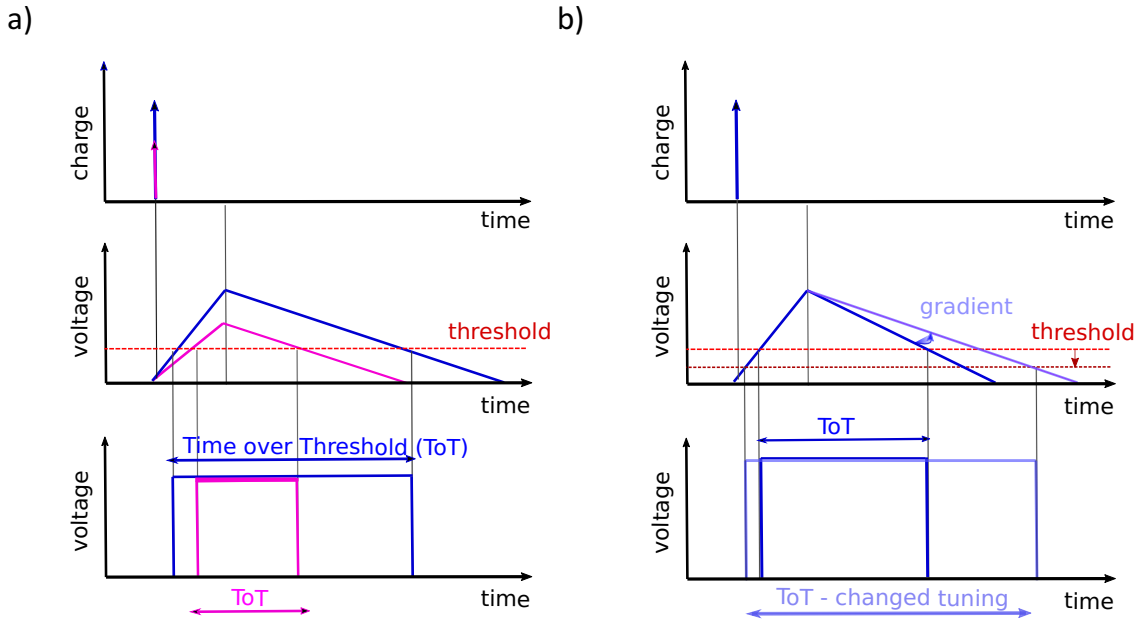

Figure 4.4: Conversion of the analog signal to the digital Time over Threshold (ToT) signal. The signal conversion for various charge pulses (a) and for different tuning settings (b) are illustrated.

The rising signal of the voltage pulse intersects the threshold level at different times corresponding to the pulse heights. The intersection with the threshold level takes place earlier in time for large signals, highlighted blue in Figure 4.4, than for small signals. Accordingly, the start of the ToT measurement is delayed for the smaller signal, commonly known as the time-walk effect. The time-walk effect shortens the ToT signal. [77]

The ToT information in BCUs is stored as 4-bit code. In order to associate small hits with the correct bunch crossing, one can make use of the implemented hit discard configuration (HitDiscCnfg) register. Setting HitDiscCnfg to zero leads to

a measurement of all hits assigned to the bunch crossing when the hit occurs. In comparison, HitDiscCnfg set to 1(2) means that small hits below a ToT of 0(1) are classified as small hits if they occur within the window of 2 bunch crossings after a big hit. Otherwise, they will be discarded. Depending on the chosen HitDiscCnfg setting, the stored 4-bit ToT code is transferred to the actual ToT values. The correlation between the ToT code and the $\mathrm{ToT}_{\mathrm{True}}$ for the HitDiscCnfg register settings is listed in Table 4.1.

Table 4.1: Correlation between the 4-bit stored ToT values (hex) and the true ToT for the HitDiscCnfg register settings 0, 1, and 2. [1]

True ToT [BCUs]	HitDiscCnfg 0	1	2
below threshold	F	F	F
1	0	E	E
2	1	0	E
3	2	1	0
4	3	2	1
5	4	3	2
6	5	4	3
7	6	5	4
8	7	6	5
9	8	7	6
10	9	8	7
11	A	9	8
12	B	A	9
13	C	B	A
14	D	C	B
15	D	D	C
≥ 16	D	D	D

Particles that generate signals remaining below the discriminator threshold are counted as 'below threshold'. In contrast, particles depositing more charge per pixel

in the sensor than that assigned to ToT 12 (C) are stored as 'overflow hits' in ToT 13 (D). The correlation between the ToT and the deposited charge in the sensor will be discussed in section 4.5 extensively.
Since the readout chip is developed for HEP experiments, the recommended maximum charge that can be processed is 100000 electrons. The external clock input has a frequency of 40 MHz. To operate the readout chip the analogue circuit requires 1.5 V and the digital circuit 1.2 V nominal voltage, applied externally during the measurements described in this thesis.
During the measurement, the hit information, ToT information, and time counter information are stored in digital regions. The latter is a formation of four pixels which is read out as one. Subsequently, after storing the event information in the digital units, either a trigger signal starts the data acquisition, and the data is sent off the chip via serial Low-Voltage Differential Signaling (LVDS) output, or the event is discarded.
More detailed descriptions of the readout chip functionalities can be found in the corresponding manual [1].

4.4 Readout system

Hybrid modules equipped with FE-I4B readout chips can be operated using multiple readout systems. One of them is the *USBpix* [78, 79] system, which was chosen for the operations presented in this thesis. Data acquisition using the system is described in the following.
The readout system consists of a Multi-IO board (MIO2) connected to a single chip adapter card (SCA), be seen in the photo in Figure 4.5. In addition, other adapter cards enable the operation of multiple modules, but they are not introduced in this thesis.
The major components of the MIO2 board are the field programmable gate array (FPGA) for communication with the FE-I4B readout chip and a USB microcontroller. SRAM provides an extension of 16 Mbits to the FPGA memory. Moreover, the 40 MHz clock of the readout is generated, and connectors for trigger generators and a 'Trigger Logical Unit (TLU)' [80] are provided next to the USB port for communication with the laptop.

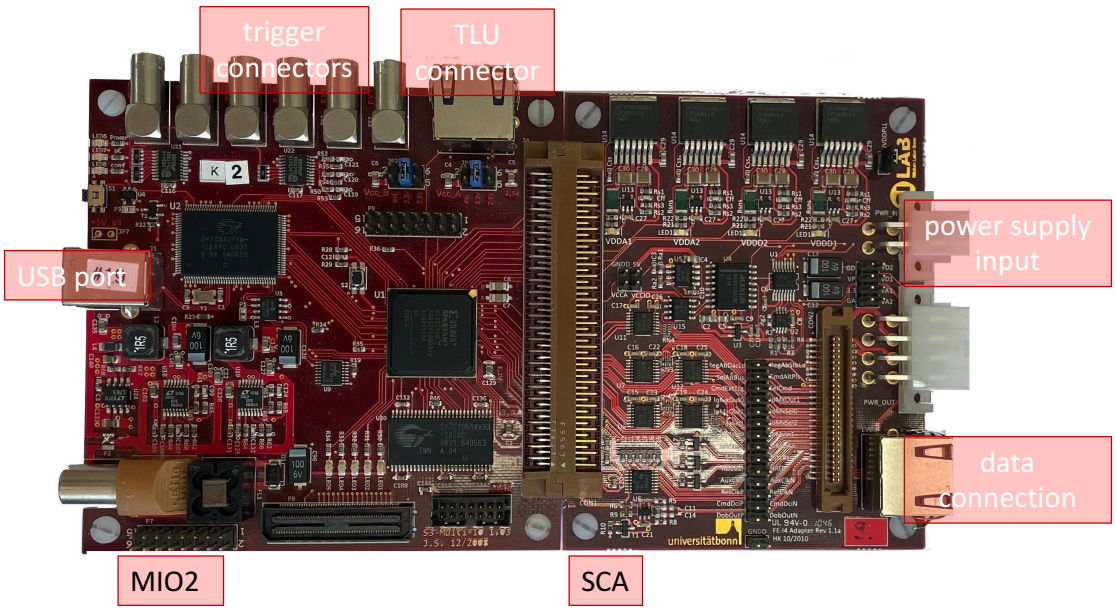

Figure 4.5: USBpix setup consisting of a Multi-IO board and a single chip adapter card.

The connection from the SCA to the hybrid module is given via Ethernet. Apart from this, a power supply connector allows the application of 2 V external voltage to power the readout hardware.

4.5 Tuning of the readout chip

Before an experiment, all pixels' responses must be adjusted depending on the expected deposited charge of the particles to measure in the sensor. In other words, registers of the readout chip need to be adjusted so that the preamplifier and discriminator of each pixel operate in a limited range. This procedure is called 'tuning' and sets the range of deposited energies that can be measured with the detector. In order to tune the readout chip, a signal can be induced by charging both injection capacities, highlighted in the analog circuit in Figure 4.3. The feedback current of the amplifier and the local threshold of the discriminator generated by a voltage generator can be adjusted independently during tuning.
There are global settings to adapt the response of all pixels and local settings for

the adjustment of individual pixels. By way of illustration, Figure 4.4(b) shows the impact of tuning on the conversion stages from the analog to the digital signal. Optimizing the feedback current regulates the falling slope of the voltage signal. The discriminator output visualized in the third plot presents the different ToT outputs for the same signal processed with different tuning settings.

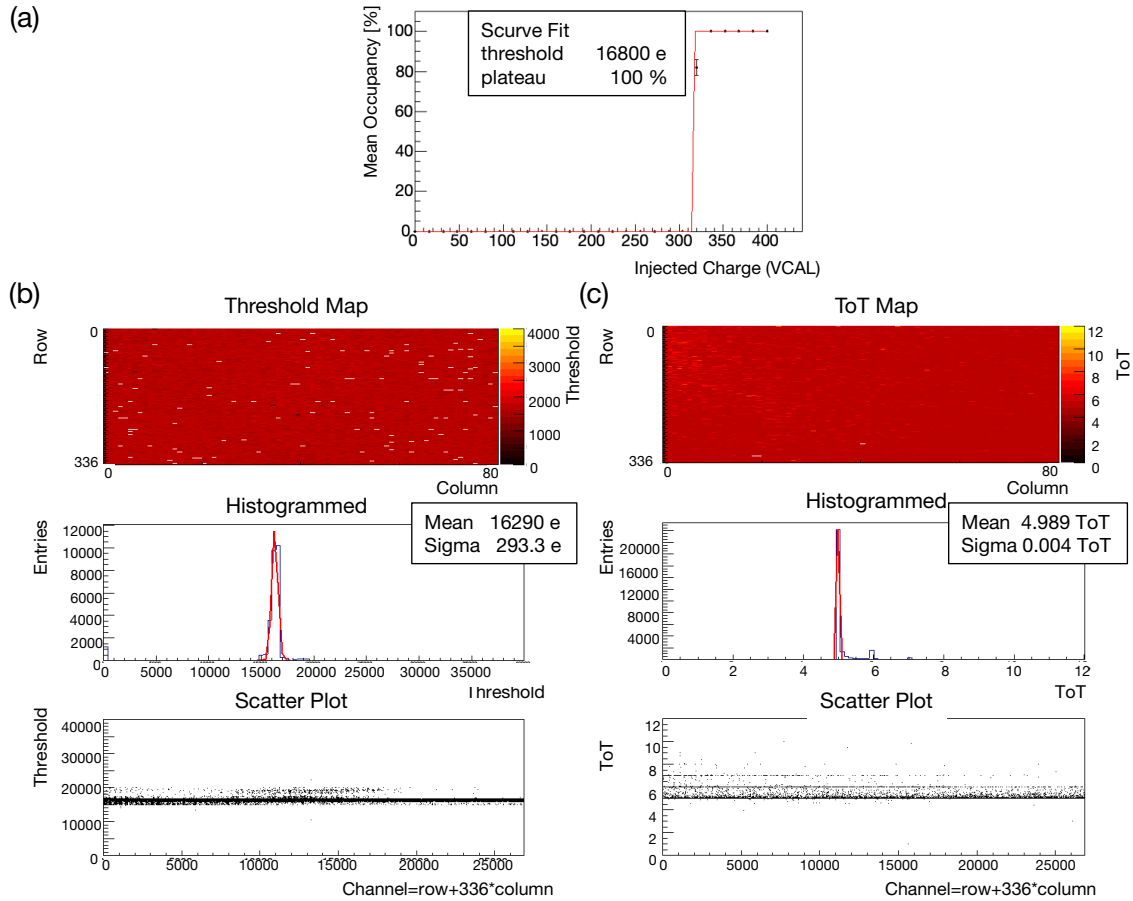

Figure 4.6: STcontrol results for a threshold scan (a and b) and a ToT verify scan (c) performed with a module tuned to a threshold of 17 ke and a ToT response of 5 for a reference charge of 60 ke. The results are illustrated as a map, histogrammed, and as scatter plot. The mean occupancy for one pixel as a function of the injected charge and the corresponding error function fit to determine the threshold value is shown in (a).

The software STcontrol [81] has been developed at Göttingen University to operate the hardware and update the firmware of the readout system via a graphical interface. It enables the verification and adjustment of configuration parameters by

the performance of specific scan and tuning algorithms. Among other things, the digital-to-analog converter (DAC) settings are adjusted to control the amplifier stage and the discriminator and thus set the tuning. Previous theses have extensively studied various scans and tuning algorithms [74, 82]. The scans to validate the tuning parameters are listed afterward to give a short overview.

- *analog and digital scan*: Used to check the functionality of the amplifier (analog scan) and discriminator (digital scan) of every pixel. Therefore a defined charge can be injected multiple times directly into the discriminator or amplifier by external charge injection circuits. Comparing the number of charge injections per pixel and the readback allows identifying noisy (more measured hits than injected) or dead (no hits) pixels. Based on the analog scan results, the dead and noisy pixels are masked out for subsequent scans.

- *threshold scan*: Performed to verify the threshold setting by injecting test charges (controlled by the *PlsrDAC*) and analyzing the pixel response. The expected discriminator response as a function of the injected charge can be described by a step function convoluted with a Gaussian function, referred to as an error function, to account for electronic noise. For example, Figure 4.6 illustrates the results for the varying scans plotted in STcontrol performed with a module consisting of an FE-I4B readout chip bump bonded to a 100 µm thick silicon sensor. The module is tuned to a threshold of 17 ke and a ToT response of 5 for a reference charge of 60 ke. The upper plot (a) presents the mean occupancy after injecting the same charge 100 times as a function of different injected charges (VCAL) for one specific pixel. The error function fitted to the mean occupancy is highlighted in red.
  Out of this data, every pixel's threshold is defined as the charge induced to achieve 50 % occupancy. The threshold distribution for all pixels is histogrammed in Figure 4.6(b) with the corresponding threshold map and scatter plot.

- *ToT verify scan*: Designed to verify the tuned ToT response for a specific injected charge. Several times, a specific charge is injected to determine the mean response ToT for all pixels. The verify scan results for the exemplary tuned module introduced previously are shown in Figure 4.6(c). A small second

peak for a ToT of 6 is visible, which could be avoided with an additional ToT adjustment to improve the uniformity of the ToT values.

4.6 ToT Calibration

Turning to the measurement results, the ToT can be converted into charge values for a specific tuning to investigate the amount of deposited charge in the sensor. 10-bit so-called PlsrDAC values control the amplitude of the voltage applied to the injection capacitors during tuning. The PlsrDAC values have to be calibrated to the injected charge and the corresponding ToT values for every pixel. A novel ToT calibration procedure was developed within the scope of the master thesis of Julia Rieger [83], described in the following.
Starting with a single pixel, a specific charge is injected into the pixel by varying the PlsrDAC value step by step. The resulting pixel answers are the ToT code values in the range from 0 to 12. Considering the chosen injection capacitor, a conversion factor, and a calibration offset, the PlsrDAC values can be converted into the injected charge Q.
The correlation between the average injected charge and the ToT values for every pixel can be described by a second-order polynomial, as shown by the equation

$$Q = a + b \cdot \mathrm{ToT} + c \cdot \mathrm{ToT}^2, \tag{4.1}$$

using the parameters a, b, and c. This procedure is repeated for all pixels.

Performing the ToT calibration for a module with the same tuning introduced in the previous section, for example, Figure 4.7 shows the averaged mean charge over all pixels Q_{mean} corresponding to the ToT values. The uncertainty on Q_{mean} is defined as the all pixels' standard error of the mean (SEM) of Q. According to Equation 4.1, a second-order polynomial is fitted to the data.

Typically the individual tuning of the detector is described by the threshold and a specific ToT value. In the case of the chosen example, the threshold is 17.000 electrons,

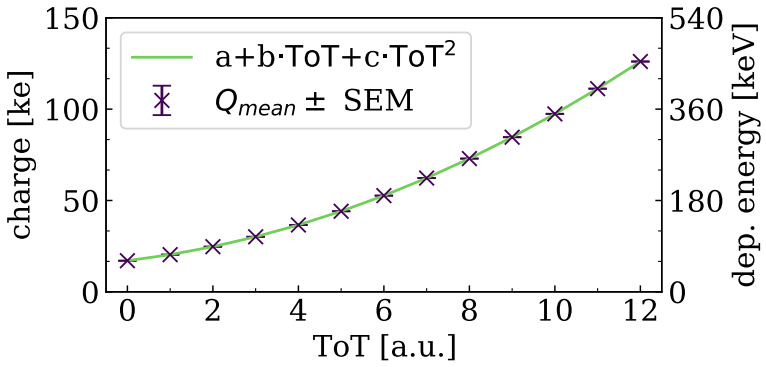

Figure 4.7: Averaged mean charge Q_{mean} over all pixels in dependence of the ToT values for the tuning *17ke5ToT@60ke*. According to Equation 4.1, a second-order polynomial is fitted to the tuning data. The second y-axis on the right side illustrates the conversion from deposited charge to deposited energy.

and 5 ToT corresponds to a reference charge of 60.000 electrons. Based on this, the tuning settings are designated as *17ke5ToT@60ke*.

Moreover, Figure 4.7 clarifies the dependence between the tuning settings and the deposited energy range of the detector. Looking at the tuning of *17ke5ToT@60ke*, particles depositing a charge in silicon lower than 17 ke cannot be detected. The ToT settings set the limit of the deposited energy range of the detector. Particles generating more charge than Q_{mean} for ToT 12 per pixel in the sensor are counted as overflow hits.

Since the average energy to create an electron-hole pair in silicon is 3.6 eV, the charge values can be converted into deposited energy by multiplying it with the latter. This conversion is illustrated by the second y-axis in Figure 4.7. It becomes clear that the chosen tuning can only be used to detect particles that deposit energies in the range of $\approx (61 - 454)$ keV in the 100 µm thick silicon sensor. Therefore, the tuning of the readout chip has to be adjusted for the expected energy deposition of the particles under study.

4.7 Experimental Setup

In summary, the experimental setup to perform measurements with the pixelated ATLAS IBL detector consists of the module on the PCB board, the corresponding power supplies to provide the analog, digital, and depletion voltages, the USBPix readout system with the connected power supply, a trigger generator, and a laptop. A sketch of the setup is illustrated in Figure 4.8.

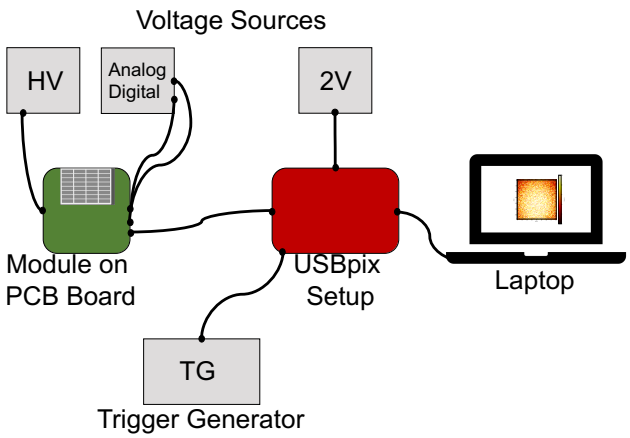

Figure 4.8: Setup to operate the detector consisting of the hybrid detector, the USBpix board, the power supplies, the trigger generator, and a laptop.

There are two ways to trigger the data acquisition of the FE-I4B readout chip. On one side, the self-triggering, which means that the measured events also release the trigger command. On the other side, external triggering, where an external signal starts the data acquisition generated by a frequency generator or another detector. In the context of this work, only external triggering is used to know the time intervals between the individual trigger signals. The maximum sustainable trigger rate is 200 kHz [1].

Furthermore, the number of trigger pulses sent following a trigger command is adjustable from 1 to 16 spaced by one clock (25 ns). Adjusting the number of trigger pulses per trigger command is implemented by setting the trigger count (TrigCnt) parameter from 1 to 16. This feature is implemented to scale the sensitive time of the detector.

The measurements discussed in this thesis were performed at different proton therapy facilities. Depending on the measurement requirements, the trigger signal is produced either by a fixed frequency generator or an external scintillation detector. Before the sections discussing the individual measurements, the setup settings will be presented in detail.

4.8 Processing and clustering of data

The measurement duration is set by the number of trigger commands that should be applied. During measurement, the hit information about the position and ToT is stored in the readout system's 2 MB onboard memory. After processing all trigger commands or when the memory is filled 99 %, the data is read out.
The so-called Trigger ID counter counts the number of given trigger commands and is set to zero when the data is read out. For a detailed introduction to the data storage of the readout system, see M. Backhaus *et al.* [79].
The Trigger IDs, together with a counter for the trigger pulses sent per trigger command and the corresponding event information, are written into an ASCII file, referred to as raw output file. The event information consists of the pixel position and the ToT value.
Due to the lateral diffusion of the charge cloud in the silicon sensor, a particle can deposit energy in more than one pixel. This process is called charge sharing [84, 85]. It requires post-processing of the data taken if tracking of individual particles is requested. Custom software is used to assign the correct hits to the corresponding particle entry. Simultaneous hits with timing deviations up to 3BCUs that occur in pixels with a variation of maximum ± 1 pixel in column and row direction are summarized into a cluster.
The cluster charge for every cluster is the sum of the single charges for all hits in a cluster. To account for slightly different tuning of the pixels in a cluster, the ToT calibration is performed before the clustering.
The hit position of the particles is determined as the ToT-weighted center of gravity of the clusters. If the clusters consist of a single hit, the center of the hit pixel is defined as the hit position. Clusters containing overflow hits or small hits are discarded.

Chapter

PBS spot shape and position measurements

5

Several approaches are examined in the proton therapy community with the aim to shape the high dose regions to the surface of the tumor volume. Thereby the normal tissue complication probability is reduced while improving the tumor control probability.

Among others, studies demonstrate that collimating pencil beam scanning proton fields leads to a decreasing lateral penumbra. [8, 86]

To give an example, C. Behrends *et al.* [10] showed a decreasing lateral penumbra of about 20 % for a single pencil beam spot in the air when using overscanning for collimated PBS fields.

Another approach to achieve a better normal tissue sparing in proton therapy is Minibeam radiation therapy (MBRT) [87]. Based on slit collimators with slit widths between 0.2 and 1 mm, spatially fractionated dose distributions can be applied during treatment. Promising results from various studies confirm better sparing of normal tissue [88, 89] and indicate higher tumor control probability [90, 91] when applying these inhomogeneous dose distributions. In addition to the advantages mentioned above, the necessary routine dosimetry for the minibeam dose distributions is challenging because detectors with spatial resolution in the range of micrometers are required to characterize the small beams [92].

A look at the above examples illustrates that the requirements of spatial resolution for detectors in proton therapy continue to increase as the development of various new approaches to therapy progresses [93]. The following chapter discusses measurement results that evaluate the performance of ATLAS IBL pixel detectors for the characterization of small proton fields. As pencil beam spots are the smallest

fields that one can get from the treatment machine at the WPE without using other apertures, we characterize them to demonstrate the high spatial resolution of the detector under study.
Detailed introduction about the requirements on QA for PBS fields and the quantities being studied are introduced section 2.3. They include the beam width σ, the spot position, and the deviation from symmetry.
The principles of the spot shape characterization results presented below has already been published in the article *Characterization of pixelated silicon detectors for daily quality assurance measurements in proton therapy* in Journal of Physics: Conference Series **2374**, 012178 (2022) [19].

5.1 Measurement settings

All measurements described in this chapter were performed at the WPE using a clinical pencil beam scanning (PBS) line equipped with a dedicated PBS nozzle. A detailed description of the treatment machine can be found in chapter 2. To evaluate the applicability of the detector under study for spot shape characterization, single pencil beam spots in the energy range of $(100 - 220)$ MeV were measured, covering approximately the full energy range that can be generated at the WPE. Due to the beam optics, the width sigma σ of the beam depends on the proton energy and varies from 3.1 mm for high energies to 5.5 mm for the lowest energy.
In addition to spot shape, measurements were also performed to examine shifts of the spot position with the ATLAS IBL pixel detector. Therefore, a 100 MeV pencil beam spot with a constant dose is scanned across the sensor area. Shifts in the order of 0.2 to 5.0 mm in the long pixel (column) direction and 0.1 to 0.6 mm the short pixel (row) direction were carried out.
The setup for the spot characterization measurements consists of an ATLAS IBL pixel detector aligned in the isocenter of the beam and a scintillation detector placed downstream, shown in Figure 5.1. After traversing through the silicon sensor, the majority of the protons hit the scintillation detector and induce a signal. The temporal correlation of the signals in both detectors is utilized by using the scintillator signal as an external trigger for the data read-out of the detector under study.

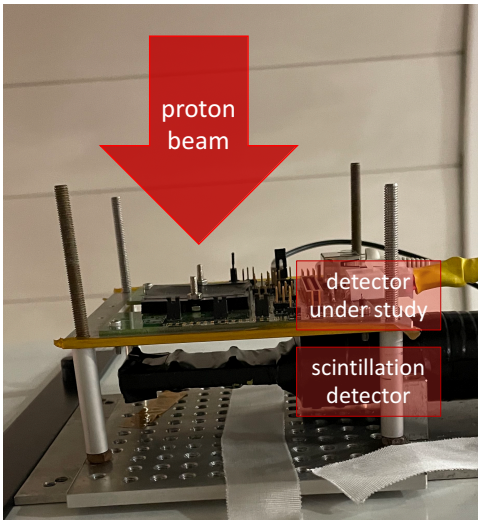

Figure 5.1: Picture of the measurement setup for the beam spot characterization at the WPE consisting of the ATLAS IBL pixel detector and the trigger scintillator downstream. The proton beam direction is highlighted.

In the case of this triggering method, the beginning and end of the data acquisition are related to the time of irradiation, and a manual operation is not necessary. This facilitates handling and conserves the memory of the readout system since no trigger signals are sent when no beam is switched on. A detailed introduction to the different triggering methods of the detector under study is provided in section 4.7. The tuning was selected to match the energy range during the experiment.

5.2 Spot shape characterization

The shape and position of the single pencil beam spots were examined by looking at the distribution of hits across the pixel array of the detector using a so-called hitmap. To extract the proton hit information, the measured entries have to be assigned to single protons; see the clustering introduction in section 4.8. For the hit position of clusters larger than a single pixel, we use the ToT-weighted center of gravity of the hit pixels.

As an example, the hitmap measured for a pencil beam with an energy of $E_{\text{sensor}} = 100\,\text{MeV}$ is shown in Figure 5.2. One can identify the expected Gaussian intensity profile of the single pencil beam spot, described in chapter 2.

To correct for the low statistics, pixel arrays of 10 rows x 2 columns are combined into one super-pixel with a resulting size of 0.5 mm × 0.5 mm, drawn in Figure 5.2. In addition, hits registered as overflow hits, see section 4.6, are also considered for spot shape characterization.
Further analysis of the spot intensity profile is performed by fitting a two-dimensional Gaussian distribution to the hitmap data, parameterized as

$$\begin{aligned} f(x,y) &= I \cdot \exp\left(-a \cdot (x-x_0)^2 - 2 \cdot b \cdot (x-x_0) \cdot (y-y_0) - c \cdot (y-y_0)^2\right) \\ &\text{with} \\ a &= \frac{\cos^2(\theta)}{2 \cdot \sigma_\mathrm{x}^2} + \frac{\sin^2(\theta)}{2 \cdot \sigma_\mathrm{y}^2} \\ b &= -\frac{\sin(2\theta)}{4 \cdot \sigma_\mathrm{x}^2} + \frac{\sin(2\theta)}{4 \cdot \sigma_\mathrm{y}^2} \\ c &= \frac{\sin^2(\theta)}{2 \cdot \sigma_\mathrm{x}^2} + \frac{\cos^2(\theta)}{2 \cdot \sigma_\mathrm{y}^2}. \end{aligned} \tag{5.1}$$

Here, I is the intensity, x_0 and y_0 are the means of the distribution, and θ is the rotation angle of the distribution measured counterclockwise. The standard deviations σ_x and σ_y describe the width of the distribution in column and row direction.
An evaluation of the goodness of fit is provided applying the reduced chi-squared χ^{2*} criterion, defined as

$$\chi^{2*}(\vec{p}) = \frac{1}{N-P} \sum_{i=1}^{N} \left[\frac{y_\mathrm{i} - g(x_\mathrm{i})}{\sigma_\mathrm{i}} \right]^2 . \tag{5.2}$$

In this case, the quality of fit depends on the degrees of freedom $(N-P)$ with a set of N measurements $\{(x_\mathrm{i}, y_\mathrm{i})\}$ and the Gaussian error on the measurement σ_i. In addition, the fitted distribution $g(\mathrm{x}, \vec{p})$, where $\vec{p}$ is a vector containing P independent fit parameters, has to be taken into account. A χ^{2*} value of 1 would represent a perfect fit, whereas values of $\chi^{2*} > 1$ and $\chi^{2*} < 1$ indicate a bad description of the data by the fit and an overfit, respectively. With χ^{2*} values in the range of $[0.88 - 1.60]$ the goodness of fit was proven. [94, 95]
Unless otherwise stated, all fits in this thesis are performed using the function *curve_fit* from *scipy.optimize* [96].
Figure 5.3 depicts hitmaps measured with different proton energies to illustrate the

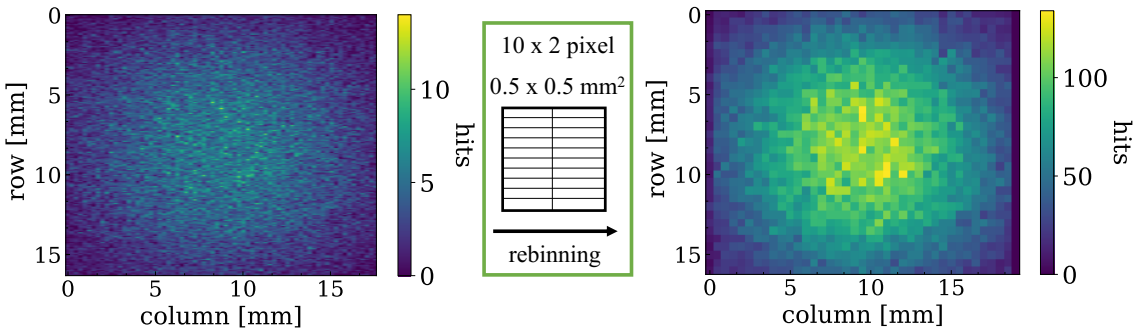

Figure 5.2: Hitmap showing the shape of pencil beam spots measured at $E_{\text{sensor}} = 100\,\text{MeV}$. In addition the rebinned hitmap with pixel sizes of $0.5\,\text{mm} \times 0.5\,\text{mm}$ is shown.

progression of the spot shape with the proton energy. The two-dimensional Gaussian fits are indicated by the orange σ bands and the standard deviations σ_{x} and σ_{y} highlighted in white.

The measurement results reveal a decrease in the spot size and a loss of roundness with increasing proton energy. In addition, the rotation angle θ varies between measurements. These findings now need to be discussed extensively.

First, the standard deviation of the beam in x- (a) and y-direction (b) as a function of proton energy is shown in Figure 5.4. The uncertainties on the measured widths $u(\sigma)$ are calculated during fitting by taking the uncertainties on every pixel entry into account. Based on Poisson distribution, the uncertainty for counting experiments like this is defined as the square root of the number of hits [62].

The precision of the pixel detector for those beam width measurements $u(\bar{\sigma}_{\text{x}})$ and $u(\bar{\sigma}_{\text{y}})$ is calculated as the mean $u(\sigma)$ over all measurements resulting in:

$$u(\bar{\sigma}_{\text{x}}) = 0.026\,\text{mm}$$
$$u(\bar{\sigma}_{\text{y}}) = 0.028\,\text{mm}.$$

Since the width of the investigated PBS spots is an order of magnitude larger than the pixel size of the detector, the rebinning of the results does not adversely affect the precision.

Due to the small pixel size, the spatial resolution of the pixelated semiconductor detectors like the ATLAS IBL detectors is an order of magnitude better than the commonly used Lynx PT detector (IBA Dosimetry, Schwarzenbruck, Germany) [97, 98]. Other semiconductor pixel detectors like the Timepix with a pixel pitch of

55 µm were also used successfully for proton field shape characterization [99, 100].

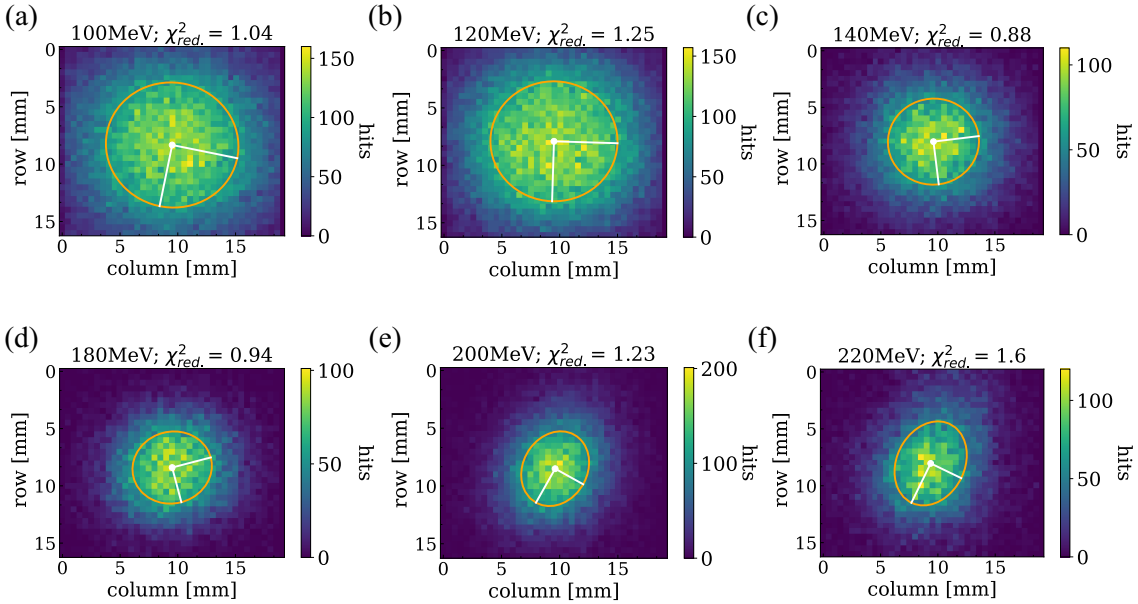

Figure 5.3: Hitmaps showing the shape of pencil beam spots measured in the energy range of $(100 - 220)$ MeV. The orange line highlights the $1 - \sigma$ band of the gaussian fit and the white lines illustrate the corresponding σ.

The expected trend of decreasing beam width with increasing proton energy is confirmed, considering the results shown in Figure 5.4. Furthermore, statistically significant deviations in the width of pencil beam spots measured with the same energy occur. The mean deviation between measurements performed for one energy is 6.8 %, whereas the expected repeatability of the machine modeling the spot shape is approximately 5 % [39]. For comparison Mirandola *et. al*, published the dosimetric commissioning results of scanned ion beams at the Italian National Center for Oncological Hadrontherapy with an overall mean spot size variation of approximately 4.1 % taken in a period of one year [101].

When comparing the energy-dependent spot width variation in x- (Figure 5.4(a)) and y- (Figure 5.4(a)) direction, one notices the differences for proton energies exceeding 200 MeV: the σ_x decreases, while the σ_y increases towards higher proton energies.

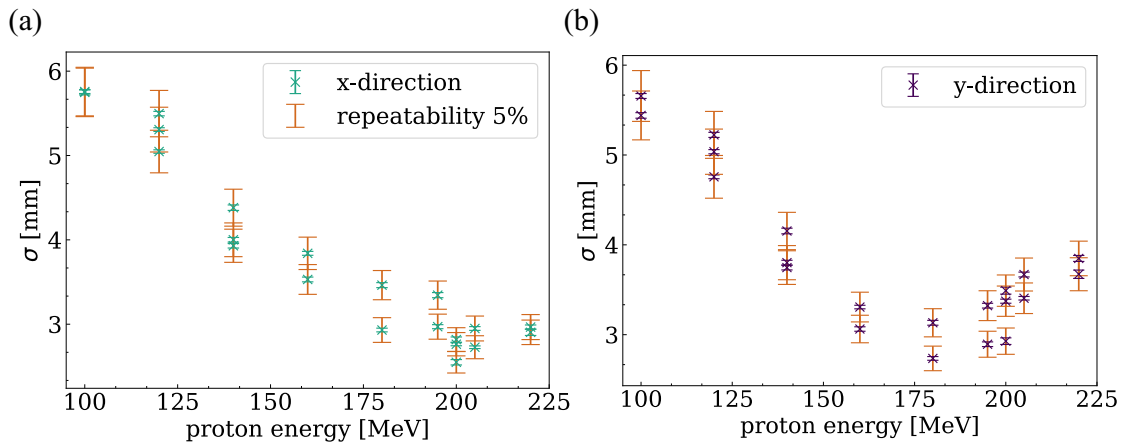

Figure 5.4: Pencil beam spot σ in x- (a) and y-direction (b) as a function of the proton energy. The 5 % repeatability of the treatment machine is highlighted as additional error bands.

This indicates that the spots become asymmetric with higher proton energies. To investigate the latter the relative percentage asymmetry as is defined as

$$as = 100 \cdot \left(1 - \frac{\sigma_{\mathrm{x}}}{\sigma_{\mathrm{y}}}\right) \tag{5.3}$$

and illustrated as a function of the proton energies in Figure 5.5. The expected asymmetry of the used treatment machine is smaller than $\approx 10\,\%$ [39], which in our measurements can be satisfied only by spots for beam energies smaller than 200 MeV. Moreover, the deviation from the commissioning beam width [39] $\sigma_{\mathrm{com.}}$ increases for higher energy spots on view in Figure 5.6. The plot illustrates the mean spot width $\bar{\sigma}$ compared to the commissioning data and the corresponding relative deviation for all investigated proton energies. A mean deviation from the commissioning data of 5.0 % for all energies and of 4.6 % when limiting the proton energy to be < 200 MeV indicates a shape shift for high energy spots compared to the commissioning data. The gained results confirm previous spot characterization measurements at the WPE based on which the energy range during treatment was limited up to 200 MeV. The increasing asymmetry and deviation from commissioning rule the usage of higher energy beams out because it may impact the dose distribution during patient treatment.

In conclusion, the ATLAS IBL pixel detector has been successfully used to characterize

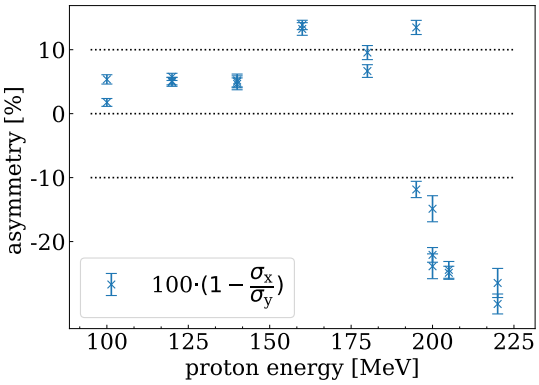

Figure 5.5: Asymmetry of pencil beam spot depending on the proton energy.

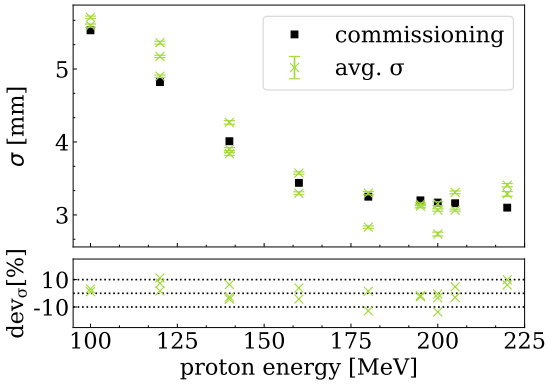

Figure 5.6: Mean pencil beam spot σ as a function of the proton energy. The deviation from the commissioning data is shown in the lower part of the plots.

beam profiles. The measured increasing asymmetry of the beam spots with increasing proton energy confirms the daily QA measurements performed at the West German Proton Therapy Centre Essen (WPE).

5.3 Spot position characterization

In addition to spot shape characterization, the spot position has to be investigated for quality assurance, too. Due to the high spatial resolution of the pixelated detector, it is well suited for spot position determination, which is demonstrated through exemplary measurements summarized in this section. Detailed introduction about the requirements on quality assurance for PBS fields are given in section 2.3.
To investigate the applicability of the detector for beam spot position measurements, a 100 MeV proton spot is shifted to relative positions on the detector area starting at a start position, namely point zero. The position of point zero on the detector area $(p_{0,\mathrm{col}}, p_{0,\mathrm{row}})$ is calculated as the average of all positions measured during the

spot shape characterization, when the detector is shifted in the perpendicular pixel direction:

$$p_{0,\mathrm{col}} = (9.611 \pm 0.027)\,\mathrm{mm}$$
$$p_{0,\mathrm{row}} = (8.118 \pm 0.035)\,\mathrm{mm}.$$

The standard deviations of point zero of 0.067 mm in column direction and 0.112 mm in row direction are an estimator for the precision on point zero determination taking into consideration the repeatability of the treatment machine and the spatial resolution of the detector.

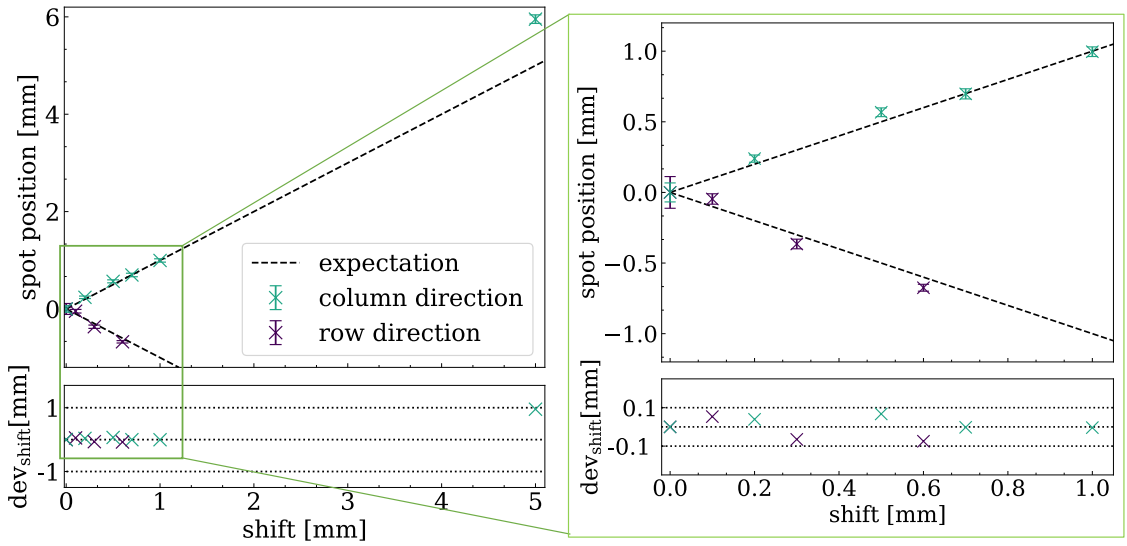

Figure 5.7: Average spot position in row and column direction as a function of the true shift. In order to assess the results more precisely the area of set positions up to 1 mm is zoomed in. The lower part of the plot highlights the deviation of true shift and measured spot position.

Figure 5.7 shows the averaged measured spot shifts in column and row direction depending on the known shifts relative to point zero. Apart from the shift of 5 mm in column direction, the averaged spot positions agree with the set position with a maximum deviation of $\mathrm{dev}_{\mathrm{shift}} = 0.075\,\mathrm{mm}$. The outlier is due to the fact that the position of this spot is only ≈ 10 pixels away from the detector edge. The resulting distortion of the intensity profile introduces a bias on the measured spot position. Consequently, the accuracy of the spot position determination $u(p_{\mathrm{col}})$ and $u(p_{\mathrm{row}})$

using the ATLAS IBL pixel detector is determined as the mean deviation between the true shift and the measured spot position:

$$u(p_{\mathrm{col}}) = 0.023\,\mathrm{mm}$$
$$u(p_{\mathrm{row}}) = 0.027\,\mathrm{mm}.$$

Considering the recommendation for quality assurance introduced in section 2.3, it has to be mentioned that the precision of spot position determination exceeds the proposed spot position tolerances ($\approx 0.7\,\mathrm{mm}$) by an order of magnitude [38].

Chapter 6

Dose consistency measurements

The readout chip (FE) of the detector under study is developed for particle tracking in HEP experiments like the ATLAS experiment [18]. Therefore, one demanding requirement is the correct hit detection within one bunch crossing cycle and around 25 ns, respectively [102]. At occupancies of 400 $\frac{\text{MHz}}{\text{cm}^2}$ ($\approx$ 3 $\frac{\text{hits}}{25\,\text{ns}\cdot\text{FE}}$), a hit inefficiency below 1 % is achieved [103].
In contrast, beam currents around 2 nA ($\approx 1.2 \cdot 10^{10}$ $\frac{\text{protons}}{\text{s}}$) at the nozzle's exit are commonly used in proton therapy treatments. In other words, a particle bunch every 9.4 ns comprises approximately 100 protons. [11]
This chapter addresses whether the detector under study can be used for dose measurements in proton therapy applications despite the high beam currents. We will distinguish between absolute and relative dose measurements.
One way to determine the absolute dose is fluence-based measurements, where the dose can be derived from the product of fluence and stopping power [45]. In comparison, relative dose measurements assume no particle counting, but the linear correlation between the quantity to measure and the dose has to be proven. Therefore, the dose linearity for varying irradiation duration and beam currents was investigated. Based on the gained results, features of the readout chip impacting the particle tracking are discussed to evaluate the device's applicability under study for dose measurements.

6.1 Dose linearity in PBS mode

As part of the daily QA in proton therapy, an output dose constancy of ± 3 % has to be verified [38]. The applicability of the investigated detector for checking dose

constancy during daily QA is tested by characterizing the dose-dependent response of the detector.
The corresponding measurements were performed at the WPE using $2.5 \times 2.5\,\mathrm{cm}^2$ PBS proton fields with energies of approximately 100 MeV. A proton field is made up of 121 single pencil beam spots. The dose is varied in the range of $(150-220)$ monitor units (MU), which is a facility-specified unit. Per dose, the measurement is repeated at least two times. For the utilized treatment machine, the reproducibility of the delivered point dose was approximated at $0.3\,\% - 0.5\,\%$ based on the measurements presented by C. Bäumer *et al.* [104].
The ATLAS IBL Pixel detector comprises a silicon sensor with 200 µm thickness and the FE-I4B readout chip. A 1 kHz fixed frequency trigger signal controls the data acquisition. In other words, a trigger command is sent every millisecond. As described in section 4.8, the hits in the sensor generated by an individual proton are assigned to a cluster. A first analysis of the dose linearity of the detector based on these measurements is published in the article *Characterization of pixelated silicon detectors for daily quality assurance measurements in proton therapy* in Journal of Physics: Conference Series **2374**, 012178 (2022) [19]. However, the subsequent evaluation will go into more detail.
For clarification, the following quantities are used to analyze the results:

- d_{trigger}: number of clusters detected for one trigger command,
- $t_{\mathrm{treat.}}$: irradiation duration defined as number of trigger commands in between the one where d_{trigger} first exceeds 12 clusters and as last fall below 12 clusters,
- d: sum of clusters measured during $t_{\mathrm{treat.}}$,
- $\bar{d}_{\mathrm{treat.}}$: averaged number of clusters per trigger command d_{trigger} measured during $t_{\mathrm{treat.}}$.

The threshold of 12 clusters per trigger command to define the treatment duration is chosen because it corresponds to the maximum d_{trigger} measured when no irradiation occurs.
A demonstration of the temporal distribution of d_{trigger} throughout irradiation is shown in Figure 6.1. Two exemplary measurements for irradiation with a dose of 150 MU and a dose of 220 MU were selected for comparison.
It can be noted as a qualitative description that the shape of the distribution is

similar. During the irradiation with the PBS technique, pencil beam spots are emitted one by one at various places over the detector. Most clusters are measured for the spots that hit the detector in the middle. The temporal structure of PBS fields measured with the detector under study is examined in more detail in section 8.3.

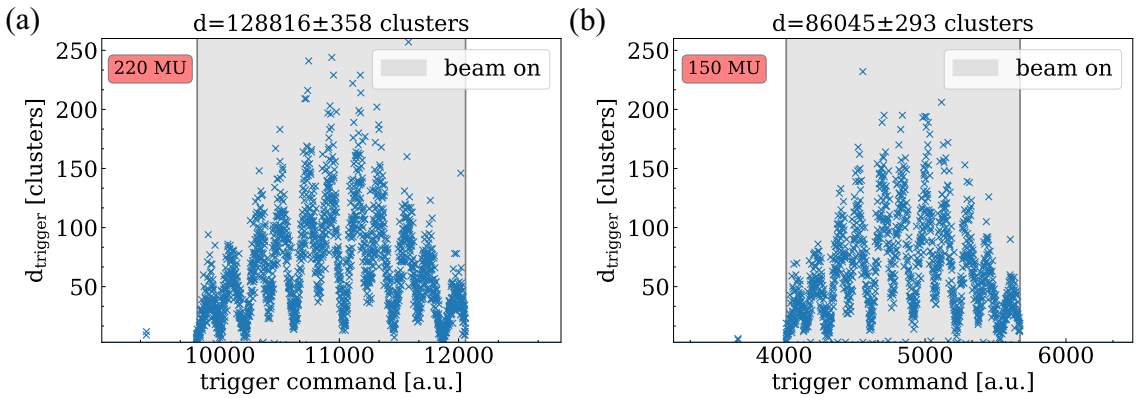

Figure 6.1: Temporal distribution of clusters over irradiation duration for an applied dose of 150 MU(a) and 220 MU(b). The estimated irradiation duration $t_{\text{treat.}}$ is highlighted in grey.

Now, we are turning to a quantitative investigation of the clusters measured while the beam was on. Since the proton energy remains unchanged during this study, a higher dose implies a longer duration of irradiation or an increased beam current. For the chosen beam parameters, the increase in beam current is small compared to the increase in irradiation duration. Investigations of $\bar{d}_{\text{treat.}}$ for all measurements of this study result in an average $\bar{d}_{\text{treat.}}$ which is 65.1 $\frac{\text{clusters}}{\text{trigger command}}$. A standard deviation of 0.7 $\frac{\text{clusters}}{\text{trigger command}}$ confirms the assumption of small variations in the beam current for different dose settings. In contrast, the measured duration of the irradiation increases with increasing dose, highlighted gray in Figure 6.1 as an example. The average duration measured for the lowest dose $t_{\text{treat,150MU}} = (1652 \pm 7)$ trigger commands, whereas the average duration measured for the highest dose is determined to be $t_{\text{treat,220MU}} = (2255 \pm 6)$ trigger commands with uncertainty given by the standard deviation of the two measurements performed per dose setting.

Considering these results, the total number of clusters d has to be proportional to the set dose of the proton field. Figure 6.2 presents the averaged total number of clusters over the full detector area d_{mean} as a function of the dose in facility-specific units MU. A linear regression (gradient $a = (602 \pm 6)\,\frac{\text{clusters}}{\text{MU}}$, interception

$b = (-4100 \pm 900)$ clusters) is used to describe the data. The 3 % band is highlighted in Figure 6.2 because an output dose constancy of $\pm 3\,\%$ has to be verified during daily QA in proton therapy [38].
A measure for the precision of the dose determination was estimated by considering the relative deviation $\mathrm{dev}_{\mathrm{dose}}$ of measurements performed for the same dose $(d_{\mathrm{i}} - d_{\mathrm{j}})$:

$$\mathrm{dev.}_{\mathrm{dose}} = \frac{d_{\mathrm{i}} - d_{\mathrm{j}}}{d_{\mathrm{mean}}} \cdot 100. \tag{6.1}$$

As the bottom plot of Figure 6.2 indicates, all measurements except one have a deviation of less than 3 %. Using PBS fields for dose linearity characterizations potentially adds some extra uncertainties. Nevertheless, the mean relative deviation is 1.5 %. Therefore, we conclude that the detector meets the requirements for dose consistency checks during daily QA.

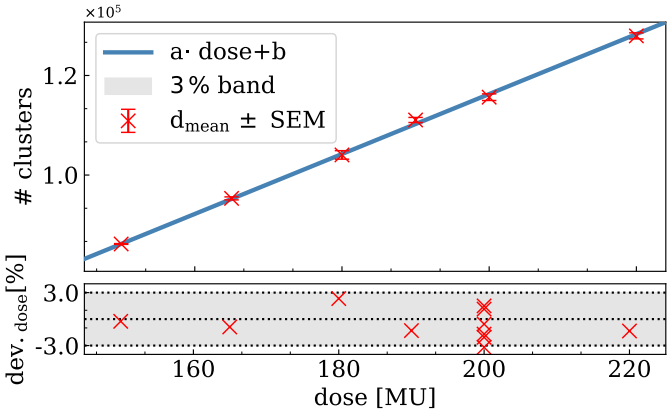

Figure 6.2: Averaged total number of clusters d_{mean} as a function of the dose described by facility-specific monitor units (MU). The linear regression (gradient $a = (602 \pm 6)\,\frac{\mathrm{clusters}}{\mathrm{MU}}$, interception $b = (-4100 \pm 900)$ clusters) is highlighted in blue. The gray band indicates the 3 % region as QA requirement. The relative deviation between measurements performed for the same dose is shown in the bottom plot.

6.2 Dose linearity measured for varying beam currents

During the last section, we proved the proportionality of the number of measured clusters with the dose when mainly varying the irradiation duration. Dose consistency checks with the detector under study can be performed using this correlation. In addition, dose variations can also be induced by changing the beam current and leaving proton energy and duration of the irradiation unchanged.
Therefore the following study focuses on investigations of the performance of the detector under study for tracking individual protons at different beam currents.

6.2.1 Experimental Setup

The following studies were performed in the experimental room of the OncoRay in Dresden. The University Proton Therapy Dresden (UPTD) utilizes the *Proteus 235 Proton Therapy System*, just like the WPE. The treatment system was already introduced in section 2.2.
The experimental room is equipped with a horizontally fixed beam line. During this study, the ATLAS IBL Pixel detector was aligned in front of the exit window of the beam line. PMMA plates with a total WET of 70.7 mm were placed upstream to generate a homogeneous proton field larger than the detector under study. The proton energy was set to 220 MeV on the treatment machine controlling system. Considering the PMMA plates in front of the detector, the protons impinging the sensor had a mean energy of approximately 188 MeV. By using a PMMA cylinder with a thickness of 20 cm and a hole diameter of 50 mm, the electronics of the PCB board are shielded.
During the measurement, the beam current I_{beam} was varied in the range of 0.35 nA – 20 nA for irradiation duration times of 1 s. Notice that the beam current settings adjusted at the controlling system are only used as labels in this study because the precise beam current at the position of the detector under study is unknown.
The detector was operated with a fixed frequency trigger to get a constant time between trigger pulses.

6.2.2 Impact of sensitive time per trigger

The quantity we are interested in during this study is the number of protons measured in a defined time interval. Different triggering settings of the readout chip must be taken into account when investigating the latter, starting with the frequency of the external trigger signal. Unless otherwise stated, the frequency of the external trigger signal is set to 1 kHz. Hence, the time between two trigger commands is 1 ms. By choosing the number of trigger commands sent, the measurement duration is adjusted to 100.000 trigger commands unless provided otherwise. During this study, all trigger commands between the one where d_{trigger} first exceeds 3 clusters and at last fall below 3 clusters are assigned to the irradiation duration $t_{\text{treat.}}$. The utilized threshold of 3 clusters is chosen because it corresponds to the maximum d_{trigger} measured when no irradiation occurred. It is different for various sensors because the threshold depends on the tuning and the electronic noise.
The number of trigger pulses sent per trigger command is defined by adjusting the TrigCnt settings, as introduced in section 4.7. It can be 1 to 16 spaced by one clock (25 ns) and thereby set the sensitive time of the detector per trigger command from $1 \cdot 25\,\text{ns}$ to $16 \cdot 25\,\text{ns}$ [1]. Taking the TrigCnt settings into account, the number of clusters measured per trigger pulse R_{TrigCnt} can be determined:

$$R_{\text{TrigCnt}} = \frac{\bar{d}_{\text{treat.}}}{\text{TrigCnt}} \ \text{[clusters/BCU]}. \tag{6.2}$$

To illustrate the quantities to measure, two exemplary measurements will be discussed taken for the same treatment machine settings ($I_{\text{beam}} = 0.35\,\text{nA}$) but with a different TrigCnt parameter set. The distributions of d_{trigger} are shown in Figure 6.3. In contrast to the distribution of clusters presented in Figure 6.1 measured for a PBS field, an apparently normally distributed number of clusters was measured during $t_{\text{treat.}}$ (highlighted grey) in this case. We expected this since only one field was used, which was centered on the detector.
By comparing the number of clusters measured for the different TrigCnt settings shown in Figure 6.3, the decrease in clusters measured with the smaller TrigCnt is evident. Due to the shorter sensitive time of the detector, fewer clusters are counted. Even so, the number of clusters measured per trigger pulse R_{TrigCnt} agrees for both measurements taking into account the uncertainties (SEM).

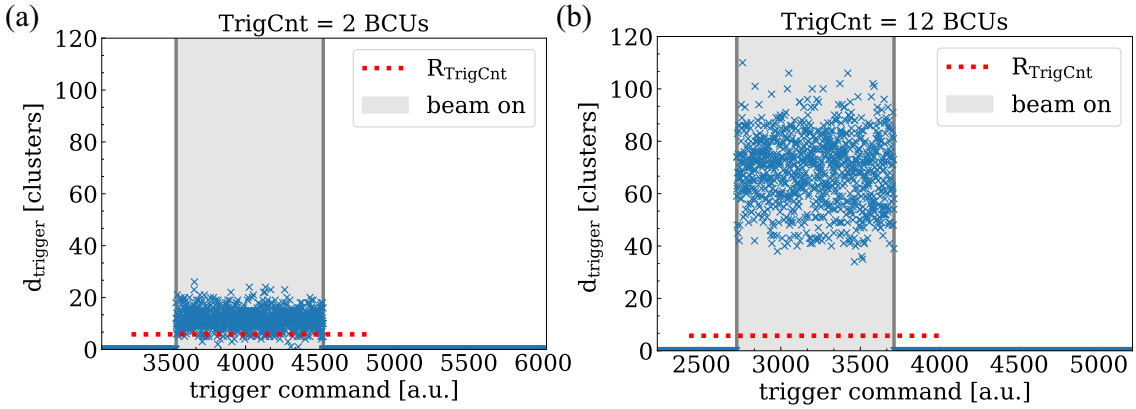

Figure 6.3: Temporal distribution of clusters over irradiation with the same treatment machine settings ($I_{\text{beam}} = 0.35\,\text{nA}$), but with different TrigCnt parameters: 2 BCUs(a) and 12 BCUs(b). The irradiation duration is highlighted in grey. Since the beam current is unchanged the averaged number of clusters per BCU R_{TrigCnt} agrees (red dotted line).

This observation is confirmed by repeating the measurement with other TrigCnt settings. The corresponding results are listed in Table 6.1. Considering the variation of the dose during the measurement campaign given by the monitoring system of 1.4 %, we conclude that the number of measured clusters per trigger pulse R_{TrigCnt} is constant regardless of the TrigCnt setting. The average number of clusters measured per trigger pulse when irradiating the detector with $I_{\text{beam}} = 0.35\,\text{nA}$ is determined to be $\bar{R}_{\text{TrigCnt},0.35\text{nA}} = (5.65 \pm 0.04)$ clusters/BCU.

Table 6.1: The investigated TrigCnt settings and the corresponding average number of clusters per BCU. The uncertainty on the results is given by the SEM.

TrigCnt [BCUs]	R_{TrigCnt} [clusters/BCU]
1	5.70 ± 0.10
2	5.80 ± 0.05
8	5.70 ± 0.04
10	5.57 ± 0.03
12	5.65 ± 0.04
16	5.73 ± 0.03

The measured irradiation duration $t_{\text{treat.}}$ for all measurements with $I_{\text{beam}} = 0.35\,\text{nA}$ was in the range of 989 to 991 trigger commands for a set irradiation duration of 1 s. This result corresponds to an underestimation of the irradiation duration of $\approx 0.01\,\text{s}$ concerning the trigger frequency of 1 kHz.

6.2.3 Investigation of memory consumption

During our studies, we have seen detector settings for which we underestimated the expected irradiation duration by more than $\approx 0.01\,\text{s}$. The reason for this and the impact on the applicability of the detector under study for proton beam characterization will be discussed in this section. In order to do this, the data storage process of the detector under study is considered, introduced in section 4.5. During a measurement, the hit information on the position and ToT are stored on the readout system until the memory is filled to 99 %. Then the data is read out, and the Trigger ID counter is set to zero.
To state the impact of the data readout, two exemplary measurements were performed for the same treatment machine settings ($I_{\text{beam}} = 0.8\,\text{nA}$) but with different TrigCnt parameters. The resulting cluster distributions over irradiation duration are shown in Figure 6.4: 10 BCUs(a) and 6 BCUs(b). The irradiation duration is highlighted in grey, and the stored Trigger IDs are marked in red.
By comparing both plots, we notice that the increased number of clusters per trigger command when sending 10 trigger pulses per trigger command leads to increased memory consumption. In addition, the information of every sent trigger command and trigger pulse is stored and read out. Thus, the memory is already partially filled even without the proton beam being switched on. As a result of the earlier data readout, the Trigger ID counter is set to zero. In contrast, the measurement with 6 trigger pulses per trigger command features no data read out from the readout system during irradiation.
The comparison of the measured irradiation duration $t_{\text{treat.}}$ reveals 883 trigger commands for the measurement with 10 trigger pulses per trigger command and 990 trigger commands for the measurement with the 6 trigger pulses per trigger command. The latter underestimates the set irradiation duration of 1 s slightly, consistent with the previously described measurements. In conclusion, emptying the

readout system's memory leads to an underestimation of $t_{\text{treat.}}$ exceeding 0.1 s. This is due to the reduction of sensitive time of the detector and loss of proton hits during the emptying of the readout board's memory.

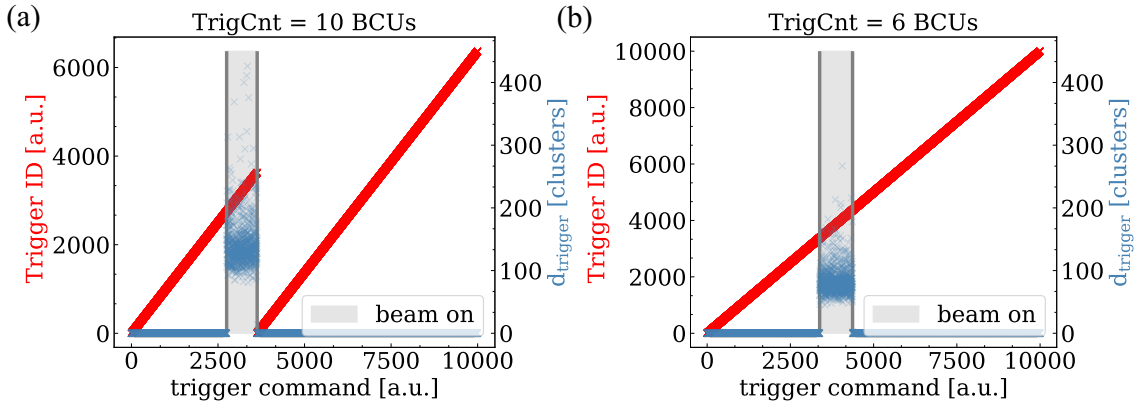

Figure 6.4: Distribution of clusters over irradiation with the same treatment machine settings ($I_{\text{beam}} = 0.8\,\text{nA}$), but with different TrigCnt parameters: 10 BCUs(a) and 6 BCUs(b). The irradiation duration is highlighted in grey and the stored Trigger IDs are marked in red.

If the quantity of interest is the mean number of clusters measured per clock (BCU), the loss of protons does not affect the measurement. Only the statistic of counted clusters is reduced. But when turning to the characterization of the shape of scanned PBS fields, for example, the number of pulses per trigger command and the trigger frequency have to be adjusted according to the irradiation duration. The requirement is that all beam spots can be detected before the memory of the readout system has to be emptied. One solution to this is to use a scintillation detector downstream of the detector as a trigger generator to correlate the trigger signals with the incidence of the proton beam.

In addition, we have to notice that absolute dose measurements with the device under study are not feasible, taking into account the status of this thesis as the insensitive time during memory readout is not well known.

6.2.4 Dose linearity

Based on the awareness that the number of measured clusters $\bar{d}_{\text{treat.}}$ is proportional to the number of trigger pulses sent per trigger command, we are interested in investigating the proportionality of R_{TrigCnt} to the beam current I_{beam} now. Hence, R_{TrigCnt} is measured for various beam currents and TrigCnt settings. Since the beam current labels set at the treatment machine may deviate from the expectation for low currents, the dose measured with the integrated ionization chambers in the nozzle is considered for the dose linearity investigations. The dose is provided in the facility-specific unit MU and varies slightly for unchanged beam parameters due to deviations of the treatment machine. In this study, we use the average dose values given for the same machine settings. The uncertainties are provided by the SEM. The maximum percentage uncertainty of the complete measurement campaign is used as a conservative uncertainty estimation for dose values that were irradiated only once. The resulting dose values and detailed measurement settings are listed in Table 6.2. In addition, this table contains the averaged clusters per BCU $\bar{R}_{\text{TrigCnt}}$. Accordingly, Figure 6.5 illustrates the averaged number of clusters per BCU as a function of the dose for a fixed irradiation time of 1 s.

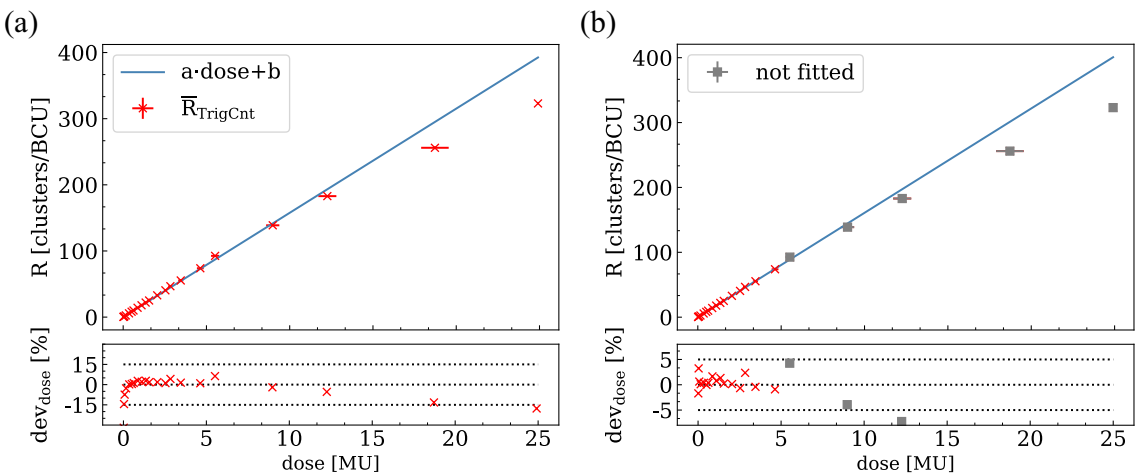

Figure 6.5: Averaged clusters per BCU $\bar{R}_{\text{TrigCnt}}$ measured for various proton beam currents I_{beam} and dose per 1 s, respectively. The deviation dev$_{\text{dose}}$ from the fit that describes the data (blue line) is shown in the bottom plot. Some data points were excluded from analysis (grey squares), illustrated in (b).

Table 6.2: Settings of I_{beam} and corresponding dose values measured with the integrated ionization chamber at the nozzle's exit for a fixed irradiation time of 1 s. The TrigCnt parameters and measured clusters per BCU $\bar{R}_{\text{TrigCnt}}$ are listed.

I_{beam} [nA]	0.030	0.045	0.088	0.175	0.350	0.500	0.600
TrigCnt [BCUs]	2x12	12	12	2x12	1, 2 1x10 5x12 8, 16	2x10	10
dose [MUs]	0.016 ± 0.001	0.034 ± 0.002	0.073 ± 0.003	0.158 ± 0.007	0.351 ± 0.002	0.506 ± 0.001	0.620 ± 0.028
$\bar{R}_{\text{TrigCnt}}$ [clusters/BCU]	0.27 ± 0.01	0.58 ± 0.02	1.20 ± 0.02	2.56 ± 0.01	5.65 ± 0.04	8.16 ± 0.00	10.03 ± 0.04

I_{beam} [nA]	0.8	1.0	1.2	1.4	1.8	2.2	2.5
TrigCnt [BCUs]	10, 8	6	4, 6	4	4	4	1
dose [MUs]	0.864 ± 0.001	1.102 ± 0.049	1.349 ± 0.005	1.557 ± 0.069	2.043 ± 0.090	2.535 ± 0.011	2.835 ± 0.125
$\bar{R}_{\text{TrigCnt}}$ [clusters/BCU]	14.15 ± 0.06	17.88 ± 0.10	22.01 ± 0.17	25.13 ± 0.20	32.93 ± 0.30	40.53 ± 0.23	46.70 ± 0.70

I_{beam} [nA]	3.0	4.0	5.0	7.5	10.0	15.0	20.0
TrigCnt [BCUs]	1	2x1	1	1	1	1	2x1
dose [MUs]	3.457 ± 0.153	4.632 ± 0.205	5.520 ± 0.244	8.981 ± 0.397	12.260 ± 0.542	18.720 ± 0.827	24.910 ± 0.007
$\bar{R}_{\text{TrigCnt}}$ [clusters/BCU]	55.40 ± 0.60	73.85 ± 0.67	92.60 ± 0.90	138.80 ± 1.20	182.90 ± 1.70	256.00 ± 2.20	323.05 ± 1.10

Assuming a linear dependency between the applied dose and the averaged clusters per BCU $\bar{R}_{\text{TrigCnt}}$, we fit a linear function to the data. The deviation of the results from the linear fit dev_{dose} shown in the bottom plot of Figure 6.5(a) indicates an

inadequate presentation of the measured correlation by the linear fit.
Turing to a higher beam current the number of counted clusters seems to saturate weakly. To estimate the beam current until a linear dependency to the number of clusters is detectable, the fitting of the linear function is repeated by successively ejecting one data point for high beam currents after the other. The fit with a small χ^{2*} presented in Figure 6.5(b) gives an impression of which data is describable by a linear function properly. When fitting $\bar{R}_{\text{TrigCnt}}$ up to beam currents of 4 nA χ^{2*} is calculated to be 2.02.
Based on this, as a proof-of-principle we are able to demonstrate the proportionality of $\bar{R}_{\text{TrigCnt}}$ with beam current labels up to 4 nA with a mean relative deviation $\bar{\text{dev}}_{\text{I}} = 0.94\,\%$ from the fitted linear function (gradient $a = (16.09 \pm 0.01)\,\frac{\text{clusters}}{25\,\text{ns}\cdot\text{nA}}$, interception $b = (0.02 \pm 0.01)\,\frac{\text{clusters}}{25\,\text{ns}}$).
The number of measured clusters per BCU for beam current labels of 5 nA, 10 nA, 15 nA and 20 nA feature deviations $\bar{\text{dev}}_{\text{dose}} > 4\,\%$. That leads to the assumption that many proton hits have not been counted. An extended storage capacity on the readout chip, a higher frequency clock of the readout chip, improved data readout, or smaller detector pixels are possible solutions to face this.
Considering the obtained results, we have to conclude that the number of protons that can be detected per clock (25 ns) saturates for high beam currents. Since the beam currents given here are only labels and the beam current on the detector is not known, the maximum number of clusters that can be measured per 25 ns absent saturation is conservatively stated to be $\bar{R}_{\text{TrigCnt}}$ taken for $I_{\text{beam}} = 4\,\text{nA}$. The result is $\bar{R}_{\text{TrigCnt, max.}} = (73.85 \pm 0.95)\,\frac{\text{clusters}}{25\,\text{ns}}$. This recommendation is valid for irradiating with a single proton field and a measurement with a trigger frequency of 1 kHz. The applicability of the detector under study for dose consistency checks in the proposed range of clusters measured per one clock 25 nA could be confirmed.
For absolute dose measurements, additional investigations on the exact sensitive time, dead time of the detector, and the applicability to measure the deposited energy per proton have to be performed. The latter will be discussed in the following section.

Chapter

Energy deposition measurements

7

In proton therapy, multiple applications can take advantage of the features of hybrid pixelated semiconductor detectors. Some features to mention are the high spatial resolution and the single particle tracking with high efficiency discussed during the previous sections of this thesis. Besides this, the detector under study provides information on the deposited charge of the individual particles in the sensor, which is commonly used as part of the particle identification in the ATLAS experiment [105]; see chapter 4.

In addition, using the deposited charge, one can potentially determine the proton range and energy in proton therapy applications. Thus, the detector could be used for daily QA applications with the advantage of determining all required quantities with one device, such as spot size, dose linearity, and range of the protons [19].

Other groups have already successfully demonstrated the usage of particle-counting hybrid silicon detectors like the MiniPix-Timepix to determine clinically relevant proton energy through measured LET spectra. [100, 106].

Based on this, the aim is to test if the detector under study designed for efficient particle tracking in a high radiation-exposed environment can measure proton energies and ranges, respectively. For this purpose, the deposited energy distributions of the protons are considered. The results are compared to the requirements for the range verification of daily QA. In addition, potential outlines for further detector development are defined.

Two different methods to measure the proton energy have been developed, namely the *LET spectra measurements* and the *track LET measurements*.

Commonly used detectors like the Multi-Layer Ionization Chamber (MLIC) Giraffe

detector (IBA Dosimetry, Schwarzenbruck, Germany) measure the depth dose distribution of the protons to determine the proton range [47]. In contrast, we consider the energy deposition spectra in the detector under study, referred to as *LET spectra measurements*. By doing so, the proton energy is concluded.
The second measurement method was inspired by previous studies that impressively demonstrated estimations of the energy loss of particles by tracking them along their trajectory through the sensor. Hybrid pixelated semiconductor detectors like Timepix or Medipix have been used for this [77, 107, 108]. To reproduce these measurements, the ATLAS IBL pixel detector is aligned parallel to the beam axis to track individual protons and their corresponding energy deposition per pixel, referred to as *track LET measurements*. The incident proton energy was estimated by analyzing the energy deposition along the tracks.
The principle part of the results presented below has already been published in the article *Measuring the Beam Energy in Proton Therapy Facilities Using ATLAS IBL Pixel Detectors* in Instruments **6**, 80 (2022) [20]. Due to some minor improvements applied to the algorithm, the results presented below differ slightly from the published ones, although the general message of the article remains unchanged.

7.1 Measurement settings

All experiments discussed in this section were performed at the WPE using a clinical PBS line equipped with a dedicated PBS nozzle. A detailed description of the treatment facility can be found in chapter 2. Scanned homogeneous fields which completely covered the detector in the isocenter of the treatment machine were taken. Due to the high particle fluxes in proton therapy (up to $10^{10}\,\mathrm{cm}^{-2}\,\mathrm{s}^{-1}$ [109]), external trigger signals at a fixed frequency of 1 kHz were issued to control the data acquisition of the detector. In doing so, a compromise between the maximum sampling rate and memory consumption of the readout system was found. In addition, the smallest sensitive window per trigger of 1 BCU or 25 ns, respectively, was chosen by setting the TrigCnt parameter to one. Accordingly, one trigger pulse is sent per trigger command. These trigger settings intend to minimize memory consumption.
The tuning settings of the readout chips have to be adapted to the expected deposited energy of the protons; see section 4.5. Since protons in the therapeutic energy

range deposit considerably more energy in the silicon sensor than particles typically detected in HEP, the readout chips were tuned up to the maximum processable charge that they are designed for. To show the influence of the sensor thickness on the measurement of the deposited energy, sensors of 200 µm and 100 µm have been utilized.

7.2 Beam characteristics

Looking at the energy deposition of protons in the matter, one quickly recognizes the significant gradient towards small energies, see Figure 2.1. Therefore, small proton energies require less precision to be told apart than large ones when considering the energies deposited in the material.
Since the proton energy range delivered by the IBA Proteus 235 isochronous cyclotron is limited to $(100 - 228)$ MeV, the lowest possible energy is used during this measurement campaign [13]. Previous studies at the WPE demonstrated range measurements for a nominal beam energy of 100 MeV, resulting in proton energies between 99.7 MeV and 100.5 MeV. The determined energy range also considers deviations of the tables utilized to convert the measured into proton energy. [110]
Based on these findings, we expect the delivered proton energy to correspond to the center of the presented energy interval, which is (99.91 ± 0.40) MeV. Moreover, the variation of the proton energy is specified by Bäumer *et al.* [110] to be 0.65 MeV.
Turning to the beam model used at the WPE, the beam divergence for the chosen beam energy is around 0.3 °.
To further reduce the proton energy, various range shifters and RW3 slabs (type SP34 IBA Dosimetry, composition: 98 % polystyrene + 2 % TiO_2, water-equivalent ratio WER = 1.025) of different thicknesses were placed downstream of the nozzle. In some instances, custom-made Ploy(Methyl Methacrylate)(PMMA) staircase phantoms were mounted on the detector as well, first described in section 7.6.
Throughout the following section, various stages of proton energies will be mentioned. Accordingly, Figure 7.1 clarifies the definitions:

- E_{init}: initial proton energy delivered by the treatment machine;

- E_{phantom}: proton energy downstream of the RW3 slabs;
- E_{sensor}: energy of protons impinging on the sensor.

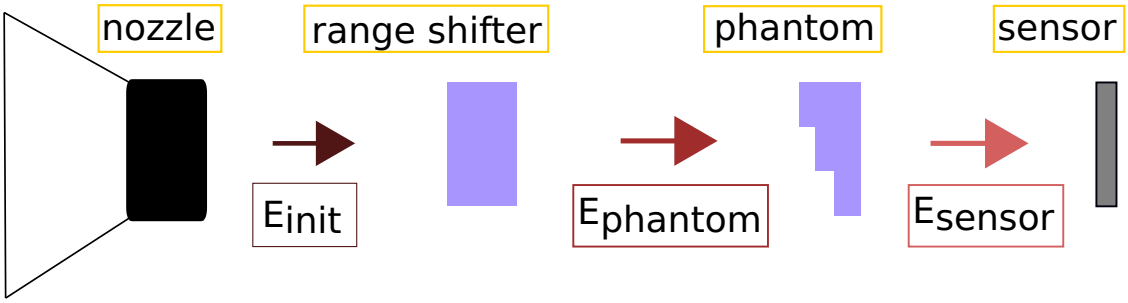

Figure 7.1: Illustration of the different proton energy stages that occur during measurement: the proton energy delivered by the accelerator E_{init}; the proton energy behind RW3 slabs of different thicknesses E_{phantom}; the energy of the protons impinging the silicon sensor E_{sensor}. [20]

To validate the measured deposited energy in the sensor $dE_{\text{SI,200}}$, the proton energy when impinging the detector E_{sensor} and the corresponding expected energy deposition $dE_{\text{expected,SI}}$ in silicon have to be determined. In order to do so, we subtracted the energy deposition in the RW3 slabs and the staircase phantom from the initial proton energy $E_{\text{init}} = (99.91 \pm 0.40)\,\text{MeV}$. Working with the energy-dependent stopping power for protons published by the PSTAR database [27], the expected deposited energy in silicon $dE_{\text{expected,SI}}$ was estimated. The energy-dependent conversion between the stopping power of protons in water and silicon using the PSTAR tables was performed successfully by other groups in previous studies [111]. For clarification, the conversion process is outlined in Figure 7.2.

Figure 7.2: Calculation of the expected deposited energy in 200 µm silicon $dE_{\text{expected,Si}}$ using the NIST database, the WET of the RW3 plates, and the WET of the corresponding ROI for the staircase phantom. [20]

During the conversion, the uncertainties on the individual energy levels must also be taken into account because they determine the uncertainty of the expected energy

deposition $dE_{\text{expected,SI}}$.
Firstly, the initial proton energy spread does not affect the uncertainty calculation because it is included in the statistical uncertainty of the measured deposited energy. Moreover, the uncertainty of the physical thickness of the RW3 slabs ($\sigma(t_{\text{RW3}}) = 0.1\,\text{mm}$[112]) and the staircase phantom have to be taken into account to the uncertainty of the $dE_{\text{expected,SI}}$. The uncertainty of the physical thickness of the custom-made staircase phantom is $\sigma_{\text{t}} = 0.1\,\text{mm}$ and that of the WER of the PMMA is $\sigma_{\text{WER}} = 0.02$, measured with a Giraffe detector (IBA Dosimetry, Schwarzbruck, Germany) (see measurement procedure in reference [2]).
For a conservative estimation of the uncertainty on $dE_{\text{expected,SI}}$, the largest possible water-equivalent thickness (WET) of the staircase phantom $\text{WET}_{\text{stair}}$, and the RW3 slabs WET_{RW3} were subtracted from the CSDA range of E_{init}. The resulting CSDA range $\text{CSDA}_{\text{sensor}}$ can be converted into the energy of the protons hitting the sensor E_{sensor} and the expected energy deposition $dE_{\text{expected,SI}}$ by using the PSTAR database and considering the thickness of the sensor.

7.3 LET approximation thin detectors

The energy deposition dE per unit length dl in a target medium induced by a particle is defined as Linear-Energy-Transfer (LET):

$$\text{LET} = \frac{dE}{dl}. \tag{7.1}$$

Without setting an upper threshold for the energy of secondary ionization electrons for the LET determination, it is conventionally referred to as *unrestricted* LET and equals the electronic stopping power. [35, 113]
Turning to the investigation of mean energy depositions in thin detectors, it is common to rely on the approximation in which the traversed length dl equals the thickness of the detector th. Based on that, the mean of the deposited energy distribution in thin detectors corresponds to the LET, assuming the latter remains constant over the detector thickness. [114]
The approximation is valid if the incident angle of the protons concerning the normal of the detector's surface is $\beta = 0\,°$, since $dl = \frac{th}{\cos\beta}$. For clarification, the

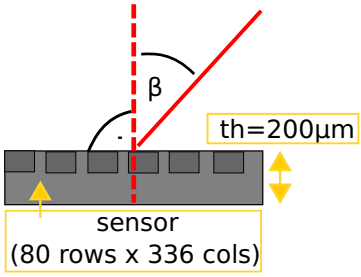

Figure 7.3: Sketch to visualize the normal of the detector's surface and the related incident angle β. For clarification the sensor thickness $th = 200\,\mu\text{m}$ and the pixelation are highlighted. [20]

incident angle β is highlighted in Figure 7.3. Unless otherwise stated, the following measurements are performed with $\beta \approx 0\,°$. The manual alignment of the detector on the treatment table leads to uncertainties of $0.5\,°$, negligible here.

The protons are scattered in the absorber and range shifter placed upstream of the detector during the measurements. Due to this, the incidence angle distribution of the protons is broadened. The latter was evaluated using Geant4 simulations developed and performed by J. Hohmann as part of her master's degree project.

The simulation consists of $5 \cdot 10^6$ protons with $E_{\text{int}} = 99.91\,\text{MeV}$ being shot on water phantoms with thicknesses corresponding to the WET of the phantoms used during the measurement campaign. After traversing the water phantom, the scattering angle distribution and the energy of the protons are scored at a distance of 15 cm from the water phantom. We define the maximum spread of the protons as twice the standard deviation of the scattering angle distribution because this includes $\approx 68.2\,\%$ of all protons.

Using the largest thickness of the water phantom of 74 mm as a conservative estimation, the maximum spread of the protons was smaller than 6° resulting in a deviation of the path length from the detector thickness of only $0.5\,\%$. Based on this, the length dl was approximated to be the detector thickness th. Considering the beam model used at the WPE, the beam divergence for the chosen beam energy is around $0.3\,°$. Since the beam divergence is small compared to the spread induced by the absorbers, it will be neglected in the scope of this thesis.

In addition to the scattering distribution, the energy distribution of the protons is also broadened and shifted to lower energies after the particles interact with the phantom and range shifter. The simulation for the largest thickness of the water phantom

(74 mm) reveals a deviation in the mean proton energy of only 2 % compared to the expected proton energy given by the NIST PSTAR database. Considering the simulation results, the impact of the energy straggling on the mean deposited energy was neglected here.

7.4 Characterization deposited energy spectra

The first step to prove the feasibility of the ATLAS IBL pixel detector for proton beam energy measurements is to investigate the detector response during irradiation with a monoenergetic proton field. As introduced in section 4.5, the FE-I4B readout chips provide information on the hit position, the timing of the hit, and the deposited energy in the sensor. The latter is processed as ToT and depends on the energy of the particles impinging the detector. Limiting factors for the number of deposited charges that can be detected is the 4-bit storage of the ToT information and the tuning setting of the readout chip.
The charge deposited by a traversing particle can be spread over several pixels. On the one hand, particles that hit the sensor with incident angles $\beta \neq 0$ traverse through more than one pixel while depositing their energy. On the other hand, the generated charge carriers can drift and then be collected in adjacent pixels. Therefore, the hits must be attributed to clusters described in section 4.8 before starting the analysis procedure.

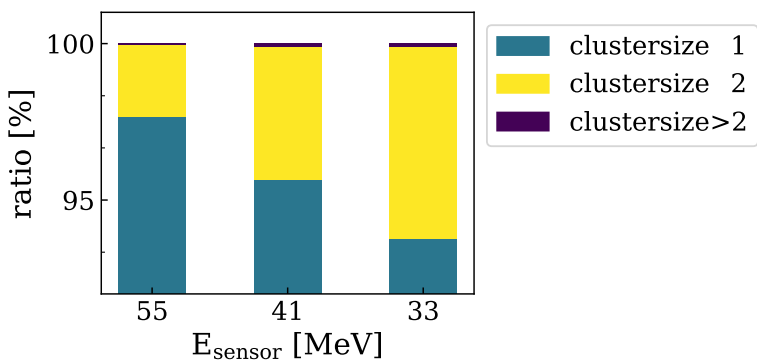

Figure 7.4: Cluster size distribution for protons with three different beam energies. The measurements were taken with a 200 µm thick detector and the same tuning.

To prove the influence of the charge sharing or clustering, cluster size distribution taken with different proton beam energies was characterized. The latter is shown in Figure 7.4. It is noticeable that the number of clusters consisting of two or more hits increases with decreasing proton energy. The increase is due to the larger number of created electron-hole pairs inducing an increased spread during the charge collection process with decreasing energy [115]. Finally, the charge can be collected by several adjacent pixels, referred to as charge sharing. [84]

The readout chip's limited range for charge processing also restricts the cluster size distributions. The restriction is proven by taking into account the proton hits registered in the overflow bin. Doing this, the number of clusters consisting of two hits for a proton energy of $E_{\text{init}} \approx 55\,\text{MeV}$ is more than doubled. This fact allows the conclusion that these clusters can potentially be assigned to low-energy protons with a high energy deposition. Since clusters containing overflow hits are excluded from the analysis, the average energy deposition is expected to be underestimated.

In addition, we assume that the duration of the sensitive time of the detector per trigger signal affects the cluster size distribution, too. Supplemental measurements were performed at the University Proton Therapy Dresden (UPTD) to verify this assumption.

The results indicate an enhancement of clusters consisting of two or more hits for proton fields in the same energy range when the sensitive time per trigger is expanded to the maximum by setting the TrigCnt parameter to 16. Accordingly, 16 trigger pulses spaced by one clock of 25 ns (1 BCU) are sent per trigger command.

For proton energies in the range of 50 MeV to 60 MeV, the mean ratio of protons depositing their energy in only one pixel drops to 87 %. The longer sensitive window per trigger command enables the measurement of charge that spreads out to be collected in an adjacent pixel but in another BCU, then the charge produced in the first hit pixel. Due to the time-walk effect introduced in section section 4.3, small charge pulses are measured with a time delay. Hence, the small charge pulses are not detected in a single BCU, leading to smaller cluster sizes when the sensitive time is limited.

In conclusion, the findings imply that a sensitive time per trigger of only 1 BCU and the chosen tuning settings disable the measurement of many clusters with cluster sizes larger than 1 for protons in the investigated energy range.

Following the ToT calibration and the clustering, the deposited energy per proton is investigated. It is described by the summed deposited energy per cluster.
Prior to the measurements, the tuning of the readout chips has to be adjusted to the proton energies. Despite the recommended maximum charge of 100 ke that the readout chip can process [1], we chose tunings that exceed the advice for the higher ToT bins. The tuning settings are listed in Table 7.1.

Table 7.1: Tuning settings of the detector used for the energy deposition measurements. The thickness of the sensor. the charge threshold and the ToT at target charge are listed.

sensor thickness	threshold	ToT at target charge
200 µm	41.000 e	6ToT@75.000e
100 µm	20.000 e	6ToT@62.000e

These settings are chosen to allow the measurement of the energy deposition of low-energy protons. For examples, protons with energies lower than 69 MeV ($th = 200\,\mu m$) and 28 MeV ($th = 100\,\mu m$) create more than 100 ke charges in the sensor on average.
In addition, the setting HitDiscConf = 2 was chosen for the measurement with the thicker sensor to account for the high energy depositions. The readout electronics and tuning settings are explained in section 4.5 in detail.

Figure 7.5 shows energy deposition spectra for different sensor thicknesses and proton energies. The center and width of the single bins are chosen according to the mean expected energy deposition per ToT. It is given by the tuning setting and therefore accommodates the non-linearity of the ToT calibration. The total ToT of a cluster containing more than one hit can exceed the maximum value for an individual hit of 13. Although multiple possible combinations can lead to the same value of the cluster ToT, the width of the higher bins is chosen to be equal to that of an individual hit of ToT 13.
The deposited energy spectra can be described by a Landau distribution convoluted with a Gaussian distribution (Langau) [116]. As part of this thesis, different methods were tested to fit a Langau function to the measured spectra using the non-linear

method of least squares (*curve_fit* from *scipy.optimize*) provided by Python. Only the first 13 bins are taken into account for fitting. Thus, distortions of the fit induced by clusters depositing charges that exceed the maximum value for an individual hit of 13 are avoided.
Starting to fit a Langau convolution provided by *pyLandau* [117], we ended up fitting a Gaussian distribution first and subsequently used the determined fit parameters as predictions for starting values of the Langau fit. The resulting Langau fits are highlighted orange in Figure 7.5.

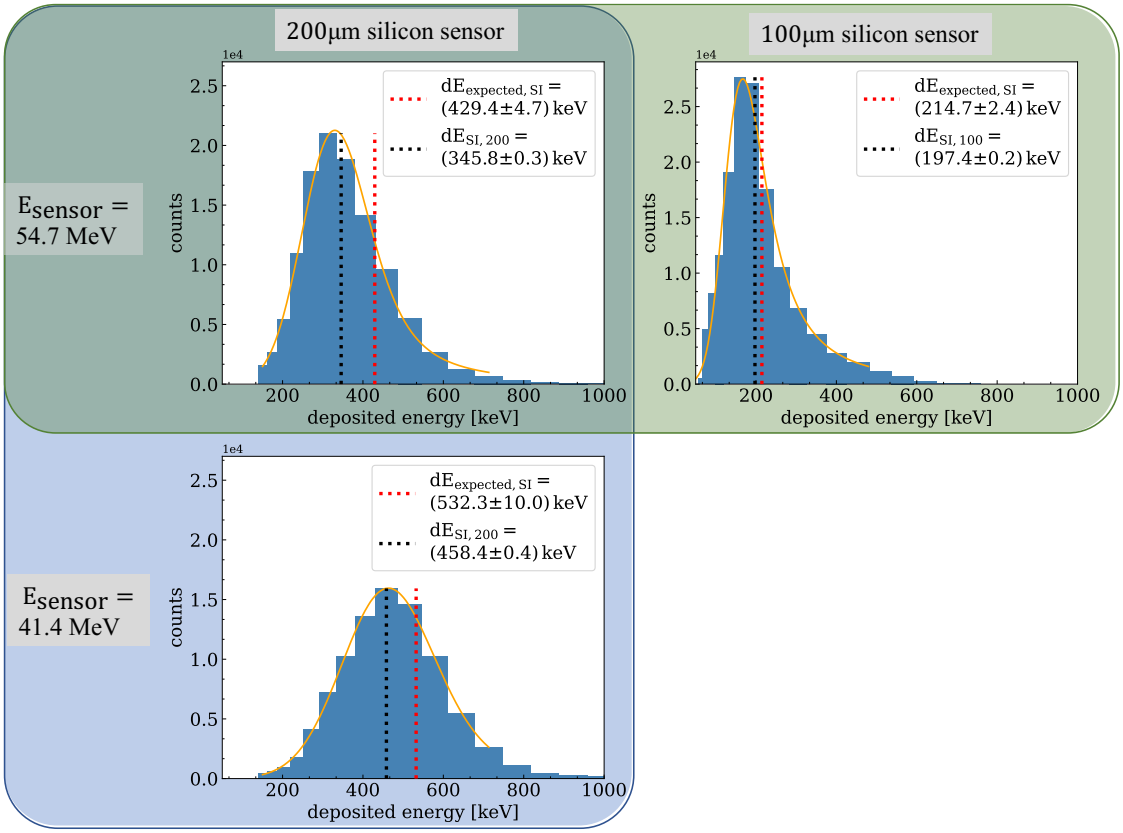

Figure 7.5: Deposited energy spectra measured with a 200 µm (highlighted blue) and a 100 µm thick silicon sensor with different tunings for a beam energy of $E_{\text{sensor}} = (54.6 \pm 0.8)$ MeV. In comparison, a deposited energy spectrum measured with the same 200 µm thick silicon sensor identically tuned, but for a beam energy of $E_{\text{sensor}} = (41.4 \pm 1.0)$ MeV is highlighted in green. The shapes of the spectra are fitted using a Langau fit (orange graph).

The energy straggling and scattering of the protons when using the range shifters and absorbers during the measurement campaign, as well as the non-linearity of the ToT calibration, leads to a widening of the energy deposition distribution. Therefore, the fits do not describe the energy deposition very well, so we use the arithmetic mean to estimate the mean deposited energy in the sensor $dE_{\mathrm{SI,th}}$. The estimator $dE_{\mathrm{SI,th}}$ is highlighted as a dotted black line in Figure 7.5.
Turning to a qualitative description of the exemplary spectra shapes, the peak width increases with decreasing proton energy. The reason is the increased energy deposition in the sensor, just like the non-linearity of the ToT Calibration, and the propagated energy straggling and scattering of the protons in the thicker range shifters. The latter will be extensively discussed in section 7.5.
When comparing the energy spectra measured with sensors of different thicknesses and with different tuning settings for the proton energy of $E_{\mathrm{sensor}} = (54.6 \pm 0.8)\,\mathrm{MeV}$, we notice that the peak shifts to lower energy depositions if measured with the 100 µm thick sensor. Since about half the amount of electron-hole pairs is generated in the sensor at half the thickness, this confirms expectations. Moreover, $dE_{\mathrm{SI,100}}$ demonstrates less deviation from the expectation than $dE_{\mathrm{SI,200}}$ because the varied tuning settings changed the range of the deposited energies that can be measured with the device under study. Furthermore, the smaller energy deposition in the thinner sensor fits the specifications of the readout electronics.
Overall the results indicate that the estimator for the mean deposited energies $dE_{\mathrm{SI,th}}$ underestimates the expected energy deposition $dE_{\mathrm{expected,SI}}$ provided by the NIST PSTAR database and shown as dotted red line in Figure 7.5. Further investigations on the underestimation of the mean deposited energies for measurements with various proton energies are presented in section 7.6. In conclusion, the main aspects that have to be taken in mind when using the detector under study for energy deposition measurements are listed:

- FE-I4B readout chip is designed to process a maximum charge of 100 ke. Therefore for measurements of low-energy protons the usage of thin sensors ($th \leq 100\,\mu\mathrm{m}$ thick) is recommended. However, using thinner sensors leads to a loss of statistics that must be compensated.

- FE-I4B readout chip is developed for the tracking of high-energy particles. Therefore the ToT values are stored in only 4-bit resolution leading to a rough

binning of the spectra. As a result, the tuning setting has to be specially adapted to the expected deposited energy in the sensor. Finding a suitable tuning can be done using the NIST PSTAR database or a Geant4 simulation. Further discussions on the influence of the tuning settings on the measured energy spectra take place in the following section.

- The sensitive time of the detector per trigger command and the trigger frequency bias the results by reducing the number of clusters with more than one hit for a shorter sensitive time.

7.5 Impact of tuning setting

Since the investigation of the measured deposited energy spectra in the silicon sensor revealed an underestimation, Geant4 simulations were performed to evaluate the influence of the binning of the energy deposition spectra on the estimator $dE_{\mathrm{SI,th}}$.
J. Hohmann developed the Geant4 simulation as part of her master's degree project. A point source was placed in front of a silicon detector plane with an area of $10 \times 10\,\mathrm{cm}^2$ and a thickness of 200 µm. The vacuum was chosen as the surrounding material so that the $1 \cdot 10^6$ protons with an energy of 55 MeV do not undergo scattering or energy loss before hitting the sensor. The energy of the simulated protons was chosen to match the experiment.
The simulation result is presented in Figure 7.6(a). Highlighted as the dotted line, the arithmetic mean of the finely binned distribution $dE_{\mathrm{SI,sim.}}$ is given. It agrees with the NIST PSTAR database prediction of $dE_{\mathrm{expected,\ SI}} = 426.7\,\mathrm{keV}$ within 0.2 %. The small deviation can be explained by different ionization energy values for water used in NIST [118] and for Geant4 simulations [119].
When considering the usage of the detector under study, the binning is adjustable via the tuning settings of the readout electronics. Therefore, the impact of the tuning settings on the mean deposited energy that one can get from the measured spectrum is investigated. Three different tuning settings were tested on the simulated data based on ToT and assuming a linear calibration.

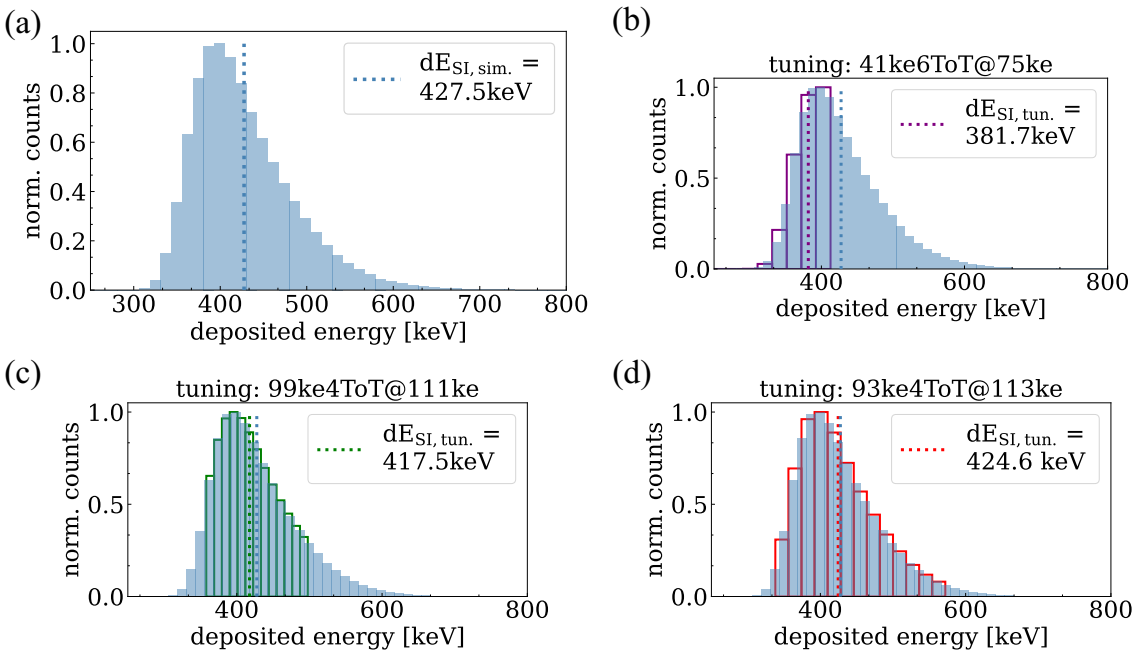

Figure 7.6: Simulated deposited energy spectra for 55 MeV protons in 200 µm silicon sensor (a). Different tunings of the readout electronics and the resulting shift of the mean deposited energy $dE_{\mathrm{SI,tun.}}$ are highlighted ((b)-(d)).

The first tuning presented in Figure 7.6(b) approximates the tuning used during the measurement. With an energy range of about $(148 - 413)$ keV, the chosen tuning cannot map the entire energy spectrum of the 55 MeV protons. Additionally, the arithmetic mean of the distribution underestimates the expected mean deposited energy by around 11 %. For measured mean deposited energies in the same proton energy range, the underestimation is around 19 %, indicating that the limited energy range is not the only reason for underestimating the mean deposited energies. The excess of the recommended maximum processible charge of 100 ke of the readout chip, the non-linearity of the ToT calibration, and deviations in the thickness of the sensor also bias the measured energy deposition spectra.

Various tuning settings were tested to determine how to tune the readout chip for energy deposition measurements. Figure 7.6(c) presents a tuning with an energy range of $(358-498)$ keV. It was adjusted on the principle that the expected mean deposited energy should be the center of the energy range. The deviation of around 2 % between the mean deposited energy of the binned data $dE_{\mathrm{SI,tun.}}$ and the expectation implies that there is the need for an additional regulation to set an appropriate tuning.

Therefore Figure 7.6(d) highlights a tuning where all deposited energies with bin entries over 5 % of the maximum count are included in the energy range, which is, in this case, $(338 - 572)$ keV. Applying this tuning to the simulated energy spectra, the deviation on the determined mean deposited energy decreases to 0.7 %. Those results show that the energy range set by the tuning should cover a wide range of the energy spectrum around the expected mean deposited energy. Nevertheless, the spectrum's binning must also be considered as it defines the resolution.
For further development of readout chips adapted to requirements in proton therapy applications, an extension in the maximum processible charge and on the 4-bit storage of the ToT information would be appropriate. Both improvements would lead to better coverage of the deposited energy spectra, even in the range of protons that generate more than 100.000 electrons in the sensor.

7.6 LET spectra measurements

The previously presented results indicate that a direct measurement of the beam energy utilizing the mean deposited energy is unfeasible with the applied tuning settings listed in Table 7.1. Nevertheless, we assume the mean energy deposition $dE_{\text{expected,SI}}$ to be proportional to the initial proton energy and, therefore, could be used as an estimator to determine the proton energy. To verify the assumption, energy spectra of various proton beam energies have to be investigated.
Three custom-made Poly(Methyl Methacrylate)(PMMA) staircase phantoms were stacked on the detector to speed up the measurement campaign. With this, different proton energies are measured simultaneously in the different regions on the pixelated detector. The three phantoms consist of a different number of blocks (two, four, and nine) with physical thicknesses th_{block} between 10 mm and 26 mm. Using an MLIC Giraffe detector (IBA Dosimetry, Schwarzenbruck, Germany), the WER of the PMMA was determined to be $\text{WER}_{\text{PMMA}} = 1.16 \pm 0.02$, comparing Behrends *et al.* [2].
A picture of the staircase phantom with nine blocks placed upstream of the detector is shown in Figure 7.7.

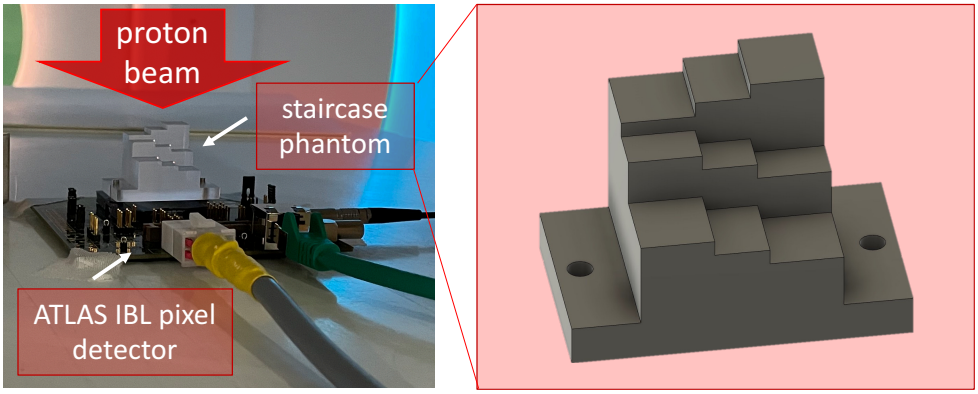

Figure 7.7: Experimental setup to characterize the energy deposition of the protons in the silicon sensor of the ATLAS IBL pixel detector after traversing a custom-made PMMA staircase phantom.

Corresponding to the blocks of the staircase phantom, the detector area is divided into regions of interest (ROIs). The influence of scattered particles at the edges of the blocks is avoided by defining the ROIs to be smaller than the respective block. The remaining energy E_{sensor} of the protons impinging the sensor within one ROIs is assumed to be the same.

Two measurements each were performed with an initial proton energy of $E_{\text{init.}} = 100\,\text{MeV}$ and RW3 slabs with a physical thickness of 4.0 cm and 4.4 cm downstream of the nozzle. This results in energies impinging the sensor E_{sensor} between 12.1 MeV and 52.7 MeV. The energy range was selected so that the readout electronics of the detector are maxed out with the high amount of produced charge while the stopping power of the protons is no longer in the plateau region anymore.

One has to consider two main sources of uncertainties for the calibration of the deposited energies: that on the measured estimator $dE_{\text{SI,200}}$ and the systematic uncertainty of the expectation on the energy deposition $dE_{\text{expected, SI}}$. The latter was already discussed in section 7.2.

Analyzing the uncertainty on the estimator $dE_{\text{SI,200}}$, we have to consider the standard error of the mean value σ_{stat} because it quantifies the spread of the deposited energy. In addition, the uncertainty has to reflect slight tuning differences overall detector pixels. For an experimental estimation of the uncertainty component, referred to as σ_{tune}, a homogeneous proton field with $E_{\text{init}} \approx 54.7\,\text{MeV}$ is used to irradiate the detector. The average relative standard deviation over the nine different regions is

found to be $\frac{\sigma_{\text{tune}}}{dE_{\text{SI,200}}} = 1.20\,\%$.
As these uncertainties are not correlated, they are added in quadrature to the total uncertainty of $\sigma_{\text{dE,SI}} = \sqrt{\sigma_{\text{stat}}^2 + \sigma_{\text{tune}}^2}$.

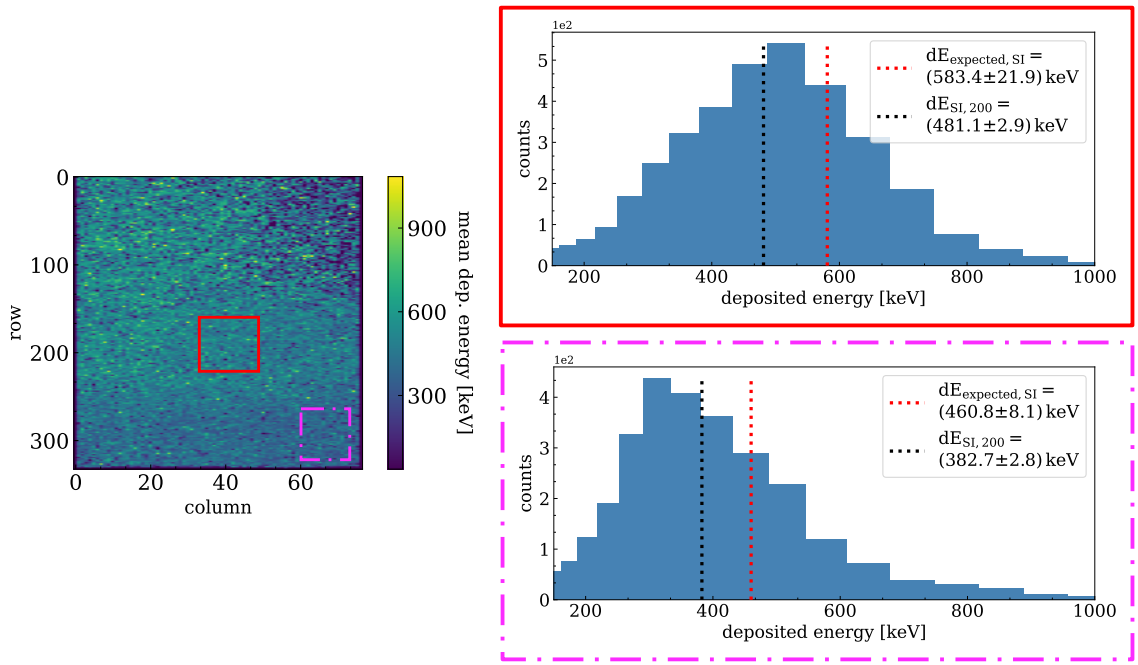

Figure 7.8: Map of mean deposited energy in the sensor downstream of the staircase phantom with nine thickness regions measured with a proton energy of $E_{\text{phantom}} \approx 65.4\,\text{MeV}$. For illustration, two regions of interest and the corresponding deposited energy spectra are highlighted. updated [20]

Figure 7.8 shows a map of the mean deposited energy per pixel measured for exemplary energy of $E_{\text{phantom}} \approx 65.5\,\text{MeV}$ with the staircase phantom outlined in Figure 7.7. To exemplify the changing mean energy depositions downstream of different blocks of the staircase phantom two ROIs are highlighted on the mean deposited energy map. The corresponding energy deposition spectra are presented next to it. The ROI bordered with the purple dotted line is taken downstream of the staircase phantom block $th_{\text{block,9}} = 1.2\,\text{cm}$, and the ROI bordered in red downstream of the phantom block $th_{\text{block,5}} = 2.0\,\text{cm}$. The various E_{sensor} for protons hitting the sensor in the different ROIs result in a shift of the peak of the deposited energy spectra. By comparing the mean deposited energy estimator $dE_{\text{SI, 200}}$ with the expected energy deposition $dE_{\text{expected, SI}}$ an underestimation is noticeable, as it

was also observed in section 7.4.

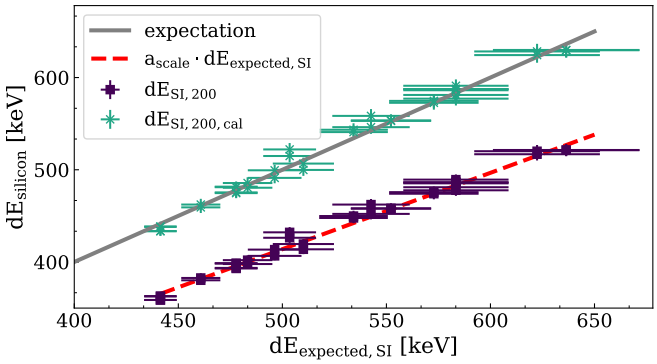

Figure 7.9: Mean deposited energy in silicon $dE_{\mathrm{SI,200}}$ versus expected mean deposited energy $dE_{\mathrm{expected,\ SI}}$. Compare results before (purple squares) and after the calibration procedure (green crosses) with $a_{\mathrm{scale}} = (0.827 \pm 0.002)\,\frac{1}{\mathrm{keV}}$. updated [20]

The correlation between the measured mean deposited energy $dE_{\mathrm{SI,200}}$ and the expectation $dE_{\mathrm{expected,\ SI}}$ for all energies E_{sensor} in the range of the selected tuning is shown in Figure 7.9, marked purple. As described in section 4.5, the adjustable tuning settings determine the detector's dynamic range. Therefore a lower energy limit $E_{\mathrm{sensor,min}} = 30.4\,\mathrm{MeV}$ is defined to be the proton energy where the expected mean deposited energy in the sensor coincides with the center of the penultimate ToT bin. Proton energies lower than the energy limit are excluded from the analysis, and the corresponding data points are not shown in Figure 7.9.

A systematical underestimation of the reference values is revealed, considering the results presented in Figure 7.9. It is visible as a shift of the data points from the expectation highlighted in grey. Nevertheless, the proportionality of the mean energy deposition $dE_{\mathrm{expected,SI}}$ and the reference values is demonstrated. Due to this, the assumption of the estimator $dE_{\mathrm{SI,200}}$ being proportional to the proton energy is confirmed. A calibration procedure is developed to use the estimator $dE_{\mathrm{SI,200}}$ for proton energy determination.

The estimator $dE_{\mathrm{SI,200}}$ can be scaled to agree with the expected energy deposition using a linear scaling with a factor a_{scale}. The parameter $a_{\mathrm{scale}} = (0.827 \pm 0.002)\,\frac{1}{\mathrm{keV}}$ has been determined using an orthogonal distance regression *ODR* from *scipy.odr*. The latter lets us take into account uncertainties on $dE_{\mathrm{expected,\ SI}}$ as well as $dE_{\mathrm{SI,200}}$.

The scaled measurement results are referred to as $dE_{\mathrm{SI,200,cal}}$ illustrated by green markers in Figure 7.9. The associated uncertainties $\sigma_{\mathrm{dE,SI,200,cal}}$ are calculated utilizing Gaussian error propagation:

$$\sigma_{\mathrm{dE,SI,200,cal}} = \sqrt{\left(\frac{\sigma_{\mathrm{dE,sensor}}}{a_{\mathrm{scale}}}\right)^2 + \left(\frac{dE_{\mathrm{SI,200}}}{a_{\mathrm{scale}}^2} \cdot \sigma_{\mathrm{a_{scale}}}\right)^2}. \tag{7.2}$$

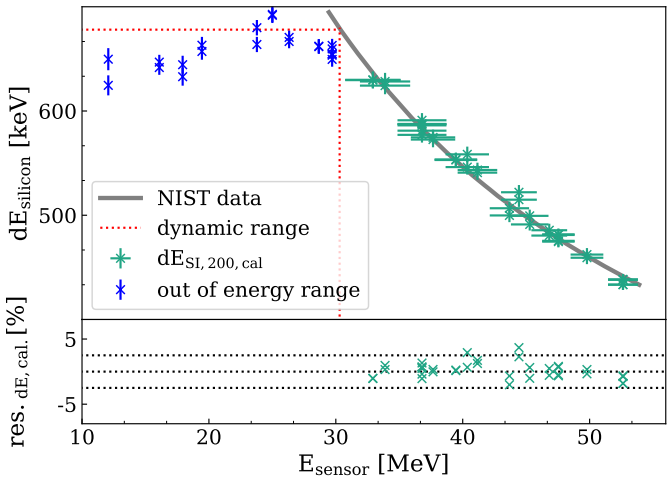

Figure 7.10: Relative deviation of the calibrated results $dE_{\mathrm{SI,200,cal.}}$ and the reference values published by NIST PSTAR database. The data points below $E_{\mathrm{sensor,min}} = 30.4\,\mathrm{MeV}$ are excluded from the analysis due to the limited energy range of the chosen detector tuning. updated [20]

Looking at Figure 7.10, the promising calibration results become apparent quantified by a mean average deviation of only 1.02 % between the calibrated measured mean energy deposition and the NIST PSTAR database.
All data points excluded from analysis for proton energies that go below $E_{\mathrm{sensor,min}}$ are marked as blue markers in Figure 7.10.
The calibration procedure and the applied uncertainties on the measured mean deposited energy are verified by performing a so-called *leave-one-out-cross-validation*. Thereby the calibration procedure is performed several times while excluding one data point as a test data point. We repeated the validation for every data point and calculated the pull of the calibration:

$$\mathrm{pull} = \frac{dE_{\mathrm{SI,200,cal}} - dE_{\mathrm{expected,200}}}{\sigma_{\mathrm{dE,SI,200,cal}}}. \tag{7.3}$$

By analyzing the histogrammed pull, the applied uncertainties can be evaluated. A proper uncertainty estimation is indicated by a Gaussian distribution of the pull with a standard deviation of 1 and a mean of 0. Shifts of the distribution indicate a systematical deviation between the measured data and the reference, whereas a standard deviation $\sigma_{\text{pull}} < 1$ points out the underestimation of the uncertainties. As shown in Figure 7.11, the pull values are distributed around about zero with a standard deviation of $\sigma_{\text{pull}} = 1.06$. By this, an appropriate uncertainty determination is indicated.

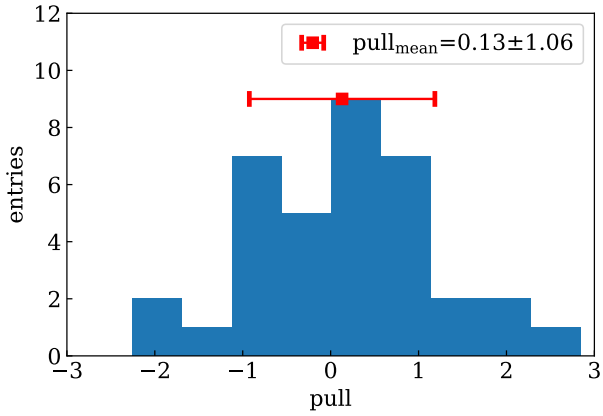

Figure 7.11: Histogrammed pull for energy deposition calibration procedure. The mean pull and the corresponding standard deviation are marked. updated [20]

Proton range deviations of 1 mm have to be detected to apply the detector under study for daily QA beam energy verification in proton therapy facilities [38]. Once again, the validation procedure allows an estimation of the resolution of the residual proton range. Again the unbiased calibration is performed several times, excluding one data point at a time. Subsequently, the calibration is used to determine the proton energy and range of the respective test data point. The conversion between proton energy and range is again based on the NIST PSTAR database.

Transferred to the presented results, we define a distinguishable range difference if it is larger than twice their uncertainties σ_{range}. The results are plotted in Figure 7.12. The upper energy limit to fulfill the daily QA requirements for the

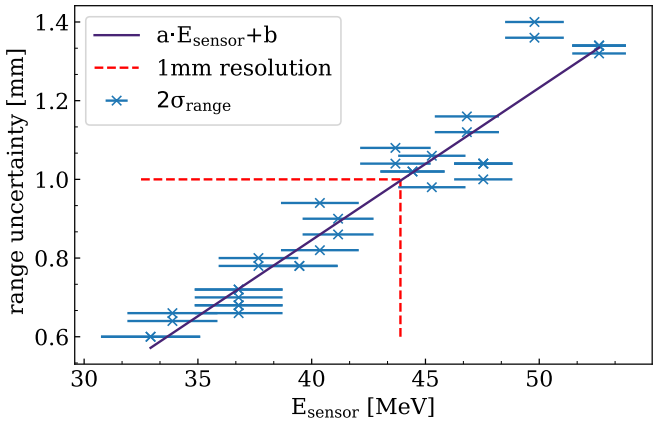

Figure 7.12: Uncertainty of the measured proton range in water corresponding to the expected proton energy impinging the sensor. A linear fit is used to determine the upper energy limit $E_{\text{max}} = (44.0 \pm 2.9)$ MeV to fulfill the daily QA requirements (marked red). updated [20]

selected tuning is determined via a linear fit using an orthogonal distance regression (gradient $a = (0.039 \pm 0.002)\,\frac{\text{mm}}{\text{MeV}}$, interception $b = (-0.702 \pm 0.078)$ mm) to be $E_{\text{max}} = (44.0 \pm 2.9)$ MeV. Notice that this energy limit has to be set for the energy of the protons impinging the sensor. As presented here, using different range shifters in front of the detector enables the measurement of higher initial beam energies. Still, the extended energy straggling in the range shifter must be considered conscientiously.

Looking at the results, important conclusions for the usage of ATLAS IBL pixel detectors for proton beam energy measurements can be drawn:

- The results presented here are only valid for the applied tuning settings. The calibration procedure must be repeated when using other tuning settings or sensors.
- Deviations of the mean deposited energies caused by variations in the sensor thickness are taken into account utilizing the calibration.
- Calibration has to be repeated regularly due to the influence of radiation damage and treatment machine adjustments.

- Different values of the ionization energy for water used in NIST [118] and Geant4 simulations [119] do not affect the calibration because we use the same NIST reference for the measurement and the calibration.

7.7 Track LET measurements

Another way to use the pixelated detector for range measurements in proton therapy is to track the single protons on their way through the sensor. Therefore, the detector under study is orientated parallel to the beam axis.

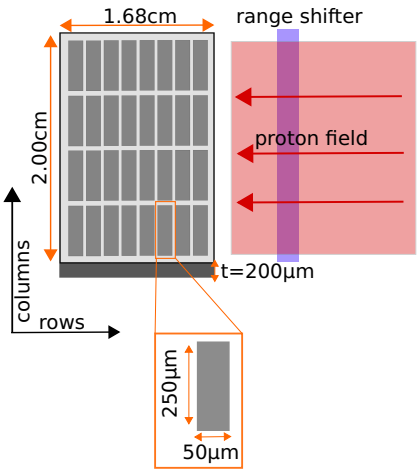

Figure 7.13: Sketch to clarify the orientation of the detector with respect to the proton beam direction. The pixel size and sensor dimensions are highlighted.[20]

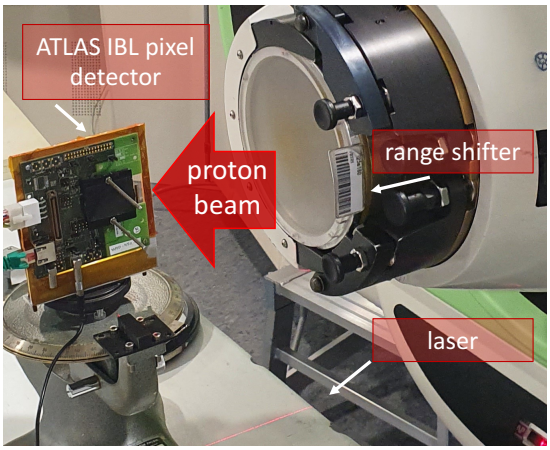

Figure 7.14: Experimental setup to track the energy deposition of single protons while traversing the sensor. The detector is mounted on a goniometer and aligned parallel to the beam axis. modified [20]

Taking advantage of the small pixel size in the beam direction of 50 µm, the energy deposition per pixel for individual protons along their track potentially enables a precise beam energy determination. Figure 7.13 illustrates the orientation of the detector with respect to the beam direction. The experimental setup of the detector under study placed on a goniometer is shown in Figure 7.14. The integrated laser

system of the fixed beam treatment room at the WPE is used for the manual alignment of the detector parallel ($\beta = (90\,° \pm 0.5\,°)$) to the beam axis.
Just as during the previous measurements, clinical range shifter and RW3-plates are utilized to generate proton energies between $E_{\text{sensor}} \approx 54.6\,\text{MeV}$ and $E_{\text{sensor}} \approx 16.6\,\text{MeV}$. The proton energies were chosen to make their continuous slowing down approximation range (CSDA range) in silicon smaller than the detector size in beam direction (1.68 cm). This implies that a proton traversing straight through the sensor is stopped completely. The size of the proton fields was adapted to cover the entire detector area. To extend the findings of the measurement studies, J. Wüller performed associated Geant4 simulations as part of her Bachelor's degree project.

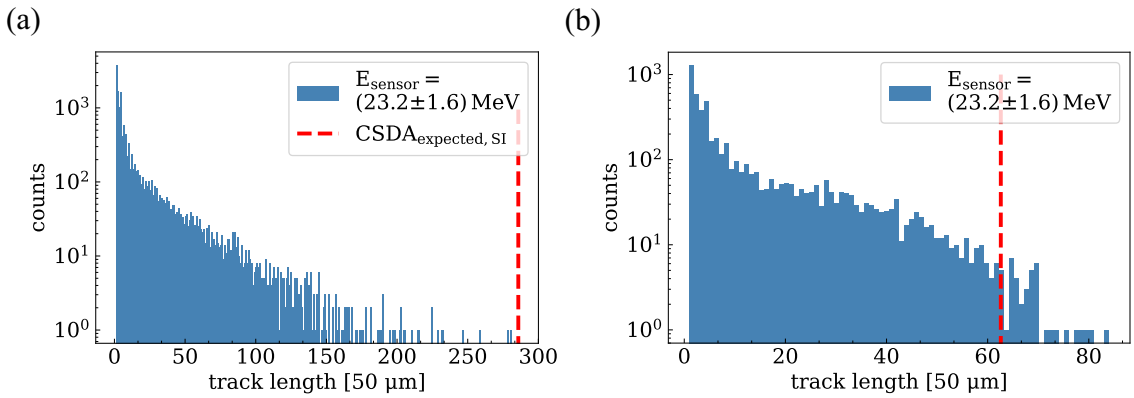

Figure 7.15: Track length distributions for parallel proton incidence with energies of $E_{\text{sensor}} = (54.6 \pm 0.8)\,\text{MeV}$(a) and $E_{\text{sensor}} = (23.2 \pm 1.6)\,\text{MeV}$(b). The expected CSDA range range is highlighted in red. [20]

Since several effects are influencing the measurement of individual protons tracks, the analysis procedure of the measured data has to be adapted:

- Due to the parallel incidence of the beam, a single proton deposits energy in several pixels on the way through the sensor. All those hits have to be assigned to one cluster. Towards the end of the range of the protons, the energy deposition per pixel increases as well as the probability of being registered as an overflow hit. In contrast with the clustering procedure explained in section 4.8, clusters containing overflow or small hits are not rejected, but the related hits are discarded here.

- Before depositing their total energy, a substantial amount of protons is scattered out of the sensor with its 200 µm thickness perpendicular to the beam direction. The influence of this effect on the track length distribution becomes apparent when considering Figure 7.15. For two different exemplary proton energies, it can be seen that there is a decline of large clusters' length towards the CSDA range caused by multiple Coulomb scattering. The probability of the protons being scattered with a larger angle increases with decreasing proton energy and increasing track length in silicon, see Equation 2.1. Therefore the track length distribution for higher energy protons (Figure 7.15(a)) features fewer tracks in the order of the CSDA range than the distribution for the lower energy protons (Figure 7.15(b)). The latter had to traverse only a shorter distance in the sensor.

- The path length of protons per pixel may be larger than the pixel width of $w = 50\,\mu\text{m}$ due to scattering. Since we accept w as the traversed distance per pixel to determine the LET, see Equation 7.1, an overestimated LET is measured. Only protons with little scattering can be measured as long clusters since only these protons can travel a long distance through the sensor. Therefore, it is striking that the longer the clusters are, the smaller the deviation from the expected traversed distance per pixel. The Geant4 simulations of J. Wüller confirmed this assumption. To account for this optimally without reducing the statistics of the measurement disproportionately only the upper 20 % of the longest clusters were taken to analyze the LET per track. This update of the analysis procedure was developed after publishing the proof-of-principle results in [20].

- Protons scattered out of and back into the sensor generate clusters with gaps, referred to as split clusters. The resulting cluster length may exceed the expected proton range because the protons lose less energy traversing through the air than through silicon. Split tracks are rejected from analysis by taking into account only clusters starting in the first 10 rows.

Turning to the obtained results, Figure 7.16 shows the mean deposited energy per pixel row averaged over the selected tracks $dE_{\text{SI},50}$ with the corresponding statistical uncertainties for proton energies of $E_{\text{sensor}} = (54.6 \pm 0.8)\,\text{MeV(a)}$ and $E_{\text{sensor}} = (23.2 \pm 1.6)\,\text{MeV(b)}$. Caused by the decreasing energy of the protons while

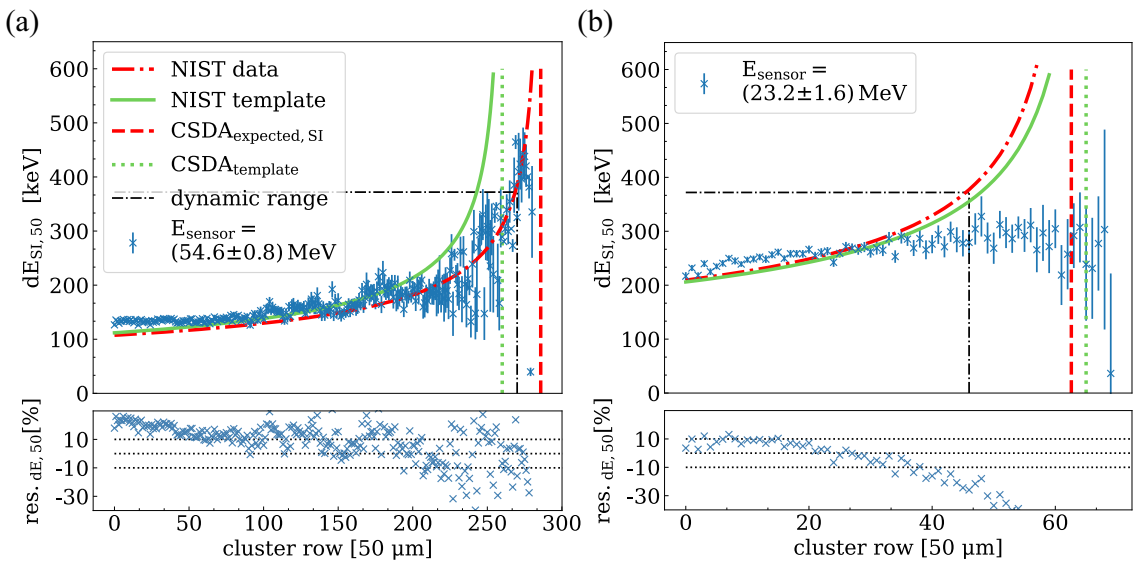

Figure 7.16: Mean energy deposition $dE_{\mathrm{SI},50}$ measured in beam direction along the proton tracks. Two different proton energies were used: $E_{\mathrm{sensor}} = (54.6 \pm 0.8)\,\mathrm{MeV}$(a) and $E_{\mathrm{sensor}} = (23.2 \pm 1.6)\,\mathrm{MeV}$(b). The estimated CSDA range is highlighted in green, with the corresponding deviation from the NIST PSTAR expectation (red lines) plotted below. Black dotted lines indicate the dynamic energy range of the detector. updated [20]

traversing the sensor, the pixel-wise energy deposition increases towards the end of the clusters; compare Figure 2.1. As a reference, the expected energy deposition curve and the CSDA range taken from the NIST PSTAR database are highlighted in red.

Looking at the deviation between $dE_{\mathrm{SI},50}$, and the reference curve shown in the bottom plot, we see that an overestimation of the energy deposition for pixels at the beginning of the track turns into an underestimation towards the end of the cluster. The overestimation in the first rows of the sensor is due to a scattering of the protons resulting in a longer traveled distance per pixel than expected. For higher energy depositions per pixel, the dynamic energy range of the chosen tuning for the readout chip comes into play, highlighted as a black line in Figure 7.16. As we already demonstrated in section 7.4, the limited energy range of the sensor leads to an underestimation of the deposited energy.

Nevertheless, a proof of principle method was developed to determine the proton beam energy utilizing the mean energy deposition along the tracks in the pixel row

direction, referred to as the *template method*. We started estimating the proton energy by comparing the longest measured track with the CSDA ranges published by NIST. Within an energy interval of ± 5 MeV in steps of 0.1 MeV around the energy estimation, the energy deposition curves were pulled from NIST and compared to the measured energy deposition curve. Subsequently, the best fitting curve is determined considering the minimum χ^{2*} value, highlighted as green lines for the energies in Figure 7.16. The corresponding proton energy or CSDA range given by NIST is defined as the measurement result.

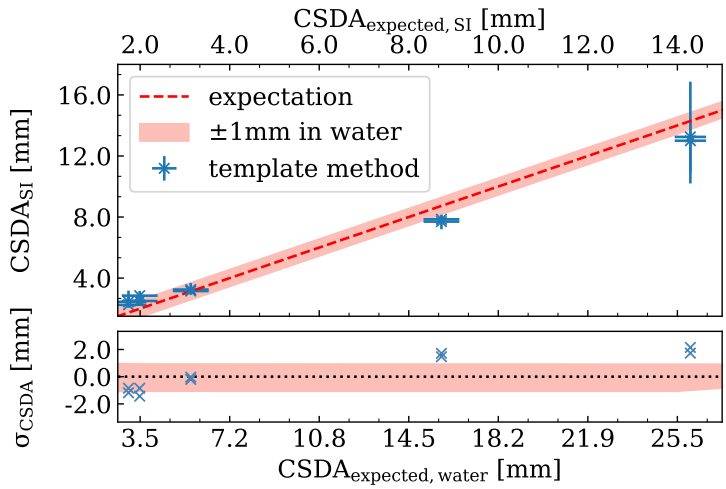

Figure 7.17: Measured CSDA_{SI} and the corresponding reference CSDA ranges in silicon and water published by the NIST PSTAR database. The light red band indicates an ± 1 mm range from the expected CSDA range in water. On the bottom, the deviation of the estimator σ_{CSDA} is illustrated. updated [20]

Due to the discussed scattering processes, most protons do not stop in the sensor. Therefore, the uncertainties on the determined proton energy are dominated by the leak to measuring individual protons' full energy deposition in the sensor. Consequently, the resulting influence of the low statistics for long tracks on the proton energy determination is estimated by randomly dividing all measured tracks in a subsample of 70 % 100 times. Afterward, the *template method* is performed on the subsamples. The resulting lowest and highest range defines the uncertainty interval on the measured range and CSDA range, respectively.

Figure 7.17 illustrates the measured CSDA range CSDA_{SI} compared to the reference

CSDA ranges in silicon and water published by the NIST PSTAR database. The $\mathrm{CSDA}_{\mathrm{water}}$ is discussed to compare the results with the requirements for quality assurance. Covering a range of 4.2 mm, the uncertainty interval for the highest proton energy is the largest because it suffers most from protons scattered out of the sensor. With decreasing energy, more protons deposit their total energy in the sensor leading to a more precise determination of the CSDA range.
With an average deviation from the expected CSDA range in the water of 1.28 mm, the precision for proton range determination of the *track LET measurement* is worse compared to the *LET spectra measurement* and cannot fulfill the daily QA requirements.
Nevertheless, the proof of principle study indicates that determining the range of the protons through tracking the energy deposition of individual protons through the detector is feasible. The following opportunities for improvement can be defined after taking the Geant4 simulation and the experimental results into account:

- Tuning settings of the readout chip adjusted to higher energy depositions enables the characterization of the energy deposition at the end of the range of the protons. To give a clue for further readout chip developments with an extended maximum processible charge, 5 MeV protons generate an average charge of 189 ke in 50 µm silicon [27].

- The statistics of the number of clusters should be enlarged by extending the measurement time. Based on this, the deposited energy along the proton tracks could be characterized only for protons that are completely stopped in the sensor.

- An experimental setup should be further developed for the automatic alignment of the detector. Investigating incident angles between $\beta = 0\,^{\circ}$ and $\beta = 90\,^{\circ}$ might improve the proton range determination because the expected track length for protons with higher energies shrinks. With decreasing track length, the possibility of protons being scattered out of the sensor decreases. In addition, characterizing the cluster shape for particles incident in non-perpendicular direction can provide additional information on the particle direction and track length in the sensor, as already shown for measurements with the miniaturized radiation camera Minipix [120].

Chapter

Energy deposition in platinum nanoparticles at macroscopic scale

8

One exemplary application making use of the features of the detector under study in the scope of a proton therapy application is published in the article *The radiosensitizing effect of platinum nanoparticles in proton irradiations is not caused by an enhanced proton energy deposition at the macroscopic scale* in Physics in Medicine & Biology **67**, 15 (2022) [2].

Based on studies demonstrating a dose enhancement effect in tumors enriched with noble metal nanoparticles (NPs), investigating so-called radiosensitizing effect is of great interest in radiobiological research [121]. Further introduction and theoretical background on NPs are given in the literature [122].

The tumor enrichment with metal NPs during particle irradiation potentially induces an enhanced radiotherapeutic effect and proton therapy efficiency [123]. Despite these promising prospects, the underlying mechanism substantiating the radiosensitizing effect of metal NPs still needs to be fully understood.

Particle-induced X-ray emission (PIXE) could lead to an increased dose deposition of the protons in the tumor target, but stopping power calculations revealed energy depositions far too low to support this assumption [124–126].

Another approach is the contribution of the secondary electrons generated by the protons. It is based on papers postulating that Auger electrons arising from secondary electrons release inner-atomic Auger cascades in the NPs. The latter induces hydroxyl radicals by the radiolysis of the surrounding water molecules and may cause increased dose deposition. [127]

By contrast, another study postulates that the radiosensitizing effect of gold NPs utilized during photon irradiation is based on chemical reactions at the NPs and water molecules interfaces by catalytic processes. The chemical reactions boost the radiolysis of the adjacent water molecules. [128]
Despite the various interpretations of processes leading to the increased effectiveness of the radiolysis, the impact of the occurring reactive oxygen species (ROS) on the radiosensitizing effect is proven by *Zwiehoff et al.*, for example [129].

8.1 Introduction to study structure

For the sake of contributing to the ongoing scientific discussion, an experimental study investigating the lack of correlation between the radiosensitizing effects induced by platinum NPs (PtNPs) and an increased proton energy deposition at a macroscopic scale was initiated within the MERCUR graduate school "Präzisionsprotonentherapie— Praxisbezogene Physik und Chemie an der Schnittstelle zur Medizin". All measurements in the scope of this study were performed at the WPE. The treatment facility with the corresponding treatment machine is introduced in section 2.2.
Colleagues at the University of Duisburg-Essen produced tissue-like samples containing PtNPs (PtNP cubes) and reference samples without PtNPs (nonPtNP cubes). Pulsed laser ablation is used to generate the surfactant-free PtNPs with a mean diameter of (40 ± 10) nm, see F. Waag *et al.* [130]. During a gelation process, the PtNPs were mixed with gelatin in a final concentration of $300\,\mu\mathrm{g\,ml^{-1}}$. The finished samples have a lateral dimension of about $30 \times 30\,\mathrm{mm}^2$ and a thickness in beam direction of about 20 mm, discussed in detail in the next section.
As a first step, the potential enhancement in proton therapy efficiency was proven by measuring an increased ROS generation for PtNP samples under proton irradiation. Turning to the investigation of the dose enhancement effect by means of experimental measurements, three different devices were utilized to detect differences in the proton dose and energy deposition downstream of the PtNP and the nonPtNP samples: a plane parallel ionization chamber in a motorized water phantom, a Multi-layer ionization chamber (Giraffe detector IBA Dosimetry, Schwarzenbruck Germany), and a hybrid pixelated semiconductor detector (ATLAS IBL Pixel Detector).

Deviations in the energy deposition indicate changes in the energy loss of the protons when traversing the PtNP samples. Compared to the other setups, the ATLAS IBL Pixel Detector is operated in sampling mode, which simultaneously enables the characterization of PtNP and nonPtNP samples. Additionally, it is an ionization chamber-independent setup, which complements the study perfectly. In cooperation with our colleagues from the WPE, we planned, performed, and evaluated the series of measurements with the ATLAS detector and thereby contributed to the above-mentioned paper.

8.2 Energy deposition comparison

This study aims to evaluate the influence of PtNPs on the energy deposition of protons. Therefore, various samples (abbreviated as cubes) spiked with PtNPs and without were stacked on the detector side by side for a simultaneous investigation. Varying the sample thickness and proton energy allows the energy-dependent examination of the proton energy loss.
The stacked samples were exposed with homogeneous fields having a lateral dimension of $25 \times 25\text{mm}^2$ and proton energies of 100 MeV, 110 MeV, or 120 MeV. To increase the energy deposition of the protons in the sensor additional buildup consisting of one clinical range shifter (Polymethyl methacrylate, WET = 51 mm) and an RW3-plate (WET = 5.2 mm) was placed upstream of the single cube setups. The detailed setup specifications are listed in Table 8.1.
An experimental setup to investigate the energy balance outside the different samples is shown in Figure 8.1. It consists of three nonPtNP and three PtNP samples stacked on the ATLAS IBL pixel detector. The measurements were performed with the same sensor of 200 µm thickness and unchanged tuning settings as the studies presented in section 7.4.
Starting with the measurement data analysis, the clustering has to be performed using the self-developed clustering software described in section 4.8. As discussed in the previous section, the updated clustering software leads to slightly changing results in the measured energy deposition concerning [2]. Still, of course, the findings of the campaign remain unchanged. In the last analysis step, hits in badly tuned

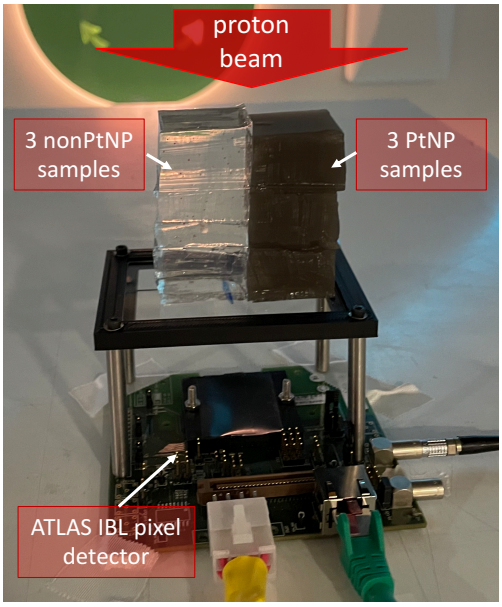

Figure 8.1: Experimental setup to characterize the energy deposition of the protons in the silicon sensor of the ATLAS IBL pixel detector after traversing the nonPtNP and the PtNP samples. (modified [2])

pixels are rejected: They were identified as pixels differing more than 1σ from the mean injected charge for a ToT value of 7 during ToT calibration, see section 4.6.

Based on the findings presented in the previous section, the arithmetic mean of the deposited energies per cluster $dE_{\mathrm{SI},200}$ is defined as an estimator for the mean deposited energy in the sensor. Downstream of the samples, two central ROIs on the detector are defined where the analysis procedure is performed. They are smaller than the samples to exclude artifacts in the edge regions.

Experimental uncertainties include variations in the pixel response over the detector and the reproducibility. Therefore the response is characterized without a sample, using a staircase phantom with nine different thickness regions. Two different orientations of the phantom stacked on the detector were measured repeatedly. After comparing $dE_{\mathrm{SI},200}$ downstream the different thickness regions, a mean deviation of the response across the detector of 1.17 % was determined and defined as uncertainty on the deposited energy.

As an example, the energy deposition spectra downstream the PtNP $dE_{\mathrm{SI,\ PtNP}}$ and nonPtNP samples $dE_{\mathrm{SI,\ nonPtNP}}$ with range shifters of 56.2 mm water equivalent thickness in front of the nozzle irradiated with the energy of 120 MeV are given in

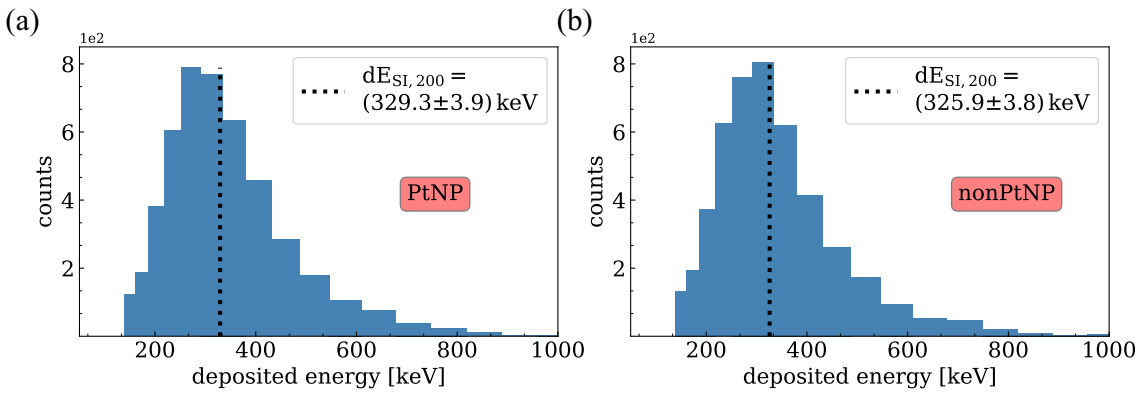

Figure 8.2: Deposited energy distributions of protons detected with in the silicon sensor (ATLAS IBL pixel detector) after traversing one PtNP (a) and one nonPtNP (b) cube. Absorbers with a WET of 56.2 mm were placed in front of the nozzle ($E_{\text{init}} = 120\,\text{MeV}$). updated [2]

Figure 8.2. The estimator $dE_{\text{SI,200}}$ is highlighted as a black dotted line. Considering the uncertainties, the mean energy deposition in the sensor is indistinguishable downstream of both samples.

Table 8.1: Measured mean deposited energies $dE_{\text{SI,200}}$ and mean deposited energy ratios $dE_{\text{SI,ratio}}$ for the different setups downstream the PtNP and nonPtNP samples. The 1σ interval takes into account the height ratio of the different samples. updated [2]

E_{init} [MeV]	Setup	$dE_{\text{SI,200}}$ [keV]		$dE_{\text{SI, ratio}}$	1σ interval
		PtNP	nonPtNP		
100	3 cubes	449.3 ± 5.3	467.7 ± 5.5	1.041 ± 0.017	[0.972, 1.036]
		449.0 ± 5.3	465.8 ± 5.4	1.037 ± 0.017	
110	1 cube, abso.	491.3 ± 5.7	487.7 ± 5.7	0.993 ± 0.016	[0.987, 1.013]
		491.5 ± 5.8	488.2 ± 5.7	0.993 ± 0.016	
120	1 cube, abso.	329.3 ± 3.9	325.9 ± 3.8	0.990 ± 0.016	[0.995, 1.007]
		326.5 ± 3.8	327.8 ± 3.8	1.004 ± 0.016	
120	4 cubes	337.8 ± 4.0	350.0 ± 4.1	1.036 ± 0.017	[0.971, 1.023]

As the aim of the measurement is to identify variation in the energy balance downstream various samples, the ratio $dE_{\text{SI, ratio}}$ of the mean deposited energies in the specific regions of the detector is calculated:

$$dE_{\text{SI, ratio}} = \frac{dE_{\text{SI, nonPtNP}}}{dE_{\text{SI, PtNP}}}. \tag{8.1}$$

The uncertainty on the latter results from Gaussian error propagation with a maximum value for the standard uncertainty of $dE_{\text{SI, ratio}}$, which is 0.017.
Additionally, $dE_{\text{SI, ratio}}$ depends on the thickness of the different samples since also thickness variations would lead to a changed energy deposition spectrum in the silicon sensor. The height of the samples is discussed as the ratio of the sample thicknesses $H = \frac{h_{\text{PtNP}}}{h_{\text{nonPtNP}}} = 0.997 \pm 0.021$. Analyzing CT images, the thickness of the samples was established to estimate H; see [2] for more details. By taking into consideration the height ratio in the following, there is no need for a precise measurement of the physical thicknesses. Uncertainties in the height determination of the soft material when compressing the samples during measurement were circumvented.
We assume that a nonPtNP sample is $h_{\text{nonPtNP}} = 20\,\text{mm}$ thick and a PtNP sample is $h_{\text{PtNP}} = h_{\text{nonPtNP}} \cdot (H \pm \sigma_{\text{H}})$ thick accordingly. Based on the stopping power references published by the NIST PSTAR database [27], the expected energy deposition in the sensor downstream of the samples is calculated. Subsequently, the predicted energy deposition ratio and the corresponding $\pm 1\sigma$ confidence interval can be determined, which results from the thickness ratio uncertainty. The resulting confidence intervals for all setup settings are listed in Table 8.1. They are considered as a second systematic uncertainty. If the ratio of energy depositions lies within the 1σ interval, no significant difference between the energy deposition in PtNP and nonPtNP samples is observable using the ATLAS IBL Pixel Detector.
The results for the different setups are summarized in Table 8.1. Considering the corresponding uncertainties, no significant differences between mean deposited energies in PtNP and nonPtNP samples can be observed.
While we already discussed the mean value of the deposited energy distribution, the shape of the latter was also investigated. Assuming equal mean values to correct for differences in the sample thicknesses, a Mann-Whitney U test [131] was performed using python (*mannwhitneyu* from *scipy.stats*). The test yields p-values in the range of $[0.355 - 0.708]$ for the respective distributions and thus evinces no significant

differences at $\alpha = 5\,\%$ significance level.
Comparing the energy deposition measurements with the other measurements performed in the scope of investigating the energy deposition of protons in the presence of platinum nanoparticles, we find similar results. No difference in the water-equivalent ratio (WER) of samples containing PtNPs and without was determined by analyzing depth dose distributions measured with the Giraffe detector as well as with an Advanced Markus chamber in a water phantom. An unaffected WER signifies that the stopping power for protons traversing the samples enriched with PtNPs is not increased. This is the same conclusion we drew from the energy deposition measurements with the ATLAS IBL pixel detector. If the protons' stopping power is unaffected by the presence of PtNPs, the energy deposition in the detector downstream of the different samples should be the same. We can confirm this assumption.

8.3 Spot profile comparison

The detector was irradiated in PBS mode during the presented measurement campaign. PBS mode means that a homogeneous dose distribution is created by scanning the field with pencil beam spots (step and shoot technique), introduced in section 2.3. One significant advantage of the detector under study compared to commonly used devices in proton therapy is the single particle sampling. The latter allows the temporal distinction of the hits deriving from individual pencil beam spots and, therefore, an investigation of the single spot profile shapes. In the scope of this campaign, the spot profile shapes permit conclusions on the effects of PtNPs on the scattering of the particles. Thereby, possible enhanced scattering of the proton beam in the sample spiked with PtNPs can be evaluated.

Before the spot shape investigation, the measured clusters have to be assigned to the single spots by means of their timing information and the number of trigger commands, respectively. We will refer to that quantity as trigger count. The detector was triggered using an external signal with a frequency of 1 kHz. Accordingly, the time between two trigger commands is $\approx 1\,\mathrm{ms}$.
In Figure 8.3, the correspondence of the column information of the clusters and the trigger count is presented for one of the measurements performed with one

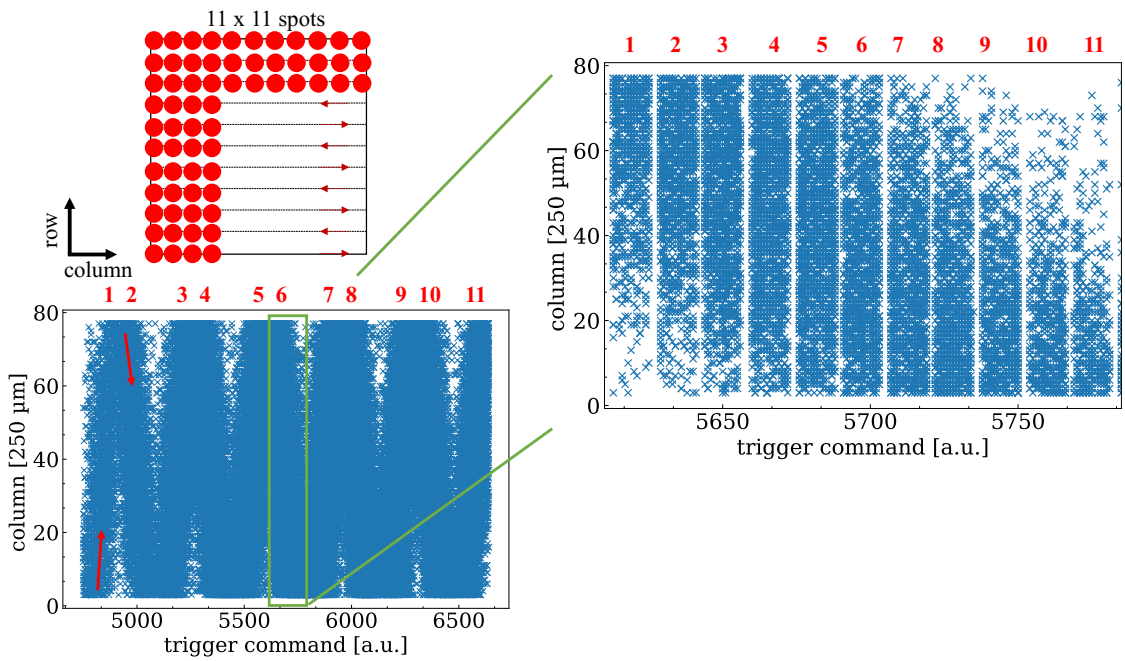

Figure 8.3: Column position for clusters depending on trigger count with zoom into the region scanning the sixth row. The pattern of the 11×11 spots per field is outlined. Absorbers with a WET of 56.2 mm were placed in front of the nozzle and one PtNP and nonPtNP sample are stacked on the detector. ($E_{\text{init}} = 120\,\text{MeV}$)

PtNP and one nonPtNP cube and the 56 mm WET material in front of the nozzle ($E_{\text{init}} = 120\,\text{MeV}$). For clarification, the emitted spot pattern consisting of 11×11 spots delivered to an area of $2.5 \times 2.5\,\text{cm}^2$ is shown in Figure 8.3.

The scanning procedure explains the distribution of the time-dependent column position per cluster. During the scanning of the rows in one direction, the position of the hits is shifted to higher pixel numbers and vice versa when scanning in the other direction to build up the next row.

For an illustration of the signal for individual spots, the column information taken during the sixth row's scanning is also shown in Figure 8.3. One can identify the signal from different PBS spots because several trigger commands between them have no hits. This is also how to assign the clusters to the single spots during the analysis.

In the thesis of Tina Pfeiler [132], the time to change between two positions of a PBS spot at a PBS nozzle placed at the WPE was determined to be in the range of $(2.25 - 4.75)$ ms for distances between $(1 - 9)$ mm depending on the direction of the

movement. Those results match the mean number of trigger commands dividing the signal $t_{\text{two sign.}} \approx (3.62 \pm 0.04)$ ms measured here.

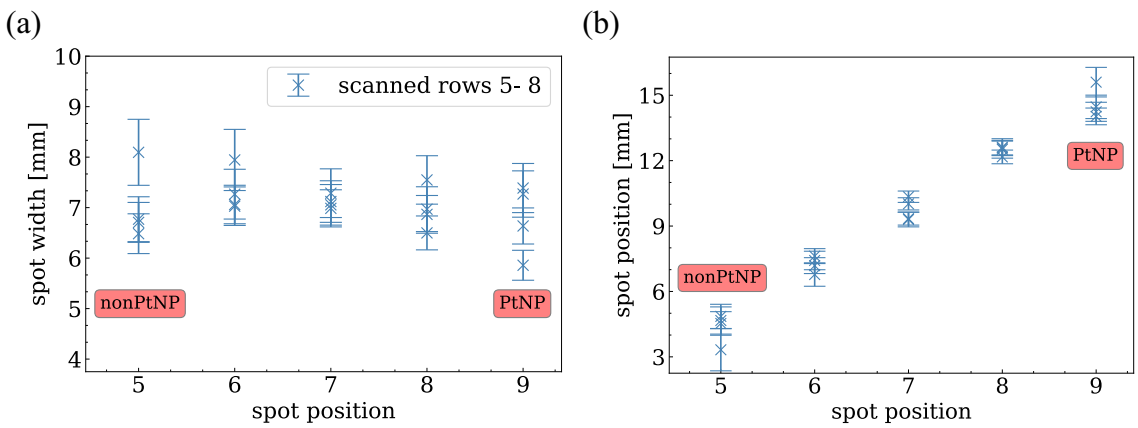

Figure 8.4: Spot widths in column direction (a) and positions on the sensor (b) for individual PBS spots. Absorbers with a WET of 56.2 mm were placed in front of the nozzle and one PtNP and nonPtNP sample are stacked on the detector. ($E_{\text{init}} = 120$ MeV)

After assigning the measured clusters to the individual spot, a one-dimensional Gaussian function was fitted to the spot profile in the longer pixels (column) direction. By summing up the hits in the row direction, an investigation of the spot shape becomes feasible even if the statistics are insufficient for fitting a two-dimensional Gaussian distribution, as presented in chapter 5.

To evaluate the influence of PtNPs on the scattering of the protons, the mean spot widths σ_{spot} with the standard error of the mean of the spots at spot position 5 and 9 are calculated, listed in Table 8.2. Spot position 9 is close to the center of the detector region covered with the PtNP sample, and position 5 is close to the center of the detector region covered with the nonPtNP sample, respectively. Since the emitted PBS field is larger than the sensitive area of the detector, only rows 5-8 were taken into account for the spot profile characterization. The considered rows run through the middle of the detector. The spot widths for the corresponding spot positions and the correlation between spot position and the measured spot position on the sensor in the column direction are shown in Figure 8.4.

If the presence of the PtNPs would affect the scattering of the protons, the ratio $\sigma_{\text{ratio, spot}}$ of σ_{spot} for the nonPtNP and the PtNP region would differ from one.

Looking at the measured $\sigma_{\text{ratio, spot}}$ and the corresponding uncertainties calculated using Gaussian error propagation listed in Table 8.2, almost all measurements are consistent with one. The consistency indicates that the multiple Coulomb scattering is not affected by the presence of PtNPs.
In conclusion, those promising results demonstrate that the detector under study allows the investigation of the spot shape of single pencil beam spots in a scanned PBS field while providing information on the deposited energy. So, the detector offers an advantage compared to the conventionally used detectors applied in this study, like the Giraffe detector or ionization chambers.

Table 8.2: Measured mean spot width σ_{spot} and mean spot width ratios $\sigma_{\text{spot,ratio}}$ for PtNP and nonPtNP samples of different thickness and for different proton energies.

E_{init} [MeV]	Setup	σ_{spot} [mm]		$\sigma_{\text{spot, ratio}}$
		PtNP	nonPtNP	
100	3 cubes	6.50 ± 0.23	6.94 ± 0.23	1.07 ± 0.05
		6.50 ± 0.21	6.65 ± 0.21	1.02 ± 0.05
110	1 cube, abso.	7.94 ± 0.35	8.00 ± 0.40	1.01 ± 0.07
		7.19 ± 0.26	7.42 ± 0.29	1.03 ± 0.06
120	1 cube, abso.	6.79 ± 0.20	7.01 ± 0.24	1.03 ± 0.05
		6.95 ± 0.22	6.64 ± 0.22	0.96 ± 0.04
120	4 cubes	6.54 ± 0.18	6.54 ± 0.19	1.00 ± 0.04

Chapter 9

Conclusion and Outlook

This work presented various studies on the characterization of the ATLAS IBL Pixel Detector for its applicability in proton therapy facilities. The main features of the detector that were tested in different measurements are the spatial resolution for field shape characterization, the sampling of the beam via the provided timing information of the hits, and the deposited energy in the sensor for beam energy measurements. To give a perspective of the detector's usage in medical physics, the detector was utilized in studies supporting the investigation of the radiosensitizing effect of platinum nanoparticles [2].

With a pixel size of 50 µm × 250 µm, the ATLAS IBL Pixel Detector provides a high spatial resolution. An application that could take advantage of the high spatial resolution is the shape characterization of proton fields, mainly if they consist of steep dose gradients or small spots. Therefore, the investigation of the shape of individual pencil beam spots with widths of 3.1 mm to 5.5 mm was presented in this work. The measured precision of 26 µm in the column direction and 28 µm in the row direction agrees with results published for other semiconductor detectors with same-sized pixels like the Timepix [99, 100]. Those pixelated semiconductor detectors outperform the spatial resolution of the commonly used Lynx PT (IBA Dosimetry, Schwarzenbruck, Germany) by order of magnitude [97, 98]. In addition to the spot shape, the spot position was also determined with a detector performance comparable to the previously presented studies.
Since the detector under study is designed for particle tracking in the ATLAS experiment, it provides timing information generated by a 40 MHz clock for individual particle hits. An external trigger frequency sets the sampling frequency up to a sustainable rate of 200 kHz. By means of those features, the time structure of different

proton fields was investigated. As expected, the measured time structure during scanning single beams differs from one taken for a single homogeneous proton field. Moreover, the linearity of the detector response with dose was investigated. In the first case, the dose variation was induced by changing the irradiation duration. For the investigated dose values in the range of $(150 - 220)$ MUs, the detector meets the requirement of the daily QA, which is the determination of an output dose consistency of $\pm 3\,\%$ [38]. In the second case, the dose was changed by adjusting the beam current. As a conservative estimation, the dose linearity was confirmed up to hit rates of $(73.85 \pm 0.95)\,\frac{\text{clusters}}{25\,\text{ns}}$ sampled with 1 kHz. For beam currents implying higher hit rates, the readout electronics saturate. In addition, measurements demonstrated that the 2 MB data storage of the readout system is a limiting factor, especially for measurements of scanned fields that take longer than 1 s.
Studies performed in the scope of this thesis showed the possibility of detecting proton range differences of 1 mm, as required for daily QA, for protons hitting the sensor with energies between 30 MeV and 44 MeV by using the information of the deposited energy per particle in the sensor [20]. Since the mean deposited energy measured systematically underestimates the reference data provided by NIST PSTAR database [27], a calibration could be performed to determine the beam energy and range, respectively. The results strongly depend on the tuning settings of the detector. It was found that the maximum processable charge of 100.000 e of the FE-I4B readout chip is far too low for applications in proton therapy. On average, protons with energies smaller than ≈ 69 MeV generate more than 100.000 e in 200 µm silicon. Due to the increased stopping power of the protons with decreasing proton energies, smaller energies are more suitable to distinguish proton range differences. Therefore, it would be appropriate if a new readout chip could process higher charge values.

Considering all the results gained in the scope of this thesis, it turns out that the spot shape, spot position, output consistency, and range verification of proton beams for daily QA could be performed using the ATLAS IBL Pixel Detector. Commonly used detector systems like the Compact Sphinx detector system (IBA Dosimetry, Schwarzenbruck, Germany) [133] or the Daily-QA3 detector (Melbourne, Florida, USA) [53] are sufficient to determine all parameters required for daily QA currently. Additionally, the large spatial resolution of the detector under study allows the

characterization even for smaller spots and higher dose gradients in the future [7, 8].

Moreover, an example of using the ATLAS IBL Pixel Detector in the field of proton therapy was given by supporting the study on the investigation of the energy deposition of protons in gels containing platinum nanoparticles (PtNPs) on a macroscopic scale [2]. By measuring the energy deposition in the silicon sensor, we proved that the presence of PtNPs does not affect the stopping power of protons in gel samples at a macroscopic scale and thereby independently confirmed measurements performed with other detectors during the study. A unique feature of the ATLAS IBL Pixel detector in the context of this study is that one could also investigate the shape of the pencil beam spots after passing different samples. An increased scattering of the protons in the presence of PtNPs was not detected here.

The prospect of fields for applications in proton therapy for hybrid pixelated semiconductor detectors, like the detector under study, is encouraging. Following the findings presented here, the detector under study will be tested as a device for Minibeam radiation therapy (MBRT) dosimetry. To characterize the beams with widths in the size of millimeters, detector thicknesses in the order of micrometers are, required [92]. The first promising results of measurements performed at UPTD were presented in the Bachelor thesis of B. Kabaci (2023): *Relativdosimetrie an Protonen Ministrahlen mit ATLAS IBL Pixeldetektor*. Moreover, S. Flynn *et al.* [134] have already published studies on the characterization of X-ray microbeams utilizing a pixelated semiconductor detector.
In addition, the high spatial resolution, combined with providing information on the deposited charge of individual particles, qualifies pixelated semiconductor detectors as promising candidates for detector systems utilized in proton radiography, as already shown with the Timepix3 detector [135], for example. Based on this thesis, the applicability of the ATLAS IBL Pixel detector for proton radiography measurements will be tested, too. H. Thews analyzed the first proton radiography measurement with the detector under study as part of her Bachelor project (2021): *Kantendetektion in der Protonenradiographie mit pixellierten Siliziumhalbleiterdetektoren*.
Since the studies presented in this work also show the limits of the readout electronics, testing other readout chips and readout systems, like the USBpix3 Multi Module

Card (MMC3) [78], for example, in clinical usage or developing a dedicated readout chip are recommended. Corresponding to the field of application of the new detector, a test of the spatial resolution, the dose linearity of the detector response, and the proton energy-dependent detector response should be investigated, taking into account the experiences of past studies. In addition, the radiation damage of the detector induced by protons in the clinical energy range has to be evaluated before usage in clinics.

Chapter

Bibliography

[1] FE-I4 collaboration and others, *The FE-I4B Integrated Circuit Guide, version 2.3* (2012).

[2] C. Behrends, C. M. Bäcker, I. Schilling, S. Zwiehoff, J. Weingarten *et al.*, *The radiosensitizing effect of platinum nanoparticles in proton irradiations is not caused by an enhanced proton energy deposition at the macroscopic scale*, Physics in Medicine & Biology **67**, 155023 (2022).

[3] C. A. Tobias, J. H. Lawrence, J. L. Born, R. K. McCombs, J. E. Roberts *et al.*, *Pituitary Irradiation with High-Energy Proton Beams A Preliminary Report**, Cancer Research **18**, 121 (1958).

[4] M. Jer, *Particle Therapy Statistics in 2014*, International Journal of Particle Therapy **2**, 50 (2015).

[5] J. A. Langendijk, L. J. Boersma, C. R. Rasch, M. van Vulpen, J. B. Reitsma *et al.*, *Clinical Trial Strategies to Compare Protons With Photons*, Seminars in Radiation Oncology **28**, 79 (2018).

[6] J. Seco, B. Clasie, and M. Partridge, *Review on the characteristics of radiation detectors for dosimetry and imaging*, Physics in Medicine & Biology **59**, R303 (2014).

[7] A. N. Schreuder and J. Shamblin, *Proton therapy delivery: what is needed in the next ten years?*, The British journal of radiology **93**, 20190359 (2020).

[8] C. Bäumer, C. Fuentes, M. Janson, A. Matic, B. Timmermann *et al.*, *Stereotactical fields applied in proton spot scanning mode with range shifter and collimating aperture*, Physics in Medicine & Biology **64**, 155003 (2019).

[9] L. Brodbek, J. Kretschmer, K. Willborn, A. Meijers, S. Both *et al.*, *Analysis of the applicability of two-dimensional detector arrays in terms of sampling rate and detector size to verify scanned intensity-modulated proton therapy plans*, Medical Physics **47**, 4589 (2020).

[10] C. Behrends, C. Bäumer, N. G. Verbeek, J. Wulff, and B. Timmermann, *Optimization of proton pencil beam positioning in collimated fields*, Medical Physics (2023).

[11] G. Pausch, J. Petzoldt, M. Berthel, W. Enghardt, F. Fiedler *et al.*, *Scintillator-Based High-Throughput Fast Timing Spectroscopy for Real-Time Range Verification in Particle Therapy*, IEEE Transactions on Nuclear Science **63**, 664 (2016).

[12] J. Yap, N. Bal, A. Kacperek, J. R. Lòpez, and C. Welsch, *Medipix3 for dosimetry and real-time beam monitoring: first tests at a 60 MeV proton therapy facility*, Journal of Instrumentation **16**, T11001 (2021).

[13] J. Petzoldt, K. E. Roemer, W. Enghardt, F. Fiedler, C. Golnik *et al.*, *Characterization of the microbunch time structure of proton pencil beams at a clinical treatment facility*, Physics in Medicine & Biology **61**, 2432 (2016).

[14] R. P. Johnson, *Review of medical radiography and tomography with proton beams*, Reports on Progress in Physics **81**, 016701 (2017).

[15] X. Llopart, R. Ballabriga, M. Campbell, L. Tlustos, and W. Wong, *Timepix, a 65k programmable pixel readout chip for arrival time, energy and/or photon counting measurements*, Nuclear Instruments and Methods in Physics Research Section A: Accelerators, Spectrometers, Detectors and Associated Equipment **581**, 485 (2007).

[16] T. Gehrke, R. Gallas, O. Jäkel, and M. Martišíková, *Proof of principle of helium-beam radiography using silicon pixel detectors for energy deposition measurement, identification, and tracking of single ions*, Medical Physics **45**, 817 (2018).

[17] S. Grinstein on behalf of the ATLAS Collaboration, *Overview of the ATLAS insertable B-layer (IBL) project*, Nuclear Instruments and Methods in Physics

Research Section A: Accelerators, Spectrometers, Detectors and Associated Equipment **699**, 61 (2013).

[18] M. Garcia-Sciveres, D. Arutinov, M. Barbero, R. Beccherle, S. Dube *et al.*, *The FE-I4 pixel readout integrated circuit*, Nuclear Instruments and Methods in Physics Research Section A: Accelerators, Spectrometers, Detectors and Associated Equipment **636**, S155 (2011).

[19] I. Schilling, C. M. Bäcker, C. Bäumer, C. Behrends, K. Kröninger *et al.*, *Characterization of pixelated silicon detectors for daily quality assurance measurements in proton therapy*, Journal of Physics: Conference Series **2374**, 012178 (2022).

[20] I. Schilling, C. M. Bäcker, C. Bäumer, C. Behrends, M. Hötting *et al.*, *Measuring the Beam Energy in Proton Therapy Facilities Using ATLAS IBL Pixel Detectors*, Instruments **6**, 80 (2022).

[21] W. D. Newhauser and R. Zhang, *The physics of proton therapy*, Physics in Medicine & Biology **60**, R155 (2015).

[22] V. L. Highland, *Some practical remarks on multiple scattering*, Nuclear Instruments and Methods **129**, 497 (1975).

[23] H. Bethe, *Zur Theorie des Durchgangs schneller Korpuskularstrahlen durch Materie*, Annalen der Physik **397**, 325 (1930).

[24] F. Bloch, *Zur Bremsung rasch bewegter Teilchen beim Durchgang durch Materie*, Annalen der Physik **408**, 285 (1933).

[25] U. Fano, *Penetration of protons, alpha particles, and mesons*, Annual Review of Nuclear Science **13**, 1 (1963).

[26] H. Kolanoski and N. Wermes, *Teilchendetektoren*, Springer Berlin, Heidelberg (2016).

[27] M. Berger, J. Coursey, M. Zucker, and J. Chang, *ESTAR, PSTAR, and ASTAR: Computer Programs for Calculating Stopping-Power and Range Tables for Electrons, Protons, and Helium Ions (Version 1.2.3).*, `http://physics.nist.gov/Star` (2005), accessed: 2022-06-15.

[28] F. Nüsslin, *Meßmethoden für die Dosimetrie*, Springer Berlin Heidelberg, Berlin, Heidelberg (2002).

[29] T. Bortfeld, *An analytical approximation of the Bragg curve for therapeutic proton beams*, Medical physics **24**, 2024 (1997).

[30] F. Mentzel, *Software Bortfeld Fit.*, `https://gitlab.e4.physik.tu-dortmund.de/fmentzel/pybragg`, accessed: 2023-02-15.

[31] H. Paganetti, *Range uncertainties in proton therapy and the role of Monte Carlo simulations*, Physics in Medicine & Biology **57**, R99 (2012).

[32] W. Ulmer, *Theoretical aspects of energy–range relations, stopping power and energy straggling of protons*, Radiation Physics and Chemistry **76**, 1089 (2007).

[33] R. Zhang and W. D. Newhauser, *Calculation of water equivalent thickness of materials of arbitrary density, elemental composition and thickness in proton beam irradiation*, Physics in Medicine & Biology **54**, 1383 (2009).

[34] H. Paganetti, *Proton Therapy Physics, Second Edition*, Series in Medical Physics and Biomedical Engineering, CRC Press, Boca Raton, New York, (2018).

[35] G. Battistoni, I. Mattei, and S. Muraro, *Nuclear physics and particle therapy*, Advances in Physics: X **1**, 661 (2016).

[36] M. Engelsman, H.-M. Lu, D. Herrup, M. Bussiere, and H. Kooy, *Commissioning a passive-scattering proton therapy nozzle for accurate SOBP delivery*, Medical physics **36**, 2172 (2009).

[37] M. Krämer and M. Durante, *Ion beam transport calculations and treatment plans in particle therapy*, The European Physical Journal D **60**, 195 (2010).

[38] B. Arjomandy, P. Taylor, C. Ainsley, S. Safai, N. Sahoo *et al.*, *AAPM task group 224: Comprehensive proton therapy machine quality assurance*, Medical physics **46**, e678 (2019).

[39] C. M. Bäcker, personal communication (2022-05-27).

[40] E. Pedroni, R. Bacher, H. Blattmann, T. Böhringer, A. Coray *et al.*, *The 200-MeV proton therapy project at the Paul Scherrer Institute: Conceptual design and practical realization*, Medical physics **22**, 37 (1995).

[41] B. Marchand, D. Prieels, B. Bauvir, R. Sépulchre, and M. Gérard, *IBA proton pencil beam scanning: an innovative solution for cancer treatment*, Proceedings of EPAC 2539–2541 (2000).

[42] C. Bäumer, S. Plaude, D. A. Khalil, D. Geismar, P.-H. Kramer *et al.*, *Clinical implementation of proton therapy using pencil-beam scanning delivery combined with static apertures*, Frontiers in Oncology **11**, 599018 (2021).

[43] M. A. Chanrion, F. Ammazzalorso, A. Wittig, R. Engenhart-Cabillic, and U. Jelen, *Dosimetric consequences of pencil beam width variations in scanned beam particle therapy*, Physics in Medicine & Biology **58**, 3979 (2013).

[44] B. Arjomandy, N. Sahoo, X. Ding, and M. Gillin, *Use of a two-dimensional ionization chamber array for proton therapy beam quality assurance*, Medical physics **35**, 3889 (2008).

[45] S. Giordanengo and H. Palmans, *Dose detectors, sensors, and their applications*, Medical physics **45**, e1051 (2018).

[46] S. Dhanesar, N. Sahoo, M. Kerr, M. B. Taylor, P. Summers *et al.*, *Quality assurance of proton beams using a multilayer ionization chamber system*, Medical physics **40**, 092102 (2013).

[47] C. Bäumer, B. Koska, J. Lambert, B. Timmermann, T. Mertens, and P. T. Talla, *Evaluation of detectors for acquisition of pristine depth-dose curves in pencil beam scanning*, Journal of applied clinical medical physics **16**, 151 (2015).

[48] R. Catalano, G. Petringa, G. Cuttone, V. Bonanno, D. Chiappara *et al.*, *Transversal dose profile reconstruction for clinical proton beams: A detectors inter-comparison*, Physica Medica **70**, 133 (2020).

[49] L. Placidi, M. Togno, D. C. Weber, A. J. Lomax, and J. Hrbacek, *Range resolution and reproducibility of a dedicated phantom for proton PBS daily quality assurance*, Zeitschrift für Medizinische Physik **28**, 310 (2018).

[50] S. Rana, J. Bennouna, E. J. J. Samuel, and A. N. Gutierrez, *Development and long-term stability of a comprehensive daily QA program for a modern pencil beam scanning (PBS) proton therapy delivery system*, Journal of Applied Clinical Medical Physics **20**, 29 (2019).

[51] Z. Su, W. Hsi, J. Forthomme, and S. Rossomme, *Evaluations of a flat-panel based compact daily quality assurance device for proton pencil beam scanning (PBS) system*, Physica medica **80**, 243 (2020).

[52] X. Ding, Y. Zheng, O. Zeidan, A. Mascia, W. Hsi *et al.*, *A novel daily QA system for proton therapy*, Journal of Applied Clinical Medical Physics **14**, 115 (2013).

[53] J. Lambert, C. Bäumer, B. Koska, and X. Ding, *Daily QA in proton therapy using a single commercially available detector*, Journal of Applied Clinical Medical Physics **15**, 217 (2014).

[54] L. Evans and P. Bryant, *LHC Machine*, Journal of Instrumentation **3**, S08001 (2008).

[55] R. Assmann, M. Giovannozzi, Y. Papaphilippou, F. Zimmermann, A. Caldwell *et al.*, *Generation of short Proton bunches in the CERN Accelerator Complex*, Proceedings of PAC09, Vancouver, BC, Canada, 4542 (2010).

[56] *The twists and turns of a successful year for the LHC.*, CERN Courier **57**, 10 (2017).

[57] G. Aad, B. Abbott, J. Abdallah, O. Abdinov, R. Aben, and others (ATLAS Collaboration), *Search for new light gauge bosons in Higgs boson decays to four-lepton final states in pp collisions at* $\sqrt{s} = 8$ TeV *with the ATLAS detector at the LHC*, Physical Review D **92**, 092001 (2015).

[58] CMS Collaboration, *Observation of a new boson at a mass of 125 GeV with the CMS experiment at the LHC*, Physics Letters B **716**, 30 (2012).

[59] ATLAS Collaboration and others, *The ATLAS experiment at the CERN large hadron collider*, Journal of Instrumentation **3**, S08003 (2008).

[60] ATLAS Collaboration, *ATLAS insertable B-layer technical design report addendum. Addendum to CERN-LHCC-2010-013*, ATLAS-TDR-019, https://cds.cern.ch/record/1451888 (2012).

[61] ATLAS Collaboration, *ATLAS insertable B-layer technical design report*, ATLAS-TDR-019, https://cds.cern.ch/record/1291633 (2010).

[62] W. R. Leo, *Techniques for nuclear and particle physics experiments: a how-to approach*, Springer Berlin, Heidelberg (2012).

[63] G. Lutz, *Semiconductor radiation detectors: Device physics*, Springer Berlin, Heidelberg (2007).

[64] S. M. Sze, *Semiconductor devices: physics and technology*, John Wiley & Sons, Ltd, Hoboken, New Jersey, (2008).

[65] C. A. Klein, *Bandgap dependence and related features of radiation ionization energies in semiconductors*, Journal of Applied Physics **39**, 2029 (1968).

[66] S. Kumar, B. A. Reshi, and R. Varma, *Comparison of Silicon, Germanium, Gallium Nitride, and Diamond for using as a detector material in experimental high energy physics*, Results in Physics **11**, 461 (2018).

[67] G. Lindström, M. Moll, and E. Fretwurst, *Radiation hardness of silicon detectors – a challenge from high-energy physics*, Nuclear Instruments and Methods in Physics Research Section A: Accelerators, Spectrometers, Detectors and Associated Equipment **426**, 1 (1999).

[68] G. Lindström, *Radiation damage in silicon detectors*, Nuclear Instruments and Methods in Physics Research Section A: Accelerators, Spectrometers, Detectors and Associated Equipment **512**, 30 (2003), proceedings of the 9th European Symposium on Semiconductor Detectors: New Developments on Radiation Detectors.

[69] G. Kramberger, *Signal development in irradiated silicon detectors*, Ph.D. thesis, Stefan Inst., Ljubljana (2001).

[70] N. Wermes, *Pixel detectors ... where do we stand?*, Nuclear Instruments and Methods in Physics Research Section A: Accelerators, Spectrometers, Detectors and Associated Equipment **924**, 44 (2019), 11th International Hiroshima Symposium on Development and Application of Semiconductor Tracking Detectors.

[71] ATLAS IBL Collaboration, *Production and integration of the ATLAS Insertable B-Layer*, Journal of Instrumentation **13**, T05008 (2018).

[72] N. Savic, J. Beyer, A. L. Rosa, A. Macchiolo, and R. Nisius, *Investigation of thin n-in-p planar pixel modules for the ATLAS upgrade*, Journal of Instrumentation **11**, C12008 (2016).

[73] J.-C. Beyer, A. L. Rosa, A. Macchiolo, R. Nisius, N. Savic *et al.*, *Characterisation of novel thin n-in-p planar pixel modules for the ATLAS Inner Tracker upgrade*, Journal of Instrumentation **13**, C01009 (2018).

[74] J.-C. Beyer, *Optimisation of Pixel Modules for the ATLAS Inner Tracker at the High-Luminosity LHC*, Ph.D. thesis, LMU München, München (2019).

[75] T. Wittig, *Slim edge studies, design and quality control of planar ATLAS IBL pixel sensors*, PhD thesis, Universität Dortmund, Dortmund (2013).

[76] P. Grenier, *Silicon Sensor Technologies for the ATLAS IBL Upgrade*, Physics Procedia **37**, 874 (2012), proceedings of the 2nd International Conference on Technology and Instrumentation in Particle Physics (TIPP 2011).

[77] B. Bergmann, M. Pichotka, S. Pospisil, J. Vycpalek, P. Burian *et al.*, *3D track reconstruction capability of a silicon hybrid active pixel detector*, The European Physical Journal C **77**, 421 (2017).

[78] *USBpix website*, `http://icwiki.physik.uni-bonn.de/twiki/bin/view/Systems/UsbPix`, accessed: 2022-12-12.

[79] M. Backhaus, M. Barbero, L. Gonella, J. Große-Knetter, F. Hügging *et al.*, *Development of a versatile and modular test system for ATLAS hybrid pixel detectors*, Nuclear Instruments and Methods in Physics Research Section A: Accelerators, Spectrometers, Detectors and Associated Equipment **650**, 37 (2011), international Workshop on Semiconductor Pixel Detectors for Particles and Imaging 2010.

[80] D. Cussans, *Description of the JRA1 trigger logic unit (TLU), v0. 2c*, EUDETMemo-2009-04 (2009).

[81] *STcontrol User Guide*, `https://icwiki.physik.uni-bonn.de/twiki/bin/view/Systems/STcontrolI4/`, accessed: 2022-12-12.

[82] A. Gisen, *Quad module prototypes and design improvement studies of planar n+-in-n silicon pixel sensors for the ATLAS Inner Tracker upgrade*, Ph.D. thesis, TU Dortmund University (2018).

[83] J. Rieger, *Comparison of Thin n- and p-type Bulk Silicon Pixel Sensors*, Masters Thesis, Georg-August-University Göttingen (2012).

[84] M. Campbell, V. Havranek, E. Heijne, T. Holy, J. Idarraga *et al.*, *Charge collection from proton and alpha particle tracks in silicon pixel detector devices*, 2007 IEEE Nuclear Science Symposium Conference Record **2**, 1047 (2007).

[85] M. Kroupa, J. Jakubek, and F. Krejci, in *2008 IEEE Nuclear Science Symposium Conference Record*, IEEE (2008), 259–262.

[86] A. Moignier, E. Gelover, D. Wang, B. Smith, R. Flynn *et al.*, *Theoretical benefits of dynamic collimation in pencil beam scanning proton therapy for brain tumors: dosimetric and radiobiological metrics*, International Journal of Radiation Oncology* Biology* Physics **95**, 171 (2016).

[87] J. Meyer, J. Eley, T. E. Schmid, S. E. Combs, R. Dendale *et al.*, *Spatially fractionated proton minibeams*, The British journal of radiology **92**, 20180466 (2019).

[88] Y. Prezado, G. Jouvion, D. Hardy, A. Patriarca, C. Nauraye *et al.*, *Proton minibeam radiation therapy spares normal rat brain: Long-Term Clinical, Radiological and Histopathological Analysis*, Scientific reports **7**, 1 (2017).

[89] S. Girst, C. Greubel, J. Reindl, C. Siebenwirth, O. Zlobinskaya *et al.*, *Proton Minibeam Radiation Therapy Reduces Side Effects in an In Vivo Mouse Ear Model*, International Journal of Radiation Oncology*Biology*Physics **95**, 234 (2016), particle Therapy Special Edition.

[90] Y. Prezado, G. Jouvion, C. Guardiola, W. Gonzalez, M. Juchaux *et al.*, *Tumor Control in RG2 Glioma-Bearing Rats: A Comparison Between Proton Minibeam Therapy and Standard Proton Therapy*, International Journal of Radiation Oncology*Biology*Physics **104**, 266 (2019).

[91] C. Lamirault, E. Brisebard, A. Patriarca, M. Juchaux, D. Crepin *et al.*, *Spatially modulated proton minibeams results in the same increase of lifespan as a uniform target dose coverage in F98-glioma-bearing rats*, Radiation Research **194**, 715 (2020).

[92] M. Sotiropoulos and Y. Prezado, *Radiation quality correction factors for improved dosimetry in preclinical minibeam radiotherapy*, Medical Physics **49**, 6716 (2022).

[93] M. Clausen, S. Ruangchan, A. Sotoudegan, A. F. Resch, B. Knäusl *et al.*, *Small field proton irradiation for in vivo studies: Potential and limitations when adapting clinical infrastructure*, Zeitschrift für Medizinische Physik (2022).

[94] O. Behnke, K. Kröninger, G. Schott, and T. Schörner-Sadenius, *Data analysis in high energy physics: a practical guide to statistical methods*, John Wiley & Sons, Ltd, Hoboken, New Jersey, (2013).

[95] R. Andrae, T. Schulze-Hartung, and P. Melchior, *Dos and don'ts of reduced chi-squared*, arXiv preprint arXiv:1012.3754 (2010).

[96] *Scipy optimize.curve_fit Reference Guide.*, `https://docs.scipy.org/doc/scipy/reference/generated/scipy.optimize.curve_fit.html`, accessed: 2022-11-24.

[97] S. Russo, A. Mirandola, S. Molinelli, E. Mastella, A. Vai *et al.*, *Characterization of a commercial scintillation detector for 2-D dosimetry in scanned proton and carbon ion beams*, Physica Medica **34**, 48 (2017).

[98] F. Bisello, D. Menichelli, M. Scaringella, C. Talamonti, M. Zani *et al.*, *Development of silicon monolithic arrays for dosimetry in external beam radiotherapy*, Nuclear Instruments and Methods in Physics Research Section A: Accelerators, Spectrometers, Detectors and Associated Equipment **796**, 85 (2015).

[99] M. G. Bisogni, G. A. P. Cirrone, G. Cuttone, A. Del Guerra, P. Lojacono *et al.*, *Medipix2 as a tool for proton beam characterization*, Nuclear Instruments and Methods in Physics Research Section A: Accelerators, Spectrometers, Detectors and Associated Equipment **607**, 48 (2009).

[100] A. Rosenfeld, S. Alnaghy, M. Petasecca, D. Cutajar, M. Lerch *et al.*, *Medipix detectors in radiation therapy for advanced quality-assurance*, Radiation Measurements **130**, 106211 (2020).

[101] A. Mirandola, S. Molinelli, G. Vilches Freixas, A. Mairani, E. Gallio *et al.*, *Dosimetric commissioning and quality assurance of scanned ion beams at the Italian National Center for Oncological Hadrontherapy*, Medical physics **42**, 5287 (2015).

[102] F. Hügging on behalf of the ATLAS Pixel Collaboration, *Front-End electronics and integration of ATLAS pixel modules*, Nuclear Instruments and Methods in Physics Research Section A: Accelerators, Spectrometers, Detectors and Associated Equipment **549**, 157 (2005).

[103] A Miucci on behalf of the ATLAS Collaboration, *The ATLAS Insertable B-Layer project*, Journal of Instrumentation **9**, C02018 (2014).

[104] C. Bäumer, B. Ackermann, M. Hillbrand, F.-J. Kaiser, B. Koska *et al.*, *Dosimetry intercomparison of four proton therapy institutions in Germany employing spot scanning*, Zeitschrift für Medizinische Physik **27**, 80 (2017).

[105] M. Aaboud on behalf of the ATLAS Collaboration, *Search for metastable heavy charged particles with large ionization energy loss in pp collisions at* $\sqrt{s} = 13$ TeV *using the ATLAS experiment*, Physical Review D **93**, 112015 (2016).

[106] T. Gehrke, L. Burigo, G. Arico, S. Berke, J. Jakubek *et al.*, *Energy deposition measurements of single 1H, 4He and 12C ions of therapeutic energies in a silicon pixel detector*, Journal of Instrumentation **12**, P04025 (2017).

[107] M. Kroupa, A. Bahadori, T. Campbell-Ricketts, S. George, and C. Zeitlin, *Kinetic energy reconstruction with a single layer particle telescope*, Applied Physics Letters **112**, 134103 (2018).

[108] C. Granja, J. Jakubek, M. Martisikova, S. Kodaira, S. Polansky *et al.*, *Dynamic range and resolving power of the Timepix detector to heavy charged particles*, Journal of Instrumentation **13**, C11003 (2018).

[109] M.-R. Mohammadian-Behbahani, V. Monaco, M. Abujami, D. Bersani, E. M. Data *et al.*, *Two-channel combination methods for count-loss correction in radiation measurements at high rates and with pulsed sources*, Nuclear Instruments and Methods in Physics Research Section A: Accelerators, Spectrometers, Detectors and Associated Equipment **1040**, 167195 (2022).

[110] C. Bäumer, C. M. Bäcker, M. Gerhardt, E. Grusell, B. Koska *et al.*, *Measurement of absolute activation cross sections from carbon and aluminum for proton therapy*, Nuclear Instruments and Methods in Physics Research Section B: Beam Interactions with Materials and Atoms **440**, 75 (2019).

[111] A. Parisi, P. Olko, J. Swakoń, T. Horwacik, H. Jabłoński *et al.*, *Microdosimetric characterization of a clinical proton therapy beam: comparison between simulated lineal energy distributions in spherical water targets and experimental measurements with a silicon detector*, Physics in Medicine & Biology **67**, 015006 (2022).

[112] C. Behrends, C. Bäumer, N. Verbeek, J. Ehlert, R. Prasad *et al.*, *Providing proton fields down to the few-MeV level at clinical pencil beam scanning facilities for radiobiological experiments*, Medical Physics **49**, 666 (2022).

[113] International Commission on Radiation Units and Measurements, *Linear energy transfer*, ICRU REPORT **16**, 14 (1970).

[114] M. Kroupa, A. Bahadori, T. Campbell-Ricketts, A. Empl, S. M. Hoang *et al.*, *A semiconductor radiation imaging pixel detector for space radiation dosimetry*, Life Sciences in Space Research **6**, 69 (2015).

[115] J. Bouchami, A. Gutierrez, A. Houdayer, J. Idarraga, J. Jakubek *et al.*, *Study of the charge sharing in silicon pixel detector with heavy ionizing particles interacting with a Medipix2 and a Timepix devices*, 2008 IEEE Nuclear Science Symposium Conference Record 1358–1360 (2008).

[116] C. Leroy and P.-G. Rancoita, *Silicon solid state devices and radiation detection*, World Scientific Publishing Company, Singapur (2012).

[117] *pyLandau package website.*, `https://pypi.org/project/pylandau/`, accessed: 2023-18-01.

[118] I. C. on Radiation Units and Measurements, *Stopping powers and ranges for protons and alpha particles*, Tech. rep. (1993).

[119] P. Sigmund, A. Schinner, and H. Paul, *Errata and addenda for ICRU Report 73, Stopping of Ions Heavier than Helium*, Journal of the ICRU (2009).

[120] C. Granja, C. Oancea, J. Jakubek, L. Marek, E. Benton *et al.*, *Wide-range tracking and LET-spectra of energetic light and heavy charged particles*, Nuclear Instruments and Methods in Physics Research Section A: Accelerators, Spectrometers, Detectors and Associated Equipment **988**, 164901 (2021).

[121] J. F. Hainfeld, F. A. Dilmanian, D. N. Slatkin, and H. M. Smilowitz, *Radiotherapy enhancement with gold nanoparticles*, Journal of Pharmacy and Pharmacology **60**, 977 (2010).

[122] J. Schuemann, A. F. Bagley, R. Berbeco, K. Bromma, K. T. Butterworth *et al.*, *Roadmap for metal nanoparticles in radiation therapy: current status, translational challenges, and future directions*, Physics in Medicine & Biology **65**, 21RM02 (2020).

[123] S. Lacombe, E. Porcel, and E. Scifoni, *Particle therapy and nanomedicine: state of art and research perspectives*, Cancer Nanotechnology **8**, 1 (2017).

[124] J.-K. Kim, S.-J. Seo, K.-H. Kim, T.-J. Kim, M.-H. Chung *et al.*, *Therapeutic application of metallic nanoparticles combined with particle-induced x-ray emission effect*, Nanotechnology **21**, 425102 (2010).

[125] G. Dollinger, *Comment on 'Therapeutic application of metallic nanoparticles combined with particle-induced x-ray emission effect'*, Nanotechnology **22**, 248001 (2011).

[126] J. C. Polf, L. F. Bronk, W. H. Driessen, W. Arap, R. Pasqualini *et al.*, *Enhanced relative biological effectiveness of proton radiotherapy in tumor cells with internalized gold nanoparticles*, Applied physics letters **98**, 193702 (2011).

[127] C. Le Sech, K. Kobayashi, N. Usami, Y. Furusawa, E. Porcel *et al.*, *Comment on "Enhanced relative biological effectiveness of proton radiotherapy in tumor cells with internalized gold nanoparticles"[Appl. Phys. Lett. 98, 193702 (2011)]*, Applied Physics Letters **100**, 193702 (2012).

[128] C. Sicard-Roselli, E. Brun, M. Gilles, G. Baldacchino, C. Kelsey *et al.*, *A new mechanism for hydroxyl radical production in irradiated nanoparticle solutions*, small **10**, 3338 (2014).

[129] S. Zwiehoff, J. Johny, C. Behrends, A. Landmann, F. Mentzel *et al.*, *Enhancement of proton therapy efficiency by noble metal nanoparticles is driven by the number and chemical activity of surface atoms*, Small **18**, 2106383 (2022).

[130] F. Waag, R. Streubel, B. Gökce, and S. Barcikowski, *Synthesis of gold, platinum, and gold-platinum alloy nanoparticle colloids with high-power megahertz-repetition-rate lasers: the importance of the beam guidance method*, Applied Nanoscience **11**, 1303 (2021).

[131] H. B. Mann and D. R. Whitney, *On a test of whether one of two random variables is stochastically larger than the other*, The annals of mathematical statistics **18**, 50 (1947).

[132] T. Pfeiler, *Dynamic evaluation of 4D robust optimisation for motion management in scanned proton therapy of hepatocellular carcinoma*, PhD thesis, Universität Dortmund, Dortmund (2018).

[133] E. Rossi, S. Russo, D. Maestri, G. Magro, A. Mirandola *et al.*, *Characterization of a flat-panel detector for 2D dosimetry in scanned proton and carbon ion beams*, Physica Medica **107**, 102561 (2023).

[134] S. Flynn, T. Price, P. P. Allport, I. Silvestre Patallo, R. Thomas *et al.*, *Evaluation of a pixelated large format CMOS sensor for x-ray microbeam radiotherapy*, Medical Physics **47**, 1305 (2020).

[135] V. Olsansky, C. Granja, C. Oancea, A. Mackova, V. Havranek *et al.*, *Spectral-sensitive proton radiography of thin samples with the pixel detector Timepix3*, Journal of Instrumentation **17**, C04016 (2022).

Chapter

Publications

Articles

1. I. Schilling, C. M. Bäcker, C. Bäumer, C. Behrends, M. Hötting, J. Hohmann, K. Kröninger, B. Timmermann and J. Weingarten, *Measuring the Beam Energy in Proton Therapy Facilities Using ATLAS IBL Pixel Detectors*, Instruments **6**(4), 80 (2022).

2. I. Schilling, C. M. Bäcker, C. Bäumer, C. Behrends, K. Kröninger, B. Timmermann and J. Weingarten, *Characterization of pixelated silicon detectors for daily quality assurance measurements in proton therapy*, Journal of Physics: Conference Series **2374**, 012178 (2022).

3. C. Behrends, C. M. Bäcker, I. Schilling, S. Zwiehoff, J. Weingarten, K. Kröninger, C. Rehbock, S. Barcikowski, J. Wulff, C. Bäumer and B. Timmermann, *The radiosensitizing effect of platinum nanoparticles in proton irradiations is not caused by an enhanced proton energy deposition at the macroscopic scale*, Physics in Medicine and Biology **67**, 155023 (2022).

Conference contributions

1. I. Schilling, C. M. Bäcker, C. Bäumer, C. Behrends, K. Kröninger, B. Timmermann and J. Weingarten, *Development of a pixelated silicon detector for daily quality assurance in PBS proton therapy with one single device*, DPG Frühjahrstagung 2021, online (talk).

2. I. Schilling, C. M. Bäcker, C. Bäumer, C. Behrends, K. Kröninger, B. Zimmermann and J. Weingarten, *Characterization of Pixelated Silicon Detectors for the Measurement of Small Radiation Fields in Proton Therapy*, TIPP 2021, online (talk).

3. I. Schilling, C. M. Bäcker, C. Bäumer, C. Behrends, K. Kröninger, B. Timmermann and J. Weingarten, *Characterization of Pixelated Silicon Detectors for the Measurement of Small Radiation Fields in Proton Therapy*, Joint Conference of the ÖGMP, DGMP and SGSMP 2021, online (poster).

4. I. Schilling, C. M. Bäcker, C. Bäumer, C. Behrends, M. Hötting, K. Kröninger, B. Timmermann and J. Weingarten, *Comparison of different methods to measure the beam energy in proton therapy using pixelated silicon detectors*, AAPM 2021, Washington, DC, USA (poster).

5. I. Schilling, C. M. Bäcker, C. Bäumer, C. Behrends, M. Hötting, J. Hohmann, K. Kröninger, B. Timmermann and J. Weingarten, *Measuring the beam energy at a proton therapy facility using ATLAS IBL pixel detectors*, DPG Frühjahrstagung 2023, Dresden, DE (talk).

Supervised and co-supervised theses

1. B. Kabakci, *Relativdosimetrie an Protonen Ministrahlen mit ATLAS IBL Pixeldetektor*, Bachelor Thesis, 2023.

2. H. Thews, *Kantendetektion in der Protonenradiographie mit pixellierten Siliziumhalbleiterdetektoren*, Bachelor Thesis, 2022.

3. N. Bauer, *Strahlform- und Strahlpositionsmessungen mit pixellierten Siliziumhalbleiterdetektoren zur täglichen Qualitätssicherung in der Protonentherapie*, Bachelor Thesis, 2022.

4. J. Wüller, *Simulation der Ladungsdeposition eines Protonenstrahls in einem Siliziumsensor bei streifendem Einfall*, Bachelor Thesis, 2021.

5. V. Gesthüsen, *Simulation der Tiefendosiskurve eines PBS Protonenstrahls in einem Siliziumsensor unter Verwendung verschiedener Rangeshifter*, Bachelor Thesis, 2021.

6. M. Wiegers, *Untersuchung der maximalen detektierbaren Trefferrate eines ATLAS Pixeldetektors*, Bachelor Thesis, 2021.

7. S. Jansen, *Vermessung von Röntgenspektren mit ATLAS Pixeldetektoren*, Master Thesis, 2020.

8. O. El-kettani, *Studie zur Eignung von ATLAS Pixeldetektoren zur Vermessung von Strahlfeldern in der Protonentherapie*, Bachelor Thesis, 2020.

9. R. Peschin, *Spektroskopische Untersuchung von Neutron-aktivierten Silizium Detektoren*, Bachelor Thesis, 2020.

10. E. Akay, *Simulation der Ladungsdeposition eines Protonenstrahls in einem pixellierten Siliziumhalbleiterdetektor*, Bachelor Thesis, 2020.

11. P. Wegner, *Simulation von elektronischen Dosimetern zur Optimierung der Eintrittsfenstermaterialien und des Dosimeteraufbaus*, Bachelor Thesis, 2020.

Chapter

Danksagung

Abschließend möchte Ich mich bei allen bedanken, die mich während der letzten Jahre unterstützt haben und mir damit das Erstellen dieser Dissertation ermöglicht haben.

Zunächst möchte ich Herrn Prof. Dr. Kevin Kröninger dafür danken meine Promotion betreut zu haben und mir die Infrastruktur seiner Arbeitsgruppe zur Verfügung gestellt zu haben. Ich danke Ihnen darüber hinaus für die fachliche Diskussionen und Chancen mich weiter zu entwicklen, die Sie mir im Rahmen der Promotion ermöglicht haben. Ich möchte mich ebenso bei Herrn Dr. Christian Bäumer bedanken, sich dazu bereit erkärt zu haben das Zweitgutachten dieser Arbeit zu übernehmen und mich bei der gemeinsamen Forschung am WPE immer tatkräftig unterstützt zu haben.

Vielen Dank an die MERCUR-Stiftung für die Förderung der Arbeit im Rahmen des Graduiertenkollegs “Präzisionsprotonentherapie— Praxisbezogene Physik und Chemie an der Schnittstelle zur Medizin” (Grant Number St-2019-0007).

Ein ganz besonderer Dank gilt Jens. Zum einen für die fachliche Unterstützung im Rahmen meiner Doktorarbeit, die meinen Forschungsalltag bereichert hat und für das Korrekturlesen dieser Arbeit. Genauso aber auch für die vielen vertrauensvollen nicht-fachliche Gespräche immer wenn es nötig war.

Vielen Dank an die IBA PT Teams und die Physik Teams des WPEs und der UPTD für die Unterstützung während der Messreihen. Besonders hervorheben möchte ich hierbei Carina und Max, sowie Jörg und Sebastian.

Danke an die gesamte Arbeitsgruppe Kröninger für die schöne Zeit und die vielen tollen Abende. Ich werde die Arbeit mit euch vermissen. Vielen Dank Andrea

für die tollen Gespräche, dein offenes Ohr und deine Hilfe bei allen bürokratischen Problemen. Danke Mike für deine Unterstützung im Labor.

Danke Lukas, Max und Marta für das Korrekturlesen und die Verbesserungsvorschläge zu dieser Arbeit. Vielen Dank Jana, Flo und Marius für die fachliche und technische Unterstützung.

Während meines Studiums waren Evelin und Alina an meiner Seite und sind mit mir durch Höhen und Tiefen gegangen. Ich bin euch dankbar für jede Umarmung, jedes Gespräch und eure Freundschaft.

Als Letztes möchte ich den Leuten danken, ohne die ich heute nicht die wäre die ich bin: meiner Familie. Ihr gebt mir Sicherheit, baut mich auf, wenn ich zweifel, habt für jedes Problem eine Lösung und lacht mit mir.
Danke Lukas für die Gewissheit, dass du immer hinter stehst. Ich freu mich auf alles, was noch kommt ... :)